

**ATOMIC AND ELECTRONIC
ANALYSIS OF INTERACTIONS
BETWEEN NANOPOROUS AU
AND PROTEINS**

Naoki Miyazawa

CONTENTS

1. GENERAL INTRODUCTION

1.1 Introduction

<i>1.1.1 Nanoporous metals and their properties</i>	1
<i>1.1.2 Antimicrobial properties of nanomaterials</i>	3
<i>1.1.3 Antimicrobial properties of nanoporous Au</i>	10
<i>1.1.4 Computational studies of interactions between metals and biomacromolecules</i>	13

1.2 Scope of the present study

<i>1.2.1 Enhanced enzyme properties of laccase</i>	15
<i>1.2.2 Antimicrobial properties of nanoporous Au</i>	17

References	19
-------------------------	-----------

2. MOLECULAR DYNAMICS STUDY OF LACCASE IMMOBILIZED ON SELF-ASSEMBLED MONOLAYER MODIFIED AU

2.1 Introduction	25
2.2 Methods	27
2.3 Results and discussion	31
2.4 Conclusion	39
References	41

3. ANTIMICROBIAL MECHANISMS DUE TO HYPERPOLARIZATION INDUCED BY NANOPOROUS AU

3.1 Introduction	46
3.2 Methods	
3.2.1 <i>Computational methods</i>	49
3.2.2 <i>Experimental methods</i>	61
3.3 Results and Discussion	64
3.4 Conclusion	82
References	84

4. ELECTRONIC ORIGIN OF ANTIMICROBIAL ACTIVITY OWING TO SURFACE EFFECT

4.1 Introduction	94
4.2 Methods	
4.2.1 <i>Preparation of npAu and npAu-Pt</i>	96
4.2.2 <i>Bacterial strain</i>	97
4.2.3 <i>Tests of antimicrobial activity (AA)</i>	97
4.2.4 <i>Inductively coupled plasma (ICP) atomic emission spectrophotometry measurements</i>	98
4.2.5 <i>Ultraviolet photoelectron spectrometry (UPS) measurements</i>	99
4.2.6 <i>First-principles calculations of Au surfaces</i>	99
4.2.7 <i>Moleculr dynamics simulation and first-principles calculations of hyperpolarization of peptidoglycan</i>	101
4.3 Results and discussion	104
4.4 Conclusions	116
References	118

5. WEAK INTERACTION CAUSES DYSFUNCTION OF A POTASSIUM ION

CHANNEL

5.1 Introduction	123
5.2 Methods	
5.2.1 <i>Potassium channel interacting with hyperpolarized cell wall</i>	124
5.2.2 <i>Bias-exchange metadynamics simulations</i>	128
5.2.3 <i>First-principles calculations on the selectivity filter</i>	128
5.3 Results and Discussion	131
5.4 Conclusion	143
References	144

6. THE EFFECT OF NANOPOROUS AU ON THE FUNCTIONS OF ATP SYNTHASE

6.1 Introduction	148
6.2 Methods	150
6.3 Results and discussion	155
6.4 Conclusion	160
References	161

7. GENERAL CONCLUSIONS

164

ACKNOWLEDGEMENTS

167

LIST OF PUBLICATIONS

169

CHAPTER1

GENERAL INTRODUCTION

1.1 Introduction

1.1.1 Nanoporous metals and their properties

Nanostructured metallic materials have structural features with typical length scales of nanometers. These materials have been getting more and more attention in many fields including mechanical [1], chemical [2], energetic [3] and biomimetic [4] applications. This is because the nanostructured materials have very different properties from their parent materials. For example, Au nanoparticles with diameters of 2–6 nm exhibit high catalytic activity and tolerance, compared with bulk Au [5]. There are many types of nanostructured metallic materials. Typical nanostructured metals are nanoparticles [6], nanowires [7], nanorods [8], and nanocrystalline metals [9]. These nanostructured metallic materials have been thoroughly investigated because of their peculiar properties.

Nanoporous metals are nanostructured materials with open porous structures containing nanometer-scale pores and ligaments. Figure 1.1 shows scanning electron microscope (SEM) images of nanoporous metals. The first electron microscopy observations of nanoporous metals were reported in 1979–1980 by Forty and Durkin [10,11], and nanoporous metals have since received much interest from researchers in

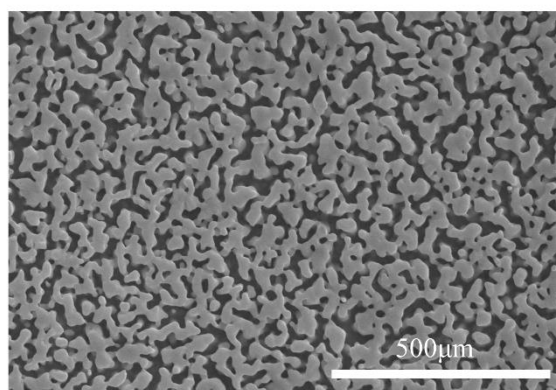


Figure 1.1 Scanning electron microscope (SEM) images of nanoporous Au. The pores and ligaments of nanometer-scale range can be observed.

various fields since. Nanoporous gold (NPG) has been intensively investigated because it is easily fabricated by the dealloying of gold–silver alloys. Figure 1.2 shows the schematic illustrations of fabrication process of NPG by dealloying. Nanoporous structure, as well as other nanostructures (nanoparticles, nanowires, nanorods and nanocrystallinity), gives the peculiar properties that are not seen in the parent bulk metals. For example, piezoelectricity in gaseous [12] and electrochemical [13,14] environments are distinguished features of nanoporous metals and can be applied to sensors and actuators. Also, many researchers have reported that the yield strength of NPG is significantly high due to very small ligament sizes [15-17]. The dependence of mechanical strength on ligament or pore sizes is not seen in conventional porous metals with pore sizes in millimeter and micrometer ranges.

Lattice distortion occurs at the surface of the nanosized ligaments of NPG because of their large curvature. This results in an interesting catalysis behavior of NPG in organic reaction that is not observed in bulk gold. For example, NPG reportedly exhibits catalytic activity in the oxidation of carbon monoxide [18-20] and methanol [21] in contrast to bulk gold. Also, NPG catalytically decomposes methyl orange (MO) which is a kind of an organic azo dye, whereas bulk gold does not. The decomposition kinetics of MO was not simply proportional to the surface area of NPG, which suggests that active sites due to lattice distortion are important in the catalysis by NPG. The self-assembled monolayer (SAM) modified NPG enhanced the catalytic activity of laccase [22]. Thus, NPG strongly affects the stability of the surrounding organic matters.

1.1.2 Antimicrobial properties of nanomaterials

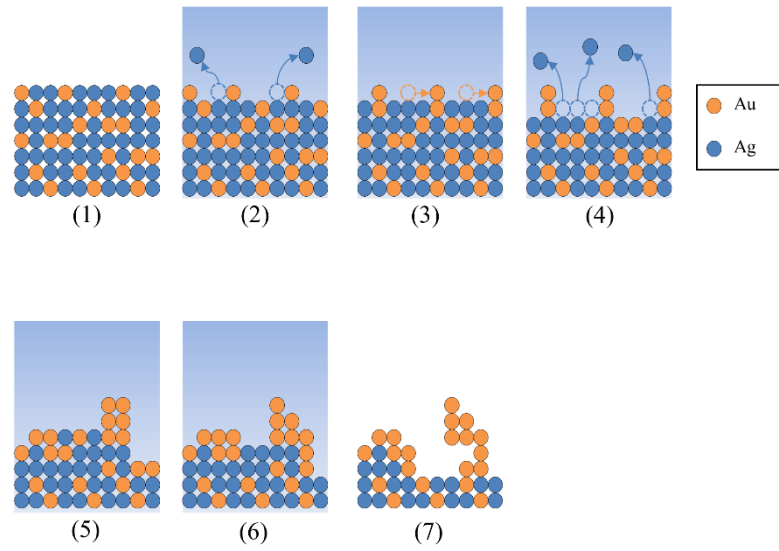


Figure 1.2 Schematic illustrations of fabrication method of nanoporous metals by dealloying. The nanometer-range pores were spontaneously formed in this method.

Remarkable antimicrobial activity (AA) of metallic nanomaterials is one of their representative applications in biological fields. The surface of bacteria plays an important role in the AA of metallic nanomaterials. The surface is composed of the cell wall and the cell membrane (Figure 1.3). The structural and mechanical characteristics of a bacterial cell wall, that is, peptidoglycan have been studied by electron microscopy [23] and molecular dynamics (MD) simulations [24,25]. Peptidoglycan is composed of repeating units consisting of a disaccharide (*i.e.*, N-acetylglucosamine (GlcNAc) and N-acetylmuramic acid (MurNAc)) and a cross-link peptide. The repeating units of a stem (L-Ala-D-iso-Gln-L-Lys-D-Ala-D-Ala) and a bridge (Gly1- Gly2- Gly3 – Gly4 – Gly5) was used as a component of cross-link peptide in the previous study [26]. Schematic illustrations of a disaccharide and a cross-rink peptide are shown in Figures 1.4 and 1.5, respectively.

The 3-dimensional structure of peptidoglycan is still not known although many studies tried to clarify the architecture of peptidoglycan [24,25]. Two major candidates of peptidoglycan structure have been proposed: the layered model [27] and the scaffold model [24,25] (Figure 1.6). In the layered model, glycan chains are arranged parallel to the surface of cell membrane, and glycan chain are arranged vertical on the surface in the scaffold model. It has been shown that the scaffold model well represents the mechanical properties of cell wall, compared with the layered model [24,25].

Many metallic nanomaterials show a remarkable antimicrobial activity through emitting harmful species such as metallic ions and reactive oxygen species (ROS). A. K. Chatterjee et al. [28] reported the AA of Cu nanoparticles through emitting Cu^{2+} ions. Ag

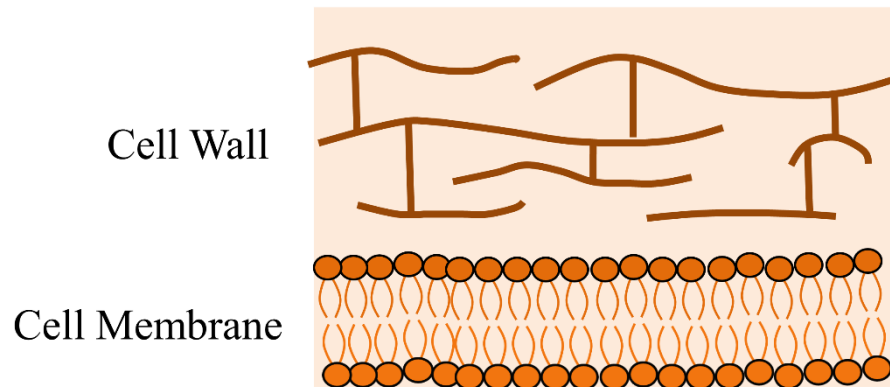


Figure 1.3 Schematic illustrations of surface layer structure of bacteria. The cell wall was located outside of cell membrane. The cell wall protects the cell membrane from turgor pressure.

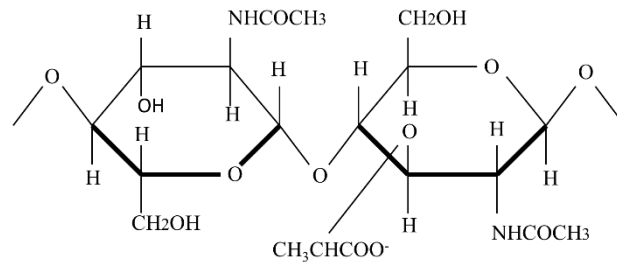


Figure 1.4 The schematic illustrations of GlcNAc (left) and MurNAc (right).

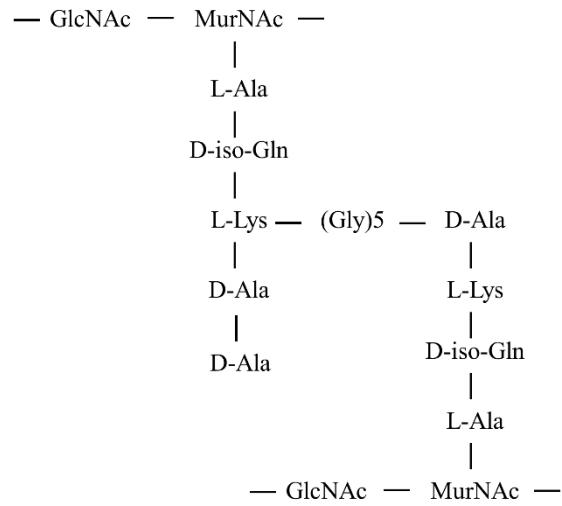


Figure 1.5 The amino-acid sequence of cross-rink peptide in peptidoglycan. The two MurNAc molecules were connected by a peptide.

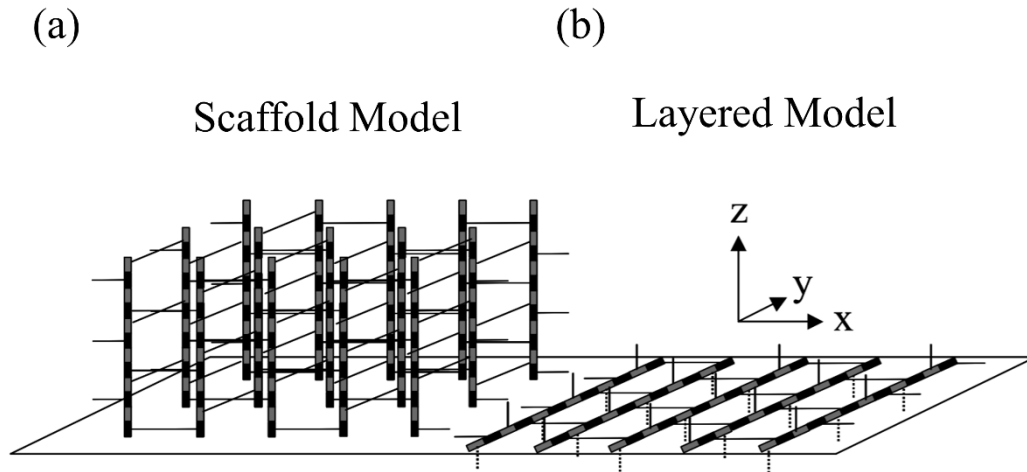


Figure 1.6 The schematic illustrations of (a) Scaffold model and (b) Layered model of peptidoglycan [16]. The glycan vertically stands in scaffold model while the glycan stands in parallel on cell membrane. The scaffold model well represents the mechanical properties of cell wall.

nanoparticles kill bacteria through emitting Ag^+ ions and ROS [29-32]. Many surface-modified nanoparticles show antimicrobial properties with release of ROS [33-36].

Some surface-modified nanoparticles show antimicrobial properties without releasing ROS and metallic ions [37-39]. The mechanisms of their antimicrobial properties are the deterioration of cytoplasmic proteins such as ribosomes by the incorporation of nanoparticles into the cytoplasm of bacteria (Figure 1.7). Positively-charged metallic nanoparticles kill bacteria by direct interactions with cell membrane [40,41]. The characteristic of metallic nanoparticles is that they can pass through the cell wall of bacteria and directly contact with the cell membrane. However, it has been recently reported that nanostructured substrates show AA without releasing ROS nor metallic ions [42-44]. Nanostructured substrates cannot pass through the cell wall because of their bulky dimensions, with typical macroscopic lengths larger than millimeters. Hence, their antimicrobial mechanisms are presumably related to disorder or denaturation of cell walls. However, there are no investigations about the interactions between nanostructured surfaces and the cell wall from the biophysical viewpoint, and the origin of AA of nanostructured surfaces is unknown.

1.1.3 Antimicrobial properties of nanoporous Au

Recently, the antimicrobial property of NPG on *E. coli* and *S. epidermidis* was reported (Figure 1.8) [45]. The characteristics of antimicrobial activity (AA) of NPG are follows: (1) the source of antimicrobial activity of NPG was neither metal ions nor ROS, which

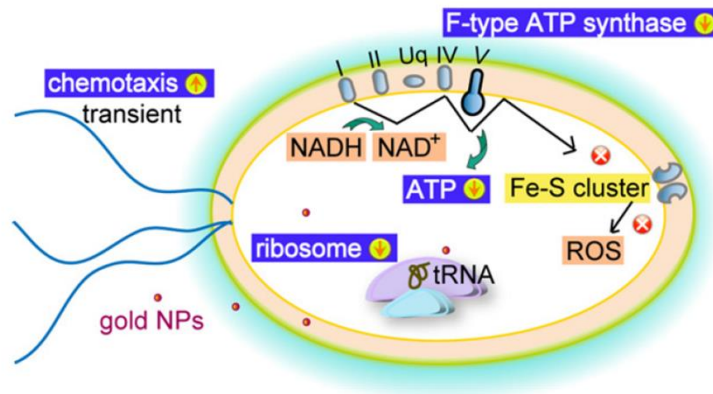
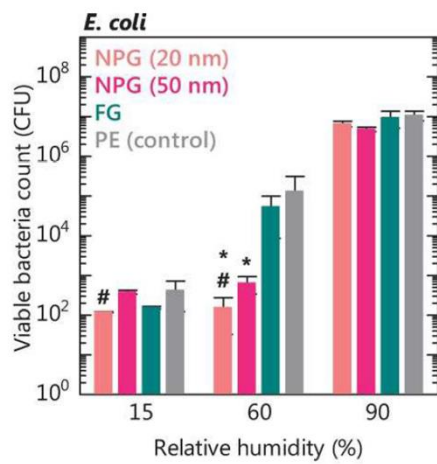


Figure 1.7 The antimicrobial mechanisms of surface-modified nanoparticle. They can easily pass through the cell wall and cell membrane of bacteria. The surface-modified nanoparticle directly deteriorate cytoplasmic proteins such as ribosomes.

(a)



(b)

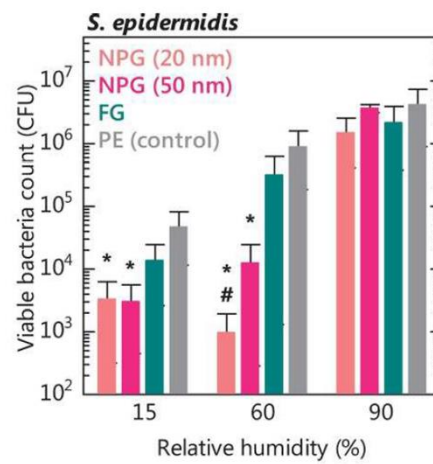


Figure 1.8 The antimicrobial activity (AA) of nanoporous Au against *E. coli* and *S. Epidermidis*. The viable bacteria count (CFU) was lower in nanoporous Au compared with flat Au.

was clarified by inductively-coupled plasma atomic emission spectroscopy and Mercoquant peroxide test, (2) direct contact between bacteria and NPG substrate was necessary for the antimicrobial efficacy of NPG because the antimicrobial activity of NPG was almost zero at the high relative humidity (RH) (=90%) where the frequency of contact between bacteria and substrate was lower than those at other RHs (Figure 1.9), (3) the microarray analyses showed that NPG disturbed the function of cell membrane of *E. coli*, and (4) the measurement of viable bacteria count showed that a long incubation time of 24 h was needed to cause the antimicrobial activity of NPG. From the facts of (2) and (3), the antimicrobial mechanism of NPG is suggested to be composed of two interactions: one between gold surface and cell wall, and the other between cell wall and cell membrane. However, there are poor understandings about the two interactions.

1.1.4 Computational studies of interactions between metals and biomacromolecules

Atomic and electronic computational works are effective ways to investigate the metal-organic matter interactions. There have been many computational studies treating metal-organic matter interactions using molecular dynamics (MD) or first-principles (FP) simulations. These studies used MD-only or FP-only methods. Many interatomic potentials of MD simulation which can calculate metal-organic matter interactions have been proposed, e.g. CHARMM-METAL [46]. MD simulations using these potentials can deal with a large number of atoms more than 1,000,000 atoms and can calculate the overall structures or functions of proteins. However, metal-organic interactions often

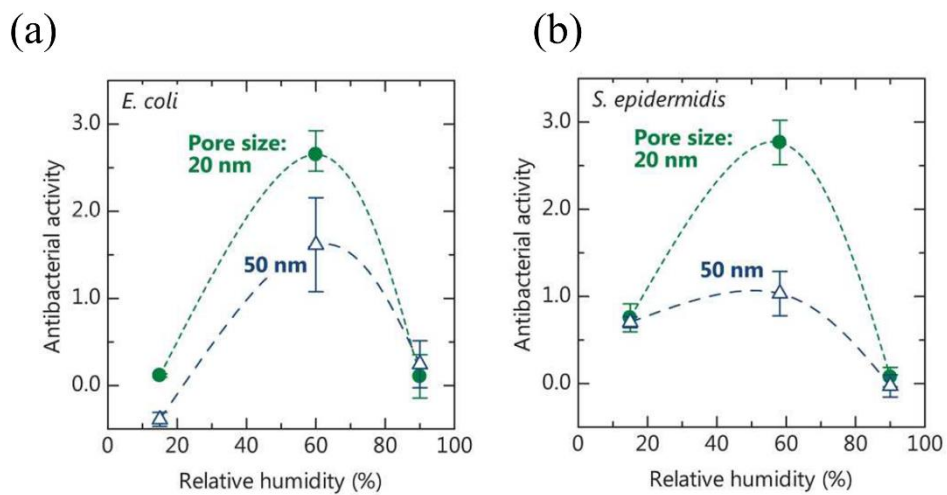


Figure 1.9 The relationship between AA and relative humidity of nanoporous Au for (a) *E. coli* and (b) *S. Epidermidis* [45]. The AA was lower in high relative humidity of 90%. This is because bacteria cannot touch the metallic surfaces in high humidity.

involve electron-related phenomena such as charge transfer and exchange interactions, and MD simulation cannot treat the electron-related phenomena. On the other hand, FP simulation can calculate electronic states of metals and organic matters but can calculate only a few hundreds of atoms. Therefore, previous FP simulations calculated only metal-amino acids interactions. electronic states of metals and organic matters but can only calculate a few hundreds of atoms. Therefore, previous FP simulations only calculated metal-amino acids interactions.

In the present study, I propose a new computational method of combining MD and FP simulations. The schematic illustrations of the methods are shown in Figure 1.10. In the methods, FP simulations calculate only contact area of proteins and MD simulations calculate overall structures and properties of proteins. The amino acids calculated in FP simulation are put back in original positions of proteins. After that, MD simulations calculate the docked proteins. The detailed methods are described in chapter 3. This new simulation method can calculate the interactions between metallic materials and proteins from electronic point of view.

1.2 Scope of the present study

1.2.1 Enhanced enzyme properties of laccase

In chapter 2, the enhanced enzyme properties of laccase immobilized on SAM-modified Au will be described. Laccase is a useful enzyme to decompose various kinds of organic and inorganic molecules. Immobilization of an enzyme such as laccase on a

Molecular dynamics simulation

First-principles calculation

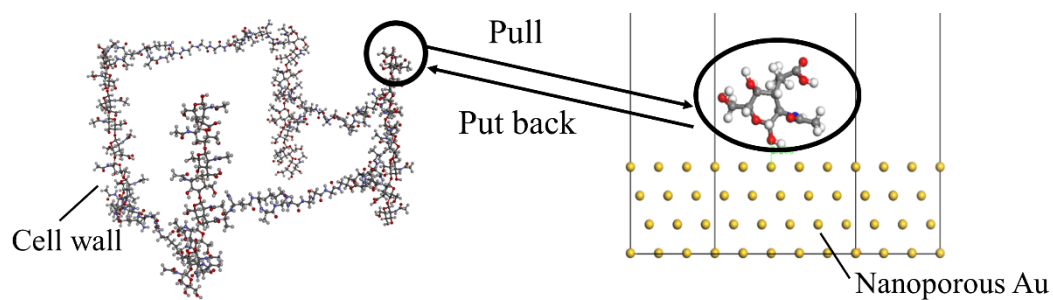


Figure 1.10 The schematic illustrations of the combination of MD simulations and FP simulations. FP simulations calculate only contact area of proteins and MD simulations calculate overall structures and properties of proteins. The amino acids calculated in FP simulation are put back in original positions of proteins. After that, MD simulations calculate the docked proteins.

substrate attracts much attention to enhance enzyme activity of an enzyme. Recently, laccase immobilized on SAM-modified NPG was found to show high enzyme activity at a high temperature of 350K [22]. This should be caused by the strong covalent bonds between SAM and laccase but the detailed mechanism is still unknown. In this chapter, the mechanisms of the enhanced enzyme activity of laccase will be studied using MD simulations.

1.2.2 Antimicrobial properties of nanoporous Au

In chapters 3 to 6, the antimicrobial properties of nanoporous Au will be studied. As discussed above, the AA of nanoporous Au originates from its interactions with cell wall. In chapter 3, effects of nanoporous Au on cell wall of bacteria will be investigated. The combination of MD and FP simulation will show that the cell wall of bacteria will be negatively hyperpolarized. The calculations are conducted based on fluorescent microscopy observation. The mechanical strength of cell wall will be also investigated using first-principles tensile tests based on scanning probe microscopy (SPM) observation. In chapter 4, the origins of hyperpolarization of cell wall caused by nanoporous Au will be discussed. The nanoporous Au-Pt substrate is fabricated and its AA is investigated. The results show that AA is proportional to the work function (WF) of a substrate. The FP simulations show that increased/decreased WF is related to the intense of spilling out of electrons at the surface.

In chapter 5 and 6, effects of hyperpolarized cell wall on functions of membrane proteins will be discussed using MD simulations. The hyperpolarized cell wall affects the

functions of membrane proteins such as ion channel and adenosine triphosphate (ATP) synthase. These membrane proteins play vital roles for bacteria. In chapter 5, effects of hyperpolarized cell wall on potassium ion channel will be discussed. Ionic balance between intracellular and extracellular side of a bacteria is vital for a bacteria. An ion channel is a membrane protein to keep the ionic balance. In chapter 6, effects on ATP synthase will be investigated. An ATP synthase is a membrane protein to synthesize ATP. Thus, to investigate the effect of hyperpolarized cell wall on the functions of ion channel and ATP synthase is important for elucidating AA of NPG.

References

- [1] J. Schiøtz, F. D. Di Tolla, K. W. Jacobsen, “Softening of Nanocrystalline Metals at Very Small Grain Sizes”, *Nature*, **391**(1998), 561-563.
- [2] A. T. Bell, “The Impact of Nanoscience on Heterogeneous Catalysis”, *Science*. **299** (2003), 1688-1691.
- [3] M. S. Whittingham, “Materials Challenges 4Materials Challenges 4”, *MRS Bulletin*. **33** (2008), 411-419.
- [4] I. A. Aksay et al., “Biomimetic Pathways for Assembling Inorganic thin Films”, *Science*. **273** (1996), 892-898.
- [5] M. Haruta M. and M. Daté, “Advances in the Catalysis of Au Nanoparticles”, *Applied Catalysis A: General*. **222** (2001), 427-437.
- [6] N. R. Jana, L. Gearheart and C. J. Murphy, “Wet Chemical Synthesis of High Aspect Ratio Cylindrical Gold Nanorods”, *J. Phys. Chem. B*, **105** (2001), 4065-4067.
- [7] M. Hakamada, T. Matsuzawa, M. Mabuchi, “Fabrication and Catalytic Decoloration Capacity of Nanodendritic Metals”, *Materials Transactions*, **55** (2014), 534-538.
- [8] M. E. McHenry, M. A. Willard, D. E. Laughlin, “Amorphous and Nanocrystalline Materials for Applications as Soft Magnets”, *Progress in Materials Science*, **44** (1999), 291-433.
- [9] Y. Ding, Y.-J. Kim, J. Erlebacher, “Nanoporous Gold Leaf: “Ancient Technology””, *Advanced Materials*, **16** (2004), 1897-1900.

- [10] A. J. Forty, "Corrosion Micromorphology of Noble Metal alloys and Depletion Gilding", *Nature* **282** (1979), 597-598.
- [11] A. J. Forty, and P. Durkin, "A Micromorphological Study of the Dissolution of Silver-Gold Alloys in Nitric Acid", *Philos. Mag. A* **42**, (1980), 295-318.
- [12] J. M. Ghuysen, "Use of Bacteriolytic Enzymes in Determination of Wall Structure and Their Role in Cell Metabolism", *Bacteriological reviews*, **32**, (1968), 425-464.
- [13] M. Beeby, J. C. Gumbart, B. Roux B., G. J. Jensen, "Architecture and Assembly of the Gram-Positive Cell Wall", *Molecular Microbiology*, **88**, (2013), 664-672.
- [14] W. Vollmer, S. J. Seligman, "Architecture of Peptidoglycan: More Data and More Models", *Trends in Microbiology*, **18**, (2010), 59-66.
- [15] B. A. Dmitriev, F. V. Toukach, K.-J. Schaper, O. Holst, E. T. Rietschel, S. Ehlers, "Tertiary Structure of Bacterial Murein: The Scaffold Model", *Journal of Bacteriology*, **185** (2003), 3458-3468.
- [16] W. Vollmer and J. -V. Höltje, "The Architecture of the Murein (Peptidoglycan) in Gram-Negative Bacteria: Vertical Scaffold or Horizontal Layer(s)?", *Journal of Bacteriology*, **186** (2004), 5978-5987.
- [17] R. Ślusarz, M. Szulc and J. Madaj, "Molecular Modeling of Gram-Positive Bacteria Peptidoglycan layer, Selected Glycopeptide Antibiotics and Vancomycin Derivatives Modified with Sugar Moieties", *Carbohydrate Research*, **389** (2014), 154-164.

- [18] S. Kameoka, and A. P. Tsai, "CO Oxidation over a Fine Porous Gold Catalyst Fabricated by Selective Leaching from an Ordered AuCu₃ Intermetallic Compound", *Catal. Lett.* **121** (2008), 337-341.
- [19] V. Zielasek, B. Jurgens, C. Schulz, J. Biener, M. M. Biener, A. V. Hamza, and M. Baumer, "Gold Catalysts: Nanoporous Gold Foams.", *Angew. Chem. Int. Ed.* **45**, (2006) 8241-8244.
- [20] C. Xu, J. Su, X. Xu, P. Liu, H. Zhao, F. Tian, and Y. Ding, "Low Temperature CO Oxidation over Unsupported Nanoporous Gold", *J. Am. Chem. Soc.* **129**, (2007) 42-43.
- [21] A. Wittstock, V. Zielasek, J. Biener, C. M. Friend, and M. Baumer, "Nanoporous Gold Catalysts for Selective Gas-Phase Oxidative Coupling of Methanol at Low Temperature", *Science* **327**, (2010) 319-322.
- [22] M. Hakamada et al., "Electrochemical Stability of Self-Assembled Monolayers on Nanoporous Au.", *Phys Chem Chem Phys* **13** (2011) 12277–12284.
- [23] J. Dubochet et al., "Electron Microscopy of Frozen-Hydrated Bacteria", *Journal of Bacteriology*, **155** (1983) 381-390.
- [24] S.O. Meroueh et al., "Three-Dimensional Structure of the Bacterial Cell Wall Peptidoglycan", *PNAS* **127** (2006) 15397-15407.
- [25] B. Dmitriev, F. Toukach, S. Ehlers, "Towards a Comprehensive View of the Bacterial Cell Wall", *Trends in Microbiology* **13** (2005) 569-574.
- [26] M. Yusupov et al., "Plasma-Induced Destruction of Bacterial Cell Wall Components: A Reactive molecular Dynamics Simulation", *J Phys Chem C*, **117** (2013) 5993-3998.
- [27] J. M. Ghuyssen, "Use of Bacteriolytic Enzymes in Determination of Wall Structure and Their Role in cell Metabolism", *Bacteriological reviews*, **32** (1968) 425-464.

- [28] A. K. Chatterjee, R. Chakraborty and T. Basu, “Mechanism of Antimicrobial Activity of Copper Nanoparticles”, *Nanotechnology*, **25** (2014) 135101–135707.
- [29] L. Z. Zhao et al., “Antibacterial Nano-Structured Titania Coating Incorporated with Silver Nanoparticles”, *Biomaterials* **32**, (2011) 5706–5716.
- [30] O. Choi and Z. Hu, “Size Dependent and Reactive Oxygen Species Related Nanosilver Toxicity to Nitrifying Bacteria”, *Environ. Sci. Technol.* **42**, (2008) 4583–4588.
- [31] C. Beer, R. Foldbjerg, Y. Hayashi, D. S. Sutherland & H. Autrup, “Toxicity of Silver Nanoparticles–Nanoparticle or Silver Ion?” ,*Toxicol. Lett.* **208**, (2012) 286–292.
- [32] E. Navarro et al., “Toxicity of Silver Nanoparticles to *Chlamydomonas Reinhardtii*”, *Environ. Sci. Technol.* **42**, (2008) 8959–8964.
- [33] S. Sadhasivam, P. Shanmugam, M. Veerapandian, R. Subbiah and K. Yun, “Biogenic Synthesis of Multidimensional Gold Nanoparticles Assisted by *Streptomyces Hygroscopicus* and Its Electrochemical and Antibacterial Properties”, *Biometals* **25**, (2012) 351–360.
- [34] Y. Cui et al., “The Molecular Mechanism of Action of Bactericidal Gold Nanoparticles on *Escherichia coli*”, *Biomaterials* **33**, (2012) 2327–2333.
- [35] Y. Zhang, H. Peng, W. Huang, Y. Zhou and D. Yan, “Facile Preparation and Characterization of Highly Antimicrobial Colloid Ag or Au Nanoparticles”, *J. Colloid Interface Sci.* **325**, (2008) 371–376.
- [36] J. F. Hernandez-Sierra et al., “The Antimicrobial Sensitivity of *Streptococcus Mutans* to Nanoparticles of Silver, Zinc Oxide, and Gold.”, *Nanomed.-Nanotechnol. Biol. Med.* **4**, (2008) 237–240.

- [37] J. J. Li, D. Hartono, C.-N. Ong, B.-H. Bay & L.-Y. L. Yung, “Autophagy and Oxidative Stress Associated with Gold Nanoparticles”, *Biomaterials* **31**, (2010) 5996–6003.
- [38] F. U. Khan et al., “Visible Light Inactivation of *E. coli*, Cytotoxicity and ROS Determination of Biochemically Capped Gold Nanoparticles”, *Microbial Pathogenesis* **107**, (2017) 419–424.
- [39] A. Kumar, S. Kumar, W.-K. Rhim, G.-H. Kim and J.-M. Nam, “Oxidative Nanopeeling Chemistry-Based Synthesis and Photodynamic and Photothermal Therapeutic Applications of Plasmonic Core-Petal Nanostructures”, *J. Am. Chem. Soc.* **136**, (2014) 16317–16325.
- [40] L. Mei et al., “Multivalent Polymer-Au Nanocomposites with Cationic Surfaces Displaying Enhanced Antimicrobial Activity”, *Polymer Chemistry* **5**, (2014) 3038–3044.
- [41] Z. V. Feng et al., “Impacts of Gold Nanoparticle Charge and Ligand Type on Surface Binding and Toxicity to Gram-Negative and Gram-Positive Bacteria”, *Chemical Science* **6**, (2015) 5186–5196.
- [42] S. Sadhasivam et al., “Biogenic Synthesis of Multidimensional Gold Nanoparticles Assisted by *Streptomyces Hygroscopicus* and Its Electrochemical and Antibacterial Properties”, *Biometals* **25**, (2012) 351–360.
- [43] Y. Zhang, H. Peng, W. Huang, Y. Zhou and D. Yan, “Facile Preparation and Characterization of Highly Antimicrobial Colloid Ag or Au Nanoparticles”, *J. Colloid Interface Sci.* **325**, (2008) 371–376.

- [44] J. F. Hernandez-Sierra et al., “The Antimicrobial Sensitivity of Streptococcus Mutans to Nanoparticles of Silver, Zinc Oxide, and Gold”, *Nanomed.-Nanotechnol. Biol. Med.* **4**, (2008) 237–240.
- [45] M. Hakamada, S. Taniguchi and M. Mabuchi, “Antimicrobial Activity of Nanoporous Gold Against *Escherichia coli* and *Staphylococcus epidermidis*.”, *J. Mater. Res.* **32**, (2017) 1787-1795.
- [46] H. Heintz, R. A. Vaia, B. L. Farmer and R. R. Naik, “Accurate Simulation of Surfaces and Interfaces of Face-Centered Cubic Metals Using 12-6 and 9-6 Lennard-Jones Potentials”, *J. Phys. Chem. C* **112**, (2008) 17281–17290.

CHAPTER2

MOLECULAR DYNAMICS STUDY OF LACCASE IMMOBILIZED ON SELF-ASSEMBLED MONOLAYER MODIFIED Au

2.1 Introduction

Free-standing nanoporous Au with a large surface area can provide a platform for immobilization of self-assembled monolayers (SAMs) [1–3]. Au strongly bonds to the thiol group of SAM because of covalent bonding between an Au atom and a S atom in the thiol group of SAM [4]. Hakamada et al. [1] showed that the Au–S bond is strengthened by defects at the surfaces of nanoporous Au. Recently, it was found that laccase immobilized on SAM-modified nanoporous Au, where a 4-aminothiophenol (4-ATP) was used as the SAM, exhibited enhanced catalytic activity in the degradation of 2,6-dimethoxyphenol (DMP) at a high temperature of 350 K, compared with non-immobilized laccase [5].

Laccase is a blue multicopper oxidase that contains four copper ions distributed in three sites, which are classified according to their spectroscopic properties, as type 1 Cu for the blue copper center, type 2 Cu for the normal copper center, and type 3 Cu for the coupled binuclear copper center. Type 1 (T1) Cu is the primary acceptor of electrons from a reducing substrate. Laccase is a useful enzyme that is capable of oxidizing a large number of organic and inorganic substrates [6], and it has received significant attention regarding its potential applications in the fields of biosensors and biofuel cells [7–9]. High stabilization of laccase at high temperature is important for such applications. Miyazaki [10] found that a hyperthermophilic laccase was produced by cloning the gene. Immobilization of laccase by a SAM is also one of methods for processing thermophilic laccase, as mentioned above. The immobilization of laccase by a SAM is promising for commercial applications because of its low cost. However, the origin of the enhanced catalytic activity at high temperature of laccase immobilized by a SAM is not understood at all.

In the present work, molecular dynamics (MD) simulations and docking simulations of laccase immobilized by 4-ATP were performed to understand the origin of the enhanced catalytic activity at high temperature. First, the bonding energy of laccase with

4-ATP was investigated at 300 and 350 K. Then, the docking of DMP to laccase was simulated.

2.2 Methods

MD simulations of the bonding of laccase with and without 4-ATP were carried out using Discovery Studio 4.0, using the CHARMM force field [11]. The crystal structure of laccase (PDB ID: 1V10 [12]) was obtained from the Protein Data Bank [13]. Laccase was immersed in a spherical water solvation where the number of water molecules was about 6,000 and the diameter of the sphere was 40 nm. The time step of the MD simulation was 1fs. The system was first energy-minimized using the steepest decent algorithm (200,000 steps) followed by the conjugate gradient method (200,000 steps). The system was gradually heated from 50 to 300 and 350 K for 2 ps, respectively. The system was equilibrated for 1 ns with constant number of particles, volume, and temperature (NVT) ensemble, where Berendsen's weak coupling scheme [14] was used to achieve constant temperature dynamics. Finally, 10 ns NVT simulations were performed. Laccase bonds with 4-ATP by formation of an amide bond between an amino group of 4-ATP and a

carboxyl group of laccase [15,16]. In the present study, acidic amino acids positioned on the surface of laccase and C-terminal were bonded with 4-ATP. The amino acid in laccase that would most likely bond with 4-ATP was determined to be Glu91 because the lowest bonding energy was obtained for the bond between Glu91 and 4-ATP (Table 1). A schematic illustration of the amide bond between the amino group of 4-ATP and the carboxyl group of laccase is shown in Fig. 2.1. The bonding energy of laccase and 4-ATP is given by

$$E_b = E_{\text{laccase+4ATP}} - E_{\text{laccase}} - E_{\text{4ATP}}, \quad (2.1)$$

where E_b is the binding energy, and $E_{\text{laccase+4ATP}}$, E_{laccase} and E_{4ATP} , are the average internal energies of 10ns NVT simulations of laccase with 4-ATP, laccase, and 4-ATP, respectively. The bonding energies at 300 and 350 K were calculated by eq. (2.1).

For docking simulations of DMP to laccase, AutoDock 4.2 software [17] was used to generate an ensemble of docked conformations for DMP and laccase. The Lamarckian genetic algorithm was used for all the molecular docking simulations and the following parameters were used; a random population of substrate conformations in up to 100 arbitrary orientations, a mutation rate of 0.02, and a crossover rate of 0.8. Simulations were carried out considering 2.5 million energy evaluations with a maximum of 27,000

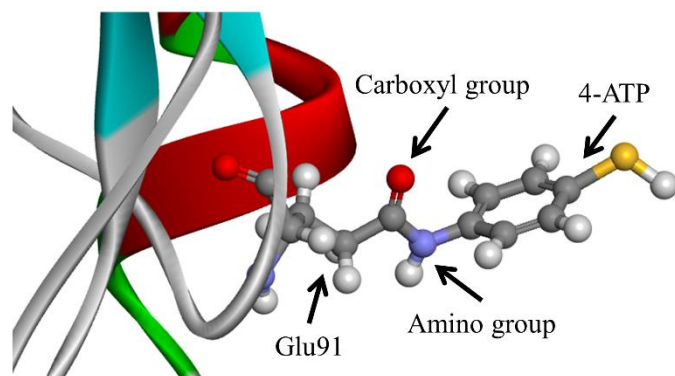


Figure 2.1 Illustration of the amide bond between the amino group of 4-ATP and a carboxyl group of laccase at 300 K. The amino acid in laccase is Glu91.

generations. The docking site of DMP was determined to be T1 site because the substrate is reduced by T1 Cu and a previous study found that T1 site is the most energetically stable site for docking of a substrate to laccase [18]. The grid box composed of 40×40×40 grid points with a spacing between each grid point of 0.375 Å was centered a T1 Cu. Laccase and Cu were rigid during docking simulations.

The hydrophobic energy was calculated using Poisson-Boltzmann solvent accessible surface area (MM-PBSA) method [19]. The 5 models were evenly extracted from the last 100 ps MD trajectories to calculate the hydrophobic interaction energy between laccase and DMP. The hydrophobic interaction energy can be calculated by

$$E_h = E_{h,\text{laccase+DMP}} - E_{h,\text{laccase}} - E_{h,\text{DMP}}, \quad (2.2)$$

where E_h is hydrophobic interaction energy, $E_{h,\text{laccase+DMP}}$ is hydrophobic energy of laccase with DMP, $E_{h,\text{laccase}}$ is hydrophobic energy of laccase and $E_{h,\text{DMP}}$ is hydrophobic energy of DMP. In the MM-PBSA calculation, a grid spacing of 0.5 Å was employed and the relative dielectric constant was set to 80 at the exterior and 1.0 at the interior of DMP-laccase complex.

After the docking simulations, the energy minimization, 1ns NVT equilibration and 10ns NVT simulations described above were performed again on the laccase with and without 4-ATP docked with DMP, respectively.

2.3 Results and discussion

Fig. 2.2 shows variations in root-mean square deviation (RMSD) of atomic positions as a function of the calculation time for laccase with and without 4-ATP at 300 and 350K before docking with DMP, respectively, in which the RMSD is given by

$$\text{RMSD} = \sqrt{\frac{1}{n} \sum (x_i - x_0)^2} , \quad (2.3)$$

where x_0 is the initial atomic position, x_i is the atomic position during the simulation, and n is the number of atoms, respectively. The RMSD value was nearly constant after 8 ns and thus the structures of laccase were stable. The bonding energy of laccase with 4-ATP was -47.1 kcal/mol at 300 K and was -42.2 kcal/mol at 350 K, respectively. Thus, laccase was stabilized by bonding with 4-ATP.

Fig. 2.3 shows the superposition of a part of laccase with and without 4-ATP, respectively. The structures of laccase did not overlap at 350 K, while they overlapped at

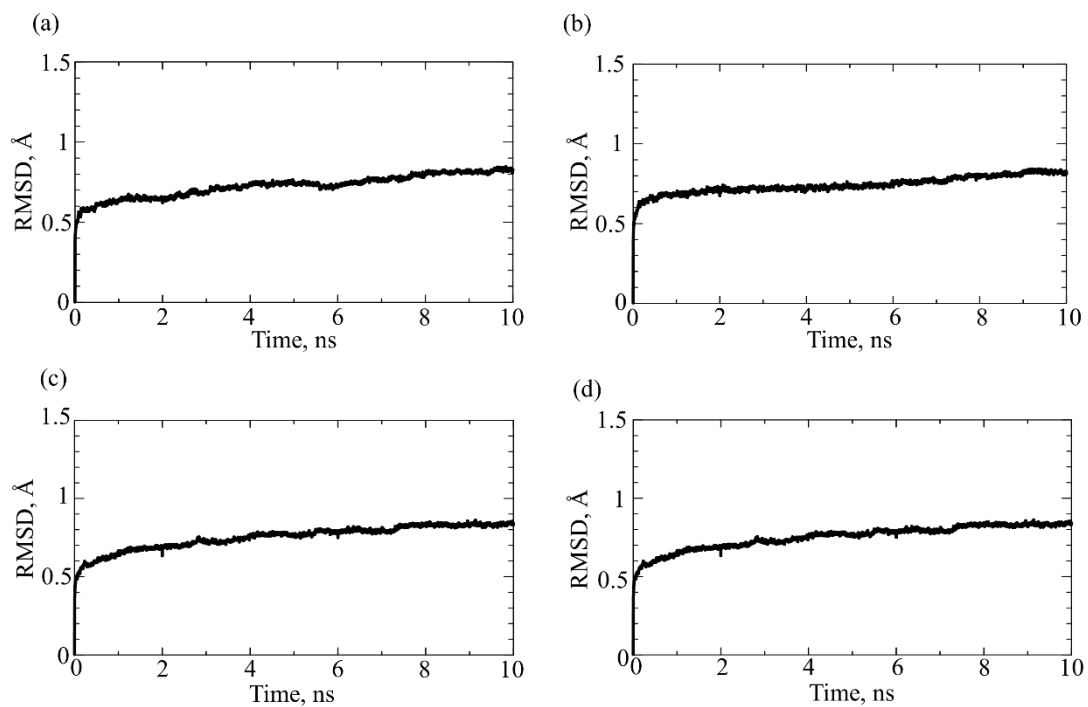


Figure 2.2 Variations in RMSD value as a function of calculation time for laccase with and without 4-ATP, (a) laccase without 4-ATP at 300 K, (b) laccase without 4-ATP at 350 K, (c) laccase with 4-ATP at 300 K and (d) laccase with 4-ATP at 350 K. The RMSD value becomes nearly constant after 8ns.

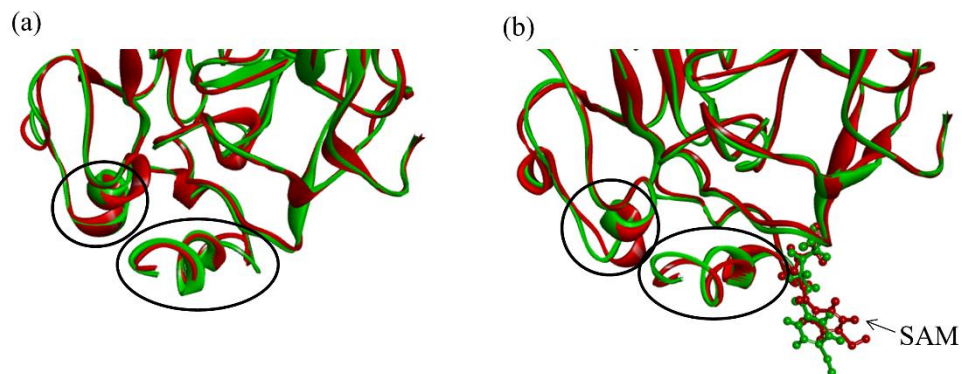


Figure 2.3 Snapshots of superposition of parts of laccase with and without 4-ATP after MD simulation at (a) 300 K and (b) 350 K. The part of laccase with and without 4-ATP after the stabilization calculations are shown in red and green, respectively. The structure of laccase does not overlap at 350 K, while they overlap at 300 K, as shown by circles.

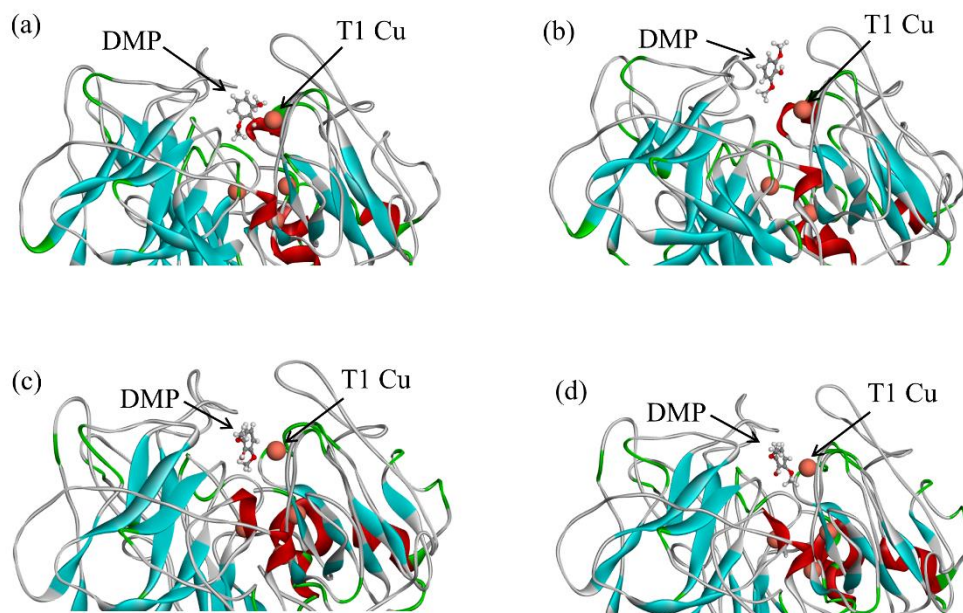


Figure 2.4 Snapshots of conformation of laccase docked with DMP after MD simulation, (a) laccase without 4-ATP at 300 K, (b) laccase without 4-ATP at 350 K, (c) laccase with 4-ATP at 300 K and (d) laccase with 4-ATP at 350 K. DMP is docked at T1 pocket.

300 K, as shown by circles in Fig. 2.3. Thus, the structure of laccase changed more by bonding with 4-ATP at 350 K than at 300 K. The conformation change leads to a variation in internal energy [20,21]. Therefore, it is suggested that the enhanced stabilization of laccase at 350 K by bonding with 4-ATP is because of the structural change of laccase.

Fig. 2.4 shows snapshots of laccase docked with DMP. DMP was docked near T1 Cu in all the cases. Some studies [22-24] suggested that structural change of laccase led to the low catalytic activity because the size of docking site became small. Hence, it is worthwhile to investigate a variation in size of T1 site. Fig. 2.5 shows variations in T1 site size as a function of calculation time, where the T1 site size is defined as a diameter of a sphere which contains amino acids around T1 copper (His396, His457, Cys452 and Leu462). The average size of T1 site was 15.3 Å for laccase without 4-ATP at 300 K, 15.6 Å for laccase without 4-ATP at 350 K, 15.3 Å for laccase with 4-ATP at 300 K and 14.8 Å for laccase with 4-ATP at 350 K, respectively. The dimensions of DMP molecule are 8.8 Å along the long axis and 5.2 Å along the short axis. Although the T1 site size for laccase with 4-ATP at 350 K was smaller than that for laccase without 4-ATP at 350 K, a difference of the size was minor considering the dimensions of DMP molecule.

Therefore, the enhanced catalytic activity of laccase with 4-ATP is unlikely to be related to the variation in T1 site size.

The hydrophobic interaction may play a vital role in an interaction between laccase and DMP because nonpolar amino acids such as Cys452 and Leu462 are located near T1 pocket [25]. Fig. 2.6 shows the hydrophobic interaction energy between laccase and DMP. It is noted that the hydrophobic interaction energy for laccase with 4-ATP was increased by a temperature increase from 300 to 350 K, while it for laccase without 4-ATP was decreased by the temperature increase. Therefore, it is suggested that the enhanced

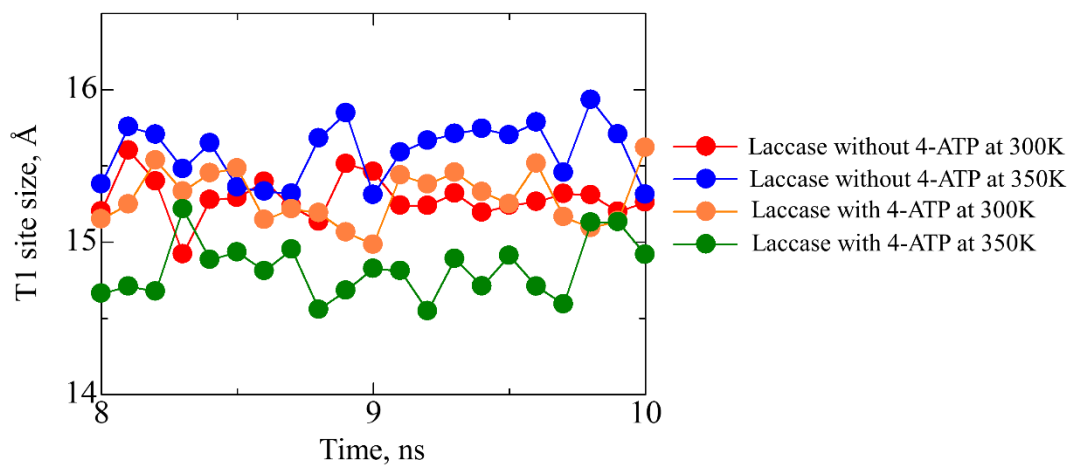


Figure 2.5 Variations in T1 site size as a function of calculation time. The T1 site size is defined as a diameter of a sphere which is drawn by approximating a receptor range containing His396, His457, Cys452 and Leu462.

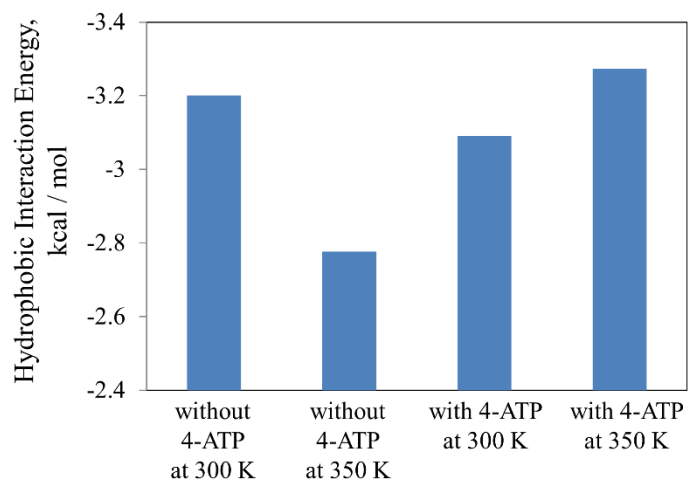


Figure 2.6 Hydrophobic interaction energy between laccase and DMP. Hydrophobic interaction energy decreases from 300 to 350 K for laccase without 4-ATP and increases for laccase with 4-ATP.

catalytic activity of laccase with 4-ATP is attributed to an enhancement in hydrophobic interaction.

A trade-off often occurs between the catalytic performance and the stability of laccase [26-28]. However, laccase immobilized by 4-ATP showed both high stability and high catalytic performance. Tokuriki et al. [28] noted that mutations that modulate enzymatic functions mostly destabilize, and mutations that stabilize seldom evolve enhanced enzymatic activity. The present work, however, suggests that structural changes caused by bonding with 4-ATP lead to the simultaneous high stability and high catalytic performance of laccase.

2.4 Conclusions

MD simulations and docking simulations of laccase immobilized on 4-ATP were performed to understand the origin of the enhanced catalytic activity at 350 K of laccase immobilized by a SAM. Laccase was stabilized by bonding with 4-ATP. The hydrophobic interaction energy between 2,6-dimethoxyphenol (DMP) and laccase was increased by bonding with 4-ATP. On the other hand, the variation in docking site size was minor

considering the dimensions of DMP molecule. Therefore, it is suggested that the enhanced catalytic activity of laccase with 4-ATP is attributed to the high hydrophobic interaction energy between laccase and DMP.

References

- [1] M. Hakamada, M. Takahashi, T. Furukawa, K. Tajima, K. Yoshimura, Y. Chino and M. Mabuchi, (2011) “Electrochemical Stability of Self-Assembled Monolayers on Nanoporous Au”, *Phys Chem Chem Phys.* **13** (2011), 12277–12284.
- [2] O. V. Shulga, et al., “Preparation and Characterization of Porous Gold and Its Application as A Platform for Immobilization of Acetylcholine Esterase”, *Chem Mater.* **19** (2007) 3902–3911.
- [3] H. Qin, C. Xu, X. Huang, Y. Ding, Y. Qu and P. Gao, “Immobilization of Laccase on Nanoporous Gold: Comparative Studies on the Immobilization Strategies and the Particle Size Effect”, *J Phys Chem. C* **113** (2009) 2521–2525.
- [4] F. Tielens and E. Santos, “AuS and SH Bond Formation/Breaking During the Formation of Alkanethiol SAMs on Au (111): a Theoretical Study”, *J. Phys Chem. C* **114**, (2010) 9444–9452.
- [5] M. Hakamada, M. Takahashi and M. Mabuchi, (2012) “Enhanced Thermal Stability of Laccase Immobilized on Monolayer-Modified Nanoporous Au”, *Mater Lett.* **66** (2012) 4–6.

- [6] A. Yaropolov, O. V. Skorobogat'ko, S. S. Vartanov and S. D. Varfolomeyev, "Laccase Properties, Catalytic Mechanism, and Applicability", *Appl Biochem Biotechnol.* **49** (1994) 257–280.
- [7] G. Gupta, V. Rajendran and P. Atanassov, "Laccase biosensor on monolayer-modified gold electrode", *Electroanalysis* **20** (2003) 1577–1583.
- [8] M. L. Mena, V. Carralero, A. González-Cortés, P. Yáñez-Sedeño and K. M. Pingarrón, "Laccase biosensor based on N-succinimidyl-3-thiopropionate-functionalized gold electrodes", *Electroanalysis* **23** (2005) 2147–2155.
- [9] L. Deng, F. Wang, H. Chen, L. Shang, L. Wang, T. Wang and D. Shaojun, "A Biofuel Cell with Enhanced Performance by Multilayer Biocatalyst Immobilized on Highly Ordered Macroporous Electrode", *Biosens Bioelectron.* **24** (2008) 329–333.
- [10] K. Miyazaki, "A Hyperthermophilic Laccase from *Thermus Thermophilus* HB27", *Extremophiles* **9** (2005) 415–425.
- [11] A. D. MacJerrell Jr, D. Bashford and M. Bellott et al, "All-Atom Empirical Potential for Molecular Modeling and Dynamics Studies of Proteins", *J Phys Chem. B* **102** (1998) 3586–3616.

- [12] S. Garavaglia et al., “The Structure of Rigidoporus Lignosus Laccase Containing a Full Complement of Copper Ions, Reveals an Asymmetrical Arrangement for the T3 Copper Pair”, *J Mol Biol.* **342** (2004) 1519–1531.
- [13] H. M. Berman et al, “The protein data bank”, *Nucleic Acids Res.* **28** (2001) 235–242.
- [14] H. J. C. Berendsen, J. P. M. Postma, A. DiNola and J. R. Haak, “Molecular Dynamics with Coupling to an External Bath”, *J. Chem. Phys.* **81** (1984) 3684-3690.
- [15] C. V. Dominguez, M. Pita, A. L. De Lacey, S. Shleev and A. Cuesta, “Combined ATR-SEIRAS and EC-STM Study of the Immobilization of Laccase on Chemically Modified Au Electrodes”, *J. Phys. Chem. C* **116** (2012) 16532–16540.
- [16] G. Gupta, V. Rajendran and P. Atanassov, “Bioelectrocatalysis of Oxygen Reduction Reaction by Laccase on Gold Electrodes, *Electroanalysis* **16** (2004) 1182–1185.
- [17] G. M. Morris, R. Huey, W. Lindstrom, M. F. Sanner, R. K. Belew, D. S. Goodsell and A. J. Olson, “AutoDock4 and AutodockTools4: automated docking with selective receptor flexibility”, *J. Comput. Chem.* **30** (2009) 1639-1662.

- [18] C. Martinez-Sotres, J. G. Rutiaga-Quinones, R. Herrera-Bucio, G. Gallo and P. Lopez-Albarran, “Molecular Docking Insights into the Inhibition of Laccase Activity by Medicarpin”, *Wood. Sci. Technol.* **49** (2015) 857-868.
- [19] J. Srinivasan, T. E. Cheatham, P. Cieplak, P. A. Kollman and D. A. Case, “Continuum Solvent Studies of the Stability of DNA, RNA, and Phosphoramidate—DNA Helices”, *J. Am. Chem. Soc.*, **120** (1998) 9401–9409.
- [20] S. R. Trevino, S. Schaefer, J. M. Scholtz and C. N. Pace, “Increasing Protein Conformational Stability by Optimizing Beta-Turn Sequence”, *J. Mol. Biol.* **373** (2007) 211–218.
- [21] H. Fu, G. R. Grimsley, A. Razvi, J. M. Scholtz and C. N. Pace, “Increasing Protein Stability by Improving Beta-Turns”, *Proteins* **77** (2009) 491–498.
- [22] F. Wang, C. Guo, H. -Z. Liu and C. -Z. Liu, “Immobilization of Pycnoporou Sanguineus Laccase by Metal Affinity Adsorption on Magnetic Chelator Particles”, *J. Chem. Technol. Biotech.* **83** (2008) 97-104.
- [23] G. Bayramoglu, M. Yilmaz and M. Y. Arica, (2010) “Preparation and Characterization of Epoxy-Functionalized Magnetic Chitosan Beads: Laccase

Immobilized for Degradation of Reactive Dyes”, *Bioprocess Biosyst. Eng.* **33** (2010) 439-448.

[24] R. A. Fernandes, A. L. Daniel-da-Silva, A. P. M. Tavares and A. M. R. B. Xavier, “EDTA-Cu(II) Chelating Magnetic Nanoparticles as a Support for Laccase Immobilization”, *Chem. Eng. Sci.* **158** (2017) 599-605.

[25] S. Garavaglia, M. T. Cambria and M. Miqilio et al., “The Structure of Rigidporous Lignisus Laccase Containing a Full Complement of Copper Ions, Reveals an Asymmetrical Arrangement for the T3 Copper Pair”, *J. Mol. Biol.* **342** (2004) 1519-1531.

[26] F. Autore, C. Del Vecchio, F. Fraternali, P. Giardina, G. Sannia and V. Faraco, “Molecular Determinants of Peculiar Properties of a *Pleurotus Ostreatus* Laccase: Analysis by Site-Directed Mutagenesis”, *Enzyme Micro Tech.* **45** (2009) 507–513.

[27] C. Vieille and G. J. Zeikus, “Hyperthermophilic Enzymes: Sources, Uses, and Molecular Mechanisms for Thermostability”, *Microbial Mol Bio Rev.* **65** (2001) 1–43.

[28] N. Tokuriki, F. Stricher, L. Serrano and D. S. Tawfik, “How protein stability and new functions trade off”, *PLoS Comput. Biol.*, **4** (2008) e1000002 1-7.

CHAPTER3

ANTIMICROBIAL MECHANISMS DUE TO HYPERPOLARIZATION INDUCED BY NANOPOROUS Au

3.1 Introduction

Bacteria such as *Escherichia coli* (*E. coli*) and *Staphylococcus epidermidis* (*S. epidermidis*) sometimes cause harmful effects to humans: for example, *E. coli* behaves as an etiologic agent when it intrudes into blood vessels or urinary system. As discussed in chapter 1, many nanomaterials of metal-free photocatalysts [1], Ag and Cu nanoparticles [2-6] and so on [7-9] show a remarkable ability to kill bacteria by the release of diverse antimicrobial species, such as reactive oxygen species (ROS) and metallic ions. Some surface-modified nanoparticles exhibit prominent antimicrobial activities without the release of the harmful diffusive species [10-13], although some surface-modified nanoparticles show antimicrobial activities with the release of ROS [14-16]. In the case of the surface-modified nanoparticles without the release of the harmful diffusive species,

the mechanism of antimicrobial activity is the deterioration of cytoplasmic proteins, such as ribosomes, by the incorporation of nanoparticles into the cytoplasm of bacteria. Also, positively-charged metallic nanoparticles exhibit antimicrobial properties by direct interactions with the cell membrane [17,18]. The antimicrobial mechanisms of these nanomaterials are related to the functional disorders of cell membrane or cytoplasmic proteins, rather than of cell walls, through which the nanomaterials can easily pass. Hence, their antimicrobial mechanisms are presumably related to disorder or denaturation of cell walls. However, there are no investigations from the biophysical viewpoint about the interactions between nanostructured surfaces and the cell wall, and the origin of the antimicrobial activity of nanostructured surfaces is unknown.

Recently, nanoporous Au (NPG), which has an open porous structure with pores and ligaments in the nanometer range [23], was found to exhibit antimicrobial properties against *E. coli* and *S. epidermidis* [24]. In this case as well, its antimicrobial activity must be related to interactions between nanostructured surfaces and the cell wall because monolithic NPG cannot pass through cell walls of bacteria. There were peculiarities for the antimicrobial activity of NPG as follows: (1) the source of antimicrobial activity of NPG was neither metal ions nor ROS, (2) direct contact between bacteria and NPG

substrate was necessary for the antimicrobial efficacy of NPG, (3) NPG disturbed the function of cell membrane of *E. coli*, and (4) a long incubation time of 24 h was needed to cause the antimicrobial activity of NPG. From (2) and (3), the antimicrobial mechanism of NPG is supposed to be composed of two interactions: one between gold surface and cell wall, and the other between cell wall and cell membrane. The large lattice strains of NPG induce hyperpolarization at the surface, as shown later. Hence, the antimicrobial activity of NPG may be a result of interactions related to the hyperpolarization induced by NPG. Also, cytoplasm was leaked for bacteria killed by NPG [24]. This fact suggests that the strength of cell walls may be altered by interactions with NPG. Hence, in the present study, the interactions between NPG and *E. coli* are investigated from the viewpoint of hyperpolarization and strength of the cell wall using the combination of molecular dynamics simulations and first-principles calculations based on experiments. The calculations were based on the following experimental results. In regard to the hyperpolarization, fluorescent microscopic observation experiment was used to study *E. coli* cultured on flat Au (FG) and NPG. Nanoporous metals have large tensile and compressive lattice strains up to 10% at the surface, because the nanosized ligaments have high positive and negative curvatures [25-28]. In regard to the strength of the cell wall,

the elastic moduli of the cell walls of *E. coli* were experimentally measured by scanning probe microscopy (SPM), and the elastic modulus of peptidoglycan, a major component of the cell wall, was calculated by MD simulations. These experiments and simulations shed light on the interactions between Au surface and cell wall. Next, effects of the hyperpolarization on lipid bilayer and on potassium channel were investigated by MD simulations, providing insights into the interactions between the cell wall and cell membrane. As will be discussed, the hyperpolarization plays a critical role in both interactions. Previously, MD simulations of the interactions between organic molecules and metallic surfaces have used empirical potentials such as CHARMM-METAL [29]. However, the empirical potentials cannot treat the effects of charge transfer and exchange interactions. Thus, in the present work, cooperation of MD simulations and first principle calculations was used for investigating the hyperpolarization. This computational strategy allows a deeper understanding of the role of hyperpolarization in antimicrobial activity.

3.2 Methods

3.2.1 Computational methods

A bacterial cell wall consists of a network of peptidoglycan. The structural characteristics of peptidoglycan have been studied by electron microscopy [30] and molecular dynamics (MD) simulations [31,32]. Peptidoglycan is composed of repeating units consisting of a disaccharide (*i.e.*, N-acetylglucosamine (GlcNAc) and N-acetylmuramic acid (MurNAc)) and a cross-link peptide. In the present study, repeating units of a stem (L-Ala-D-iso-Gln-L-Lys-D-Ala-D-Ala) and a bridge (Gly1- Gly2- Gly3 – Gly4 – Gly5) were selected as a component of cross-link peptide in accordance with the previous study [33].

The 3-dimensional structure of peptidoglycan is still not known although many studies tried to clarify the architecture of peptidoglycan [31,32]. Two major candidates of peptidoglycan structure have been proposed: the layered model [34] and the scaffold model [31,32]. It has been shown that the scaffold model well represents the mechanical properties of cell wall, compared with the layered model [31,32]. Thus, the scaffold model was used in the present study.

The components (*i.e.*, a disaccharide and a cross-link peptide) of peptidoglycan were constructed and the geometry optimizations were performed using the Gaussian program

package. Four GlcNAc-MurNAc disaccharides were connected each other and the pentapeptides and the pentaglycine were attached to the glycan chains to construct the cross-link structure. Thereafter, a terminal of pentapeptides was connected to another GlcNAc-MurNAc strand, and then MurNAc molecule, which was not still connected to the cross-link structure in GlcNAc-MurNAc strand, was connected to other pentapeptides and pentaglycine. By repeating this process, a scaffold model of peptidoglycan was constructed.

Energy minimizations and MD calculations were performed to obtain a stabilized structure of peptidoglycan by the Discovery studio 4.0 software (Biovia Inc, San Diego, CA), using the CHARMM forcefield [35]. The peptidoglycan was immersed in a spherical water solvation. The center of water solvent was positioned at the mass center of peptidoglycan and the diameter of spherical solvent water was 50.0 nm. Counter ions of 43 Na⁺ and 43 Cl⁻ were added to neutralize the system. The system was energy-minimized using the steepest decent algorithm (200,000 steps) and the conjugate gradient algorithm (100,000 steps). MD simulations were performed with the time step of 2.0 fs. The system was gradually heated from 5 to 300K for 4ps to activate thermal motion in the system. The system was equilibrated for 1ns to obtain a stable structure of

peptidoglycan with the constant number of particles, volume and temperature (NVT) ensemble. Finally, the 10ns NVT simulations were performed. The peptidoglycan model obtained by the MD simulations is shown in Fig. 3.1.

An interaction between MurNAc, which is a part of peptidoglycan, and a surface of flat Au (FG) or nanoporous Au (NPG) was investigated by first principles calculations.

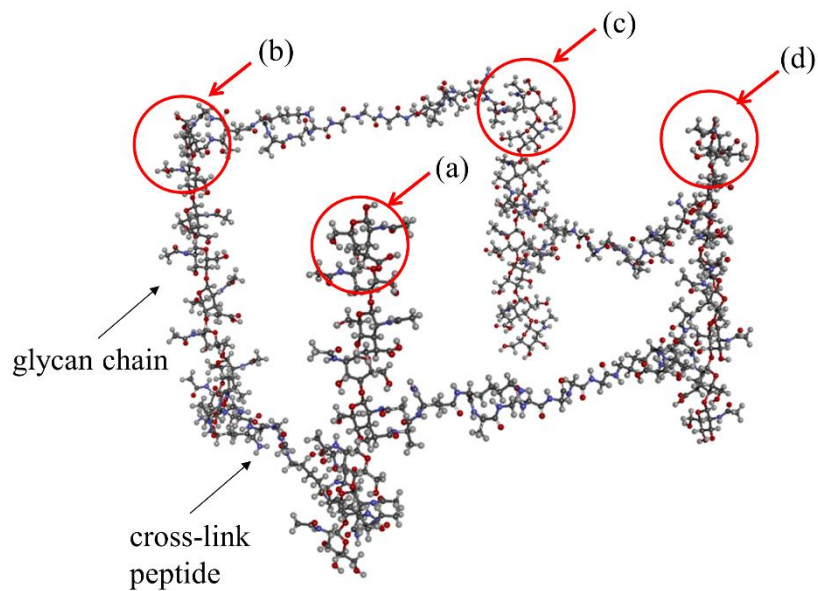


Figure 3.1 A peptidoglycan model after stability computation with 10ns NVT calculation. Gray, red, blue and white spheres show carbon, oxygen, nitrogen and hydrogen atoms, respectively. Four glycan chains are connected by cross-link peptide. Red circles (a)-(d) indicate parts of peptidoglycan calculated by first principles tensile tests (Fig. 3.2). The parts are the one adsorbed on NPG.

A (111) FG model with a surface unit cell of $4\sqrt{3} \times 3\sqrt{3}$ was used, where the lattice strain of the FG model was 0%. The model cell consisted of four (111) Au layers and contained 144 Au atoms. The vacuum gap of 15 Å was added to create the surface. In NPG, large lattice strains exist at its surface. Thus, a lattice strain of +5% or -5% was loaded into the (111) layers of the FG model and two NPG models were constructed: NPG (+5% strain) and NPG (-5% strain).

The geometry optimization calculations were performed on the FG and the NPG models by first principles calculations using the Dmol3 code [36,37]. In the DMol3 method, the physical wave functions were expanded in terms of the accurate numerical basis sets. The exchange-correlation energies were treated according to the generalized gradient approximation (GGA) with the Perdew-Wang 1991 (PW91) approximation [38] to deal with the core (DNP). The ultrasoft pseudopotentials [39] represented in reciprocal space were used for all elements in the calculations. Optical Bloch equation (OBE) calculations were used to set the van der Waals interactions into calculations. A Fermi smearing of 0.005 hartree (1 hartree = 27.2114 eV) was adopted. The tolerances of energy, gradient, and displacement convergence were 1.0×10^{-5} hartree, 2.0×10^{-3} hartree/Å, and 5×10^{-3} Å, respectively. The Brillouin zone of $2 \times 2 \times 1$ using a Monkhorst–Pack k-point

mesh [40] was used. The geometry optimization calculations were carried out with spin polarization. The bottom two layers of the FG and the NPG models were frozen during geometry optimization calculations. The Au surface was assumed to make contacts with the front edge of a disaccharide because glycan chains stood vertically on the surface of cell membrane in the scaffold model. Thus, the MurNAc, which is located at the edge of a glycan chain, was putted on the FG and the two NPG models (+5% and -5% strains).

MurNAc was positioned on fcc, hcp, atop and bridge sites of the FG model and the geometry optimization calculations were performed on the four sites using the first principles calculations. The lowest value of adsorption energy was obtained in the case of the atop site. Thus, the position of MurNAc was determined to be the atop site for all the models.

After the geometry optimizations of MurNAc molecule on the atop site for the FG and the NPG models, each MurNAc was put back at the same position in the original peptidoglycan model and 1 ns MD simulations were performed again, where the atomic positions of MurNAc molecule were not relaxed during the calculations.

After the MD simulations about peptidoglycan, the electrostatic potentials of obtained peptidoglycan were calculated by solving the Poisson Boltzmann equation using

the finite difference method implemented in Delphi program [41,42] with the Discovery studio 4.0. The values of atomic radii and partial atomic charges were taken from the CHARMM parameter set. The peptidoglycan was divided into a three-dimensional cubical grid and the electrostatic potential at each grid point was computed.

First principles tensile tests with the Dmol3 code [36,37] were performed to investigate effects of the hyperpolarization of peptidoglycan on the elastic modulus. Four parts of peptidoglycan shown by arrows in Fig. 3.1, which were absorbed on NPG, were investigated. The distance between two oxygen atoms shown by arrows in Fig. 3.2 was increased by 1% strain without relaxation. This operation was repeated to 8% strain. The exchange-correlation energies were treated according to the generalized gradient approximation (GGA) with the Perdew-Wang 1991 (PW91) approximation [9] to deal with the core (DNP). The ultrasoft pseudopotentials [39] represented in reciprocal space were used for all elements in the calculations. Optical Bloch equation (OBE) calculations were used to set the van der Waals interactions into calculations. A Fermi smearing of 0.005 hartree (1 hartree = 27.2114 eV) was adopted. The tolerances of energy, gradient, and displacement convergence were 1.0×10^{-5} hartree. The energy calculations were carried out with spin polarization.

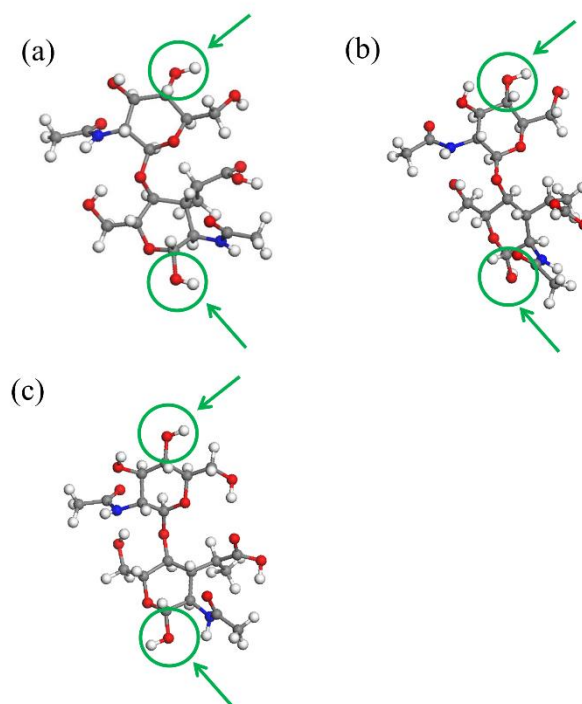


Figure 3.2 Simulation models of a part of glycan chain for first-principle tensile tests, (a) glycan chain interacting with no Au, (b) glycan chain interacting with nanoporous Au (NPG) (+5% strain) and (c) glycan chain interacting with NPG (-5% strain). The part of glycan chain corresponds to the one shown by an arrow (a) in Fig. 3.1. Gray, red, blue and white spheres show carbon, oxygen, nitrogen and hydrogen atoms, respectively.

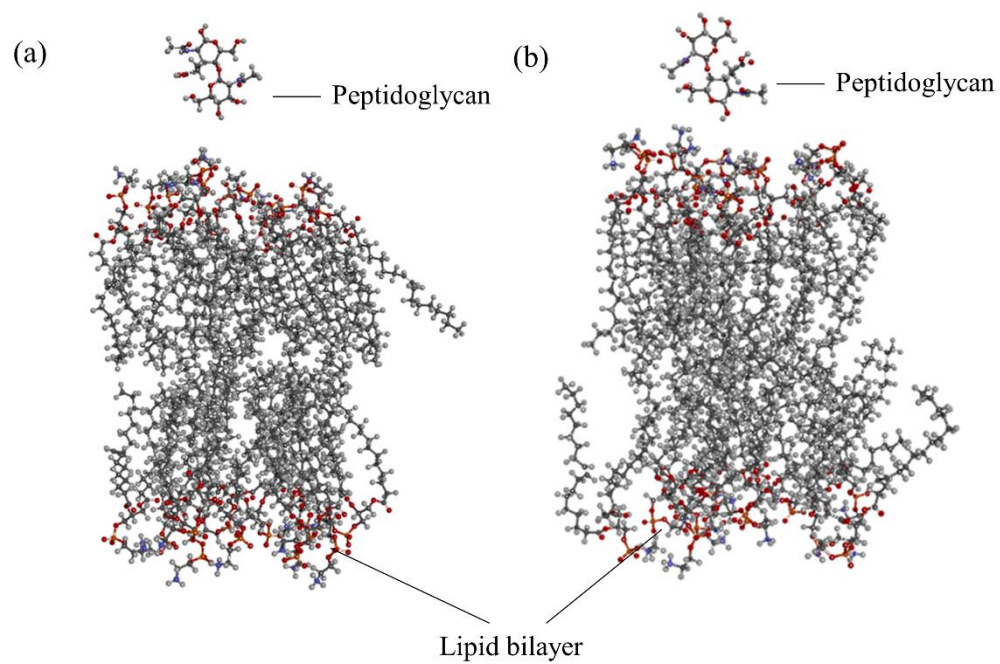


Figure 3.3 Lipid bilayer models interacting with peptidoglycan located on (a) flat Au and (b) nanoporous Au (-5% strain). No critical damage is found in lipid bilayer interacting with the peptidoglycan located on nanoporous Au.

The 24 POPE lipid were solvated in 1,412 water molecules using CHARMM-GUI web site. A part of peptidoglycan interacting with FG or NPG was positioned on lipid membrane (Fig. 3.3). Periodic boundary conditions were applied. MD simulations were performed using the CHARMM force field [35] with gromacs 5.1.1 code [43,44]. The position of peptidoglycan was fixed during the simulations. The system was energy-minimized using the steepest decent algorithm (500,000 steps). MD simulations were performed with the time step of 1.0 fs. The system was equilibrated for 10 ns to obtain a stable structure of peptidoglycan with the constant number of particles, volume and temperature (NVT) ensemble. Finally, the 100 ns NVT simulations were performed.

Initial coordinates for potassium channel were taken from the crystal structures 1K4C. The channel was embedded in a bilayer of 2,182 POPE lipid and solvated in 15,078 water molecules and 15 Cl⁻ ions using CHARMM-GUI web site. A part of peptidoglycan interacting with FG or NPG was positioned on the ion channel (Fig. 3.4). Periodic boundary conditions were applied. MD simulations were performed using the CHARMM force field³⁵ with gromacs 5.1.1 code [43,44]. The position of peptidoglycan was fixed during the simulations. The system was energy-minimized using the steepest decent

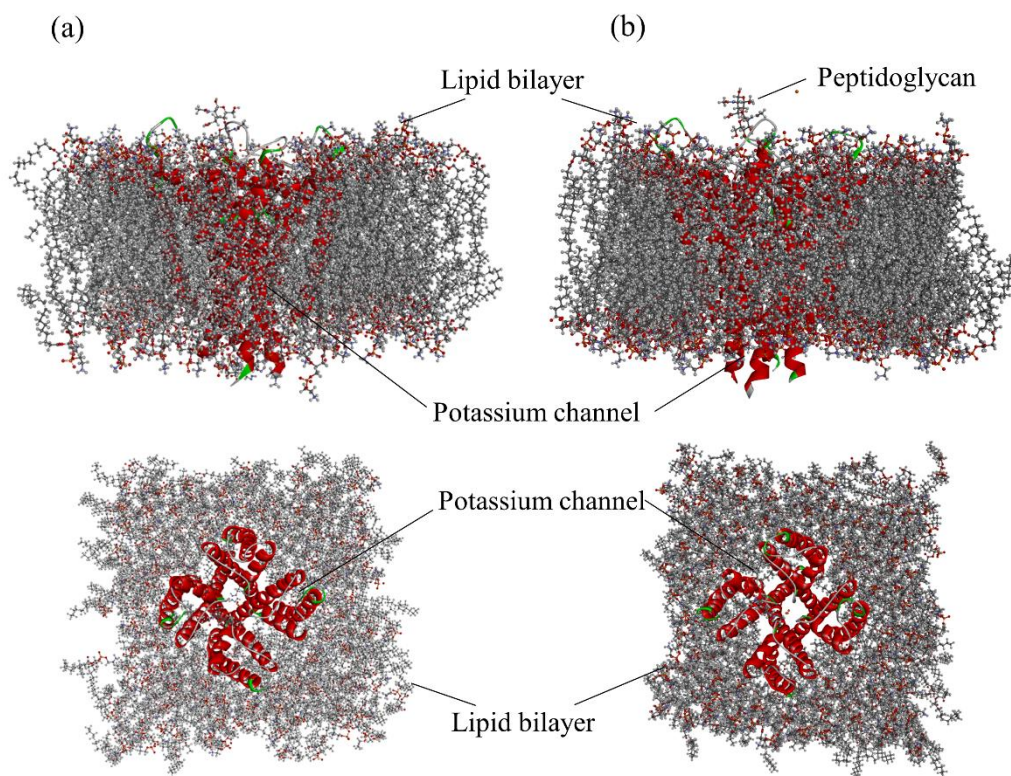


Figure 3.4 Schematic illustrations from side view (upper panel) and top view (lower panel) of potassium ion channel interacting with peptidoglycan located on (a) flat Au and (b) nanoporous Au (-5% strain). The whole structure of potassium channel is not affected by peptidoglycan located on nanoporous Au (-5% strain).

algorithm (500,000steps). MD simulations were performed with the time step of 1.0 fs. The system was equilibrated for 10 ns to obtain a stable structure of peptidoglycan with the constant number of particles, volume and temperature (NVT) ensemble. Finally, the 100 ns NVT simulations were performed.

3.2.2 Experimental methods

Au (>99.9 mass%) was sputtered on a glass slide (50 mm square and 1.2 mm in thickness) by radio-frequency (RF) magnetron sputtering (SVC-700RF, Sanyu Electron Co., Ltd., Tokyo, Japan). The Au layer was 90 nm in thickness, which is necessary to avoid delamination and fragmentation of NPG during dealloying because of its brittleness and shrinkage^{23,25}. Then, a Au_{0.3}Ag_{0.7} alloy with a thickness of 80 nm was sputtered on the Au thin film on the glass slide by RF magnetron sputtering. NPG was synthesized by dealloying of the Au-Ag/Au/glass slide (free corrosion) at 253 K for 24 h in 69 mass% HNO₃, followed by thorough water washing. The surface structure of the fabricated NPG was observed by a scanning electron microscope (SEM, SU-6600, Hitachi High-Technologies). The quantitative chemical compositions of the samples were analyzed by energy-dispersive x-ray spectroscopy (EDXS) equipped with the SEM. For comparison, Au (90 nm in thickness) on a glass slide was also prepared by RF magnetron sputtering

as a bulk material without a nanoporous structure, and is referred to as FG. The SEM images and EDXS results are summarized in a previous publication.

Type strains of *E. coli* (K-12, NBRC 3301) were obtained from the National Institute of Technology and Evaluation (Tokyo, Japan). We incubated the bacteria in Luria–Bertani (LB) medium at 308 K for 48 h before the following experiments. Casein-peptone glucose yeast extract agar (Wako Pure Chemical Industries Ltd., Osaka, Japan) was used for the incubation.

A 400 μL of culturing suspension (1/500 nutrient broth in 100 mmol/L KCl) containing 0.4 $\mu\text{mol/L}$ of DiSC₃(5) (Tokyo Chemical Industry Corporation) and 1×10^7 colony forming unit (CFU)/mL of *E. coli* was dropped onto the nanoporous and FG substrates. The *E. coli* on nanoporous and FG substrates was cultured at 308 K for 48 h at RH = 50%. The fluorescence at wavelengths of 649–670 nm was observed at given incubation times using a fluorescent optical microscope (BX53, Olympus, Tokyo, Japan).

One quantity of platinum ear of bacteria incubated was put into 5 mL of 1/500 nutrient broth, followed by vortex mixing. 400 μL of bacterial suspension were dripped onto the samples, and the bacterial suspensions were then covered with polyethylene film. The bacterial suspensions were incubated on the samples for a given period (up to 24 h) in

humidity-controlled incubators at 35°C. The incubated bacteria were completely recovered on the samples by 5 mL of phosphate-buffered saline. We used these suspensions for the following measurements.

To immobilize the bacterial cells on the glass substrate, cover glasses were coated with poly-L-lysine (Cultrex) [45,46]. The cover glasses were covered with 150 mL of 0.02 mass% poly-L-lysine aqueous solution for 30 min and rinsed with water. The cover glasses were then air-dried for 2 h. A 200 μL of the bacterial suspension was deposited onto a cover glass coated with poly-L-lysine. After 20 min, the bacterium-coated glass substrate was then gently rinsed with water three times to remove excess and loosely attached bacterial cells. The cover glass with immobilized bacteria was then transferred into the SPM fluid cell for imaging and force-measurements in water.

SPM measurements were performed using an SPM-9700 (Shimadzu) on the above-mentioned bacterial cells immobilized on glass substrates coated with poly-L-lysine and placed in the SPM fluid cell. Silicon nitride cantilevers with a nominal spring constant of 0.15 N m^{-1} were purchased from Olympus (OMCL-TR800PSA-1). To obtain force curves, we used force-mapping in contact mode, where the tip of the cantilever was indented at 50 nm s^{-1} above the center of *E. coli*. The elastic modulus was then calculated using

Johnson–Kendall–Roberts (JKR) theory [47,48]. The indentation was conducted at least 35 times.

3.3 Results and Discussion

Figure 3.5 shows fluorescent microscopic observations for *E. coli* cultured on NPG and on FG substrates. For *E. coli* cultured on FG, only weak fluorescence was emitted during the incubation times of 0-24 h, but the emission became markedly more intense after incubation for 48 h. For *E. coli* cultured on NPG, the fluorescence behavior during the incubation times of 0-24 h was almost the same as that on FG. However, no fluorescence was observed after incubation for 48 h, unlike for *E. coli* on FG. The fluorescent experiments were conducted 5 times and the same results were obtained each time.

DiSC₃(5) [49] was used as the fluorescent probe in the fluorescent experiments. Dimeric DiSC₃(5), which does not emit fluorescence, tends to be bound to negatively-polarized matters such as cell membrane with the resting membrane potential, and dimeric DiSC₃(5) decomposes into monomeric ones without polarized matters and monomeric

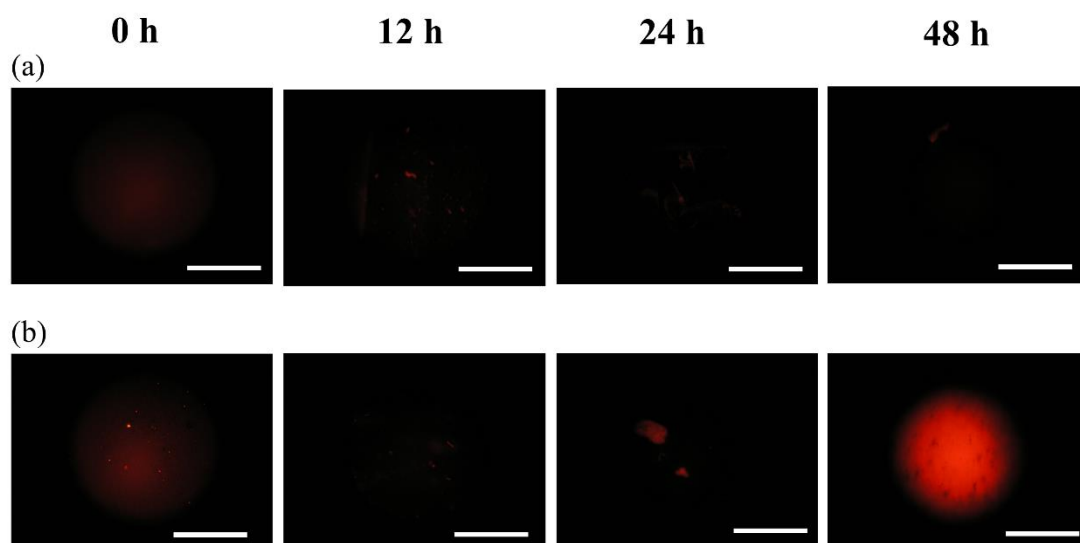


Figure 3.5 Fluorescent microscopic images of (a) *E. coli* cultured on nanoporous Au (NPG) and (b) *E. coli* cultured on flat Au (FG), where *E. coli* was cultured with a DiSC₃(5) fluorescent probe. Scale bar = 200 μm . For *E. coli* on FG, only weak fluorescence is emitted during the incubation times of 0-24 h, but this emission becomes markedly more intense after 48 h of incubation. However, for *E. coli* on NPG, no fluorescence is observed after 48 h of incubation time. The fluorescent experiments were conducted 5 times and the same results were obtained each time.

DiSC₃(5) emit fluorescence [49]. Hence, no fluorescence is emitted when the cell membrane has a certain membrane potential, while fluorescence is observed when this membrane potential is lost. The results in Fig. 3.5 show that *E. coli* was alive on FG for the first 24 h of incubation, which agrees with a previous experimental study of the viable bacterial count²⁴; however, the membrane potential was lost, accompanied by the death of *E. coli*, after incubation for 48 h. The visual observation showed that the extinction of *E. coli* at 48 h was attributed to drying of the culture medium [24]. In the case of *E. coli* on NPG, it is noteworthy that no fluorescence was found even after 48-h incubation, despite the death of *E. coli*. This suggests that a certain part of each *E. coli* cell was hyperpolarized by NPG, and dimeric DiSC₃(5) remained bound to the hyperpolarized part. The hyperpolarization must be kept after *E. coli* was dead.

When *E. coli* is attached to NPG surface, the contact site is the cell wall. The cell wall is composed of a network of peptidoglycan. Hence, peptidoglycan is a promising candidate for the material that undergoes hyperpolarization in *E. coli*. To verify this hypothesis, the interactions of peptidoglycan with NPG were investigated by a combination of MD simulations and first-principles calculations. Figure 3.6 shows the electrostatic potentials of the glycan chain (a part of a peptidoglycan) located close to a

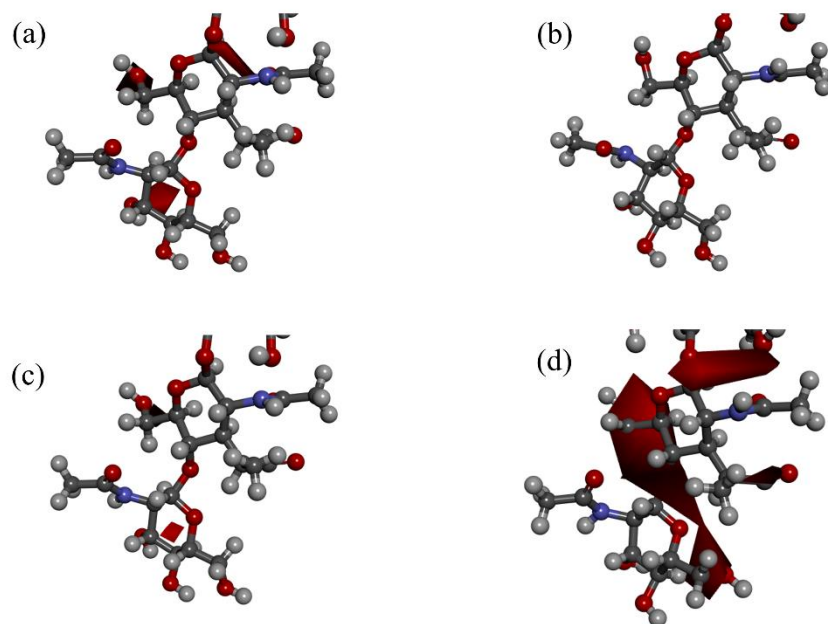


Figure 3.6 Electrostatic potentials of a part of peptidoglycan (glycan chain) close to the cell membrane, interacting with (a) no Au, (b) flat Au (FG), (c) nanoporous Au (NPG) (+5% strain) and (d) NPG (-5% strain), where the isosurface is plotted as the negative value of -20 kT. Only slight negative hyperpolarization is observed for peptidoglycan interacting with no Au, FG or NPG (+5% strain). However, large negative hyperpolarization is found for peptidoglycan interacting with NPG (-5% strain).

cell membrane, interacting with no Au substrates, FG (0% strain) or NPG (+5% and -5% strain). The isosurface is plotted as the negative value of -20 kT. Peptidoglycan interacting with NPG (-5% strain) showed a larger negative electrostatic potential than the non-interacting peptidoglycan, while no such difference was observed for peptidoglycans interacting with either FG or NPG (+5% strain). Clearly, the surface of peptidoglycan was negatively hyperpolarized by NPG. The area surrounding the surface of NPG showed a negative electrostatic potential under -5% strain, while this was not observed for the FG surface (Fig. 3.7). The vicinity of a metallic surface is generally characterized by an electric double layer, caused by the seeping of valence electrons out of the surface [50], making the surface positively charged and the surrounding negatively charged. Here, the magnitude of the electric double layer was enhanced for NPG under -5% strain, as shown in Fig. 3.7. Therefore, the negative hyperpolarization of peptidoglycan can probably be attributed to the enhanced positive charge at the NPG surface.

In the previous study [24], bacteria killed by NPG were found to leak the cytoplasm. If the elastic modulus of peptidoglycan is weakened by the hyperpolarization induced by NPG and the weakened peptidoglycan cannot stand the turgor pressure of a cell, the

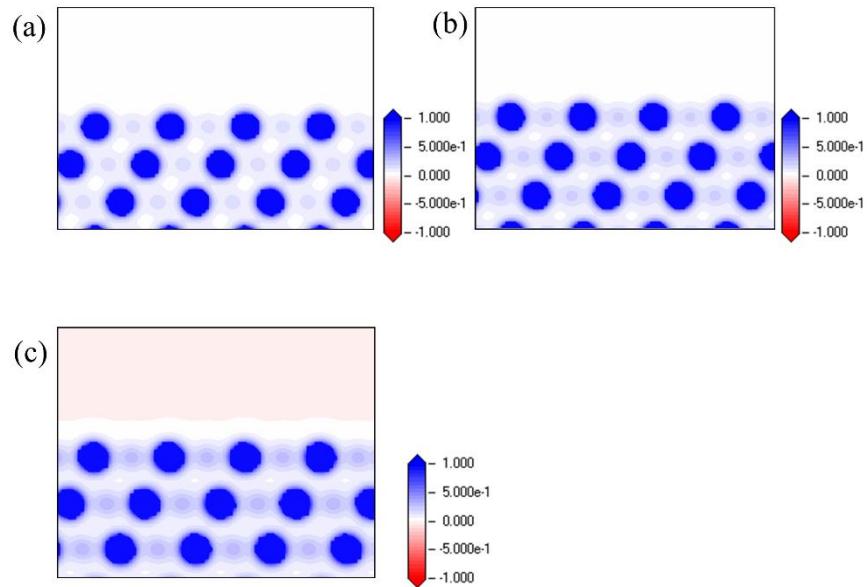


Figure 3.7 Electrostatic potential for (a) flat Au (FG), (b) nanoporous Au (NPG) (+5% strain) and (c) NPG (-5% strain). The electrostatic potential is negative at a region outside the surface of NPG (-5% strain), comparing with FG, indicating that the negative strain enhances the positive charge at the surface of NPG.

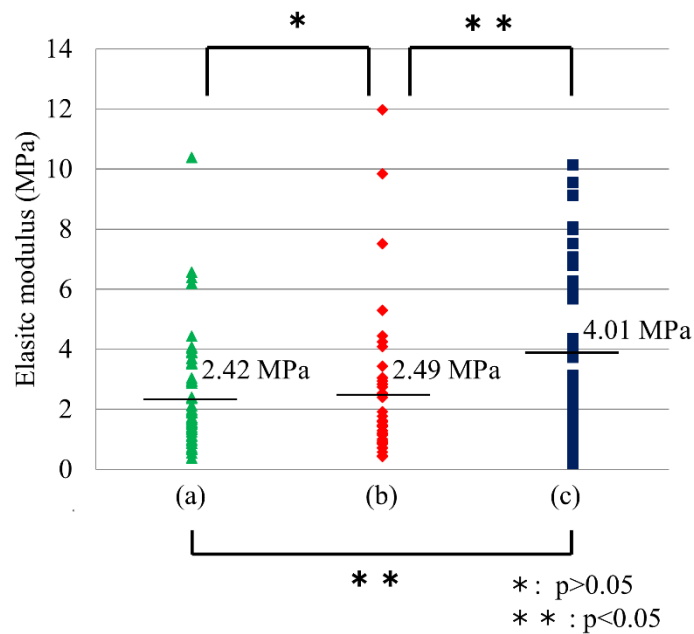


Figure 3.8 The elastic modulus of the cell wall, measured by scanning probe microscopy, of (a) raw *E. coli* (not cultured on a Au substrate), (b) *E. coli* cultured on flat Au (FG) and (c) *E. coli* cultured on nanoporous Au (NPG), where the bars show the average values. According to the *t*-test, there is no significant difference in elastic modulus between raw *E. coli* and *E. coli* cultured on FG; however, the elastic modulus of *E. coli* cultured on NPG is larger than the others.

leakage of cytoplasm will occur. To verify this, the elastic modulus was investigated by the SPM measurements. Figure 3.8 shows the elastic moduli of raw *E. coli* (not cultured on a Au substrate), *E. coli* cultured on FG and *E. coli* cultured on NPG. The average elastic modulus was 2.42 MPa for raw *E. coli*, 2.49 MPa for *E. coli* cultured on FG and 4.01 MPa for *E. coli* cultured on NPG. Previous measurements of the elastic moduli of organisms such as *E. coli* have ranged from 0.01 to 800 MPa [51], depending on measurement methods and conditions. The values obtained in the present investigation thus fall within this range. According to the *t*-test, there is no difference in elastic modulus between raw *E. coli* and *E. coli* incubated on FG; however, the elastic modulus of *E. coli* incubated on NPG is larger than the others. Thus, the interaction with NPG clearly strengthened the cell wall of *E. coli*. Previous studies also reported an increase in rigidity for malaria-infected red blood cells [52-54].

The increased elastic modulus of the cell wall of *E. coli* cultured on NPG was related to the hyperpolarization of peptidoglycan. Here, first-principles calculations were carried out to investigate in detail the effects of the hyperpolarization on the elastic modulus. The number of atoms that can be investigated by first-principles calculations is limited. Here,

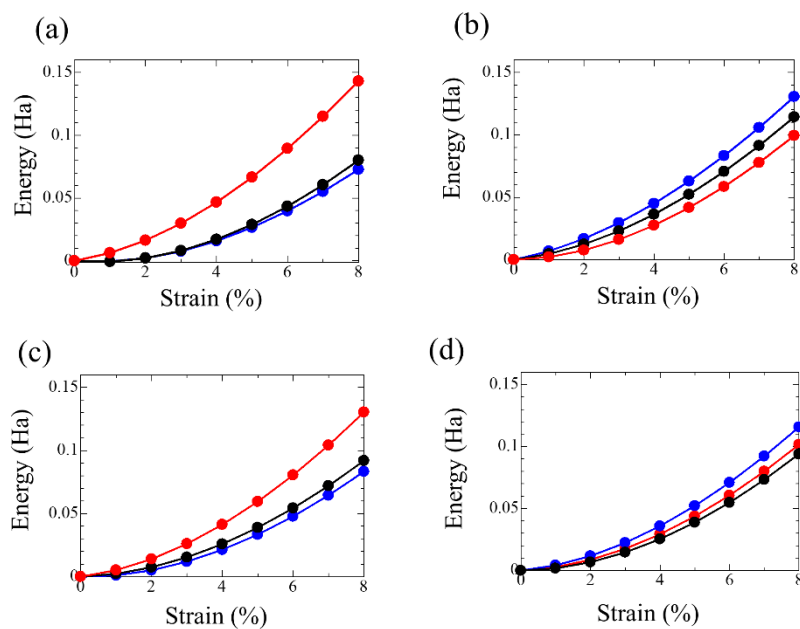


Figure 3.9 Energy–strain curves calculated by first-principles tensile tests for four parts of a glycan chain, where a-d correspond to the four parts (a)-(d) of a glycan chain shown in figure 3.1. Blue, red and green lines show results of glycan chain interacting with no Au, flat Au (FG) or nanoporous Au (NPG) (-5% strain), respectively. The interaction energy of the glycan chain with NPG is greater than those with no Au and with FG in all four parts.

four parts of the glycan chain, shown by arrows in Fig. 3.1, were investigated by the first-principles tensile tests. The energy–strain curves for the four parts of the glycan chain are shown in Fig. 3.9. For *E. coli* on NPG, the energy as a function of the strain was higher than for raw *E. coli* and for *E. coli* cultured on FG in all four parts. This indicates that the elastic modulus of the peptidoglycan was increased by the interactions with NPG, which agrees with the experimental SPM measurements.

The relative locations of atoms of peptidoglycan were not changed by NPG (Fig. 3.2), however, the interatomic distances in peptidoglycan were changed by NPG. For example, the distance between two oxygen atoms in one part of the molecule, shown by arrows in Fig. 3.2, was 10.048 Å for raw *E. coli*, 10.526 Å for *E. coli* cultured on FG and 10.847 Å for *E. coli* cultured on NPG. The lengthening of the O–O distance for *E. coli* cultured on NPG is related to the negative hyperpolarization induced by NPG. Thus, both the experimental and simulation results showed that the cell wall was strengthened by NPG, contrary to expectation. Therefore, the antimicrobial activity of NPG is unlikely to be a result of the weakening of the cell wall. The leakage of cytoplasm was observed for *E. coli* on NPG in the previous work [24], suggesting that the leakage of cytoplasm occurred after the bacteria died. Recently, it was found that nanoprotusions, whose height was

about 500 nm, on the surface led to the mechanical rupture of bacteria [20,21]. In this case, the penetration of nanoprotusions to 200 nm in depth inside bacteria was needed for causing the mechanical rupture of bacteria [20]. However, the pore or ligament size in NPG is about 20 nm, and therefore the mechanical rupture of bacteria cannot be caused by NPG.

Transcriptomic analyses [24] have revealed that NPG disturbs the function of the cell membrane, suggesting that the hyperpolarization of the cell wall affects the structure or function of the cell membrane. One of main components of a cell membrane is the lipid bilayer. Hence, the interactions of the lipid bilayer with hyperpolarized peptidoglycan were investigated by MD simulations. The results showed that the lipid bilayer interacting with the hyperpolarized peptidoglycan did not undergo critical damage, relative to the lipid bilayer interacting with the non-hyperpolarized peptidoglycan (Fig. 3.3). Positively charged Au nanoparticles are known to cause critical damage to the cell membrane of bacteria [17,18], which has also been verified by MD simulations [55,56]. In the present investigations, however, the cell wall was negatively charged, not positively, and the magnitude of this charge was much smaller than that of the positively charged Au nanoparticles. Thus, the hyperpolarized cell wall did not disrupt the lipid bilayer.

The cell membrane consists not only of the lipid bilayer, but also of a variety of membrane proteins. Disruption of the lipid bilayer is not necessarily required for bacterial death. For example, Au nanoparticles killed bacteria by inhibiting the activity of ATPase¹¹. In the present work, the potassium channel was investigated because it plays a critical role in maintaining the ion concentration inside a cell, which controls a wide variety of cell functions. Hence, in this work, the interactions of the potassium channel with the hyperpolarized peptidoglycan were investigated by MD simulations. The results showed that the overall structure of the potassium channel was only slightly affected by the hyperpolarized peptidoglycan (Fig. 3.4), as in the case of the lipid bilayer. However, the hyperpolarized peptidoglycan did cause delicate differences in the atomic positions of the ion channel. Potassium ions pass through this channel 10,000 times faster than sodium ions, despite the close similarity in size of the two species. The high selectivity of the potassium channel is related to the sophisticated structure of the selectivity filter, which forms the most constricted part of the conduction pathway. If the structure of the selectivity filter is changed even just a little bit, a critical damage will be given to the functions of the ion channel. Figure 3.10 shows the variation in root-mean-square-fluctuation (RMSF) of the atomic positions of the amino acids (Gly77, Tyr78 and Gly79)

constituting the exit region of the selectivity filter, where the horizontal axis indicates the atoms in these amino acids and the atom numbering is shown in Table 3.1. The RMSF is given by

$$\text{RMSF} = \sqrt{\frac{1}{t} \sum (x_i(t_j) - x_i)^2} \quad (3.1)$$

where t_j is the simulation time, $x_i(t_j)$ is the position of atom i at simulation time t_j , and x_i is the time-averaged position of atom i . The average RMSF was 0.68 Å for the selectivity filter interacting with the hyperpolarized peptidoglycan and 0.85 Å for the non-interacting selectivity filter, indicating that the structure of the selectivity filter fluctuated less in the presence of NPG. This difference of the average RMSF values has serious implications for the viability of the cells, being as large as the difference between a sodium ion (=1.02 Å) and a potassium ion (=1.38 Å). Any structural change to the selectivity filter strongly

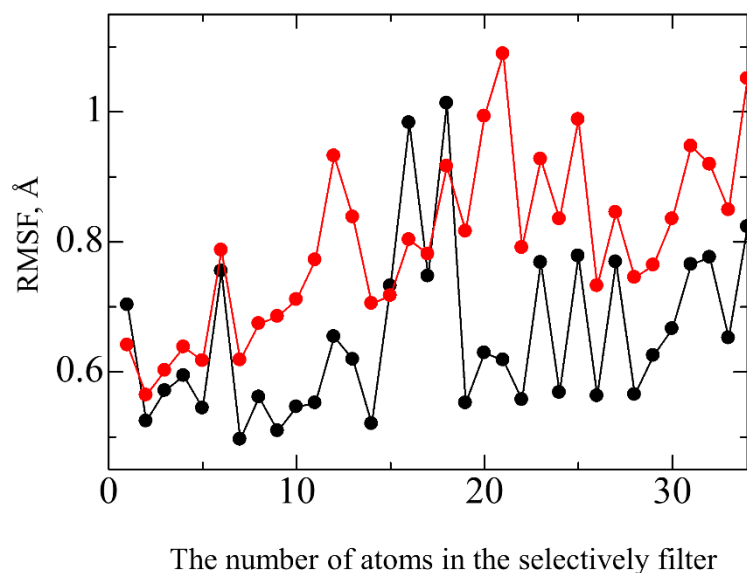
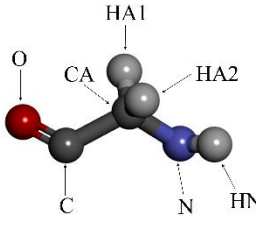
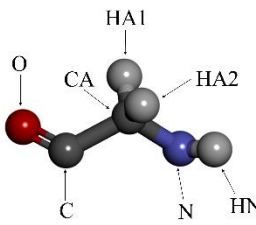


Figure 3.10 Variation in root-mean-square-fluctuation (RMSF) of atomic positions of the amino acids (Gly77, Tyr78 and Gly79) constituting the exit region of the selectivity filter, where the horizontal axis indicates the atoms in the amino acids and the atom numbering is shown in table 3.1. Black and red lines show the RMSF value of the selectivity filter interacting with no Au and nanoporous Au (NPG), respectively. The RMSF values for the selectivity filter interacting with the hyperpolarized peptidoglycan are lower than those for the non-interacting selectivity filter, indicating that the structure of the selectivity filter fluctuates less in the presence of NPG.

Table 3.1 The number of atoms in Gly77, Tyr78 and Gly79. The schematic illustrations of amino acids and the descriptions of kind of atoms are shown in the right column, where gray, red, blue and white spheres show carbon, oxygen, nitrogen and hydrogen atoms, respectively.

Number	Atom	Amino acid
1	N	Gly77 
2	HN	
3	CA	
4	HA1	
5	HA2	
6	C	
7	O	
8	N	Tyr78
9	HN	
10	CA	
11	HA	

12	CB	
13	HB1	
14	HB2	
15	CG	
16	CD1	
17	HD1	
18	CE1	
19	HE1	
20	CZ	
21	OH	
22	HH	
23	CD2	
24	HD2	
25	CE2	
26	HE2	
27	C	
28	O	

29	N	<p>Gly79</p> 
30	HN	
31	CA	
32	HA1	
33	HA2	
34	C	
35	O	

affects the velocity of potassium ions through the ion channel. Hence, any change in the structural fluctuation of the selectivity filter will affect the ion concentration inside a cell, and in turn a wide variety of cellular functions, irrespective of whether the velocity of potassium ions is increased or decreased by the reduction in fluctuation. A long incubation time of 24 h was needed for the antimicrobial activity of NPG [24]. This is quite different from the antimicrobial activity of metallic ions, which kill bacteria immediately after commencing incubation. Metallic ions immediately destroy the cell membrane. In contrast, the hyperpolarized peptidoglycan did not destroy or even damage the cell membrane, but rather caused delicate changes to the structure of the ion channel. Therefore, a longer time was needed for the bactericidal activity of NPG to be exerted.

3.4 Conclusions

In conclusion, the fluorescent microscopic observation, the SPM measurements, and the cooperation of MD simulations and first principle calculations were performed to investigate the antimicrobial mechanisms of NPG. The cell wall of *E. coli* was strengthened by NPG, indicating that the antimicrobial activity of NPG is not a result of

the weakening of the cell wall. The cell wall of bacteria was negatively hyperpolarized by NPG, and the hyperpolarized cell wall caused delicate changes to the structure of the ion channel. Therefore, it is suggested that the hyperpolarization induced by NPG played a critical role in its antimicrobial activity.

References

- [1] Y. Li, D. Shuai, S. Naraginti, D. Wang & W. Zhang, “Visible-Light-Driven Photocatalytic Inactivation of MS2 by Metal-Free g-C₃N₄: Virucidal Performance and Mechanism.”, *Water Research* **106**, (2016) 249-258.
- [2] A. K. Chatterjee, R. Chakraborty & T. Basu, “Mechanism of Antimicrobial Activity of Copper Nanoparticles”, *Nanotechnology* **25**, (2014) 135101-135707.
- [3] L. Z. Zhao, H. R. Wang, K. F. Huo, L. Y. Cui, W. R. Zhang, H. W. Ni, Y. M. Zhang, Z. F. Wu and C. K. Paul, “Antibacterial Nano-Structured Titania Coating Incorporated with Silver Nanoparticles”, *Biomaterials* **32**, (2011) 5706–5716.
- [4] O. Choi and Z. Hu, “Size dependent and reactive oxygen species related nanosilver toxicity to nitrifying bacteria”, *Environ. Sci. Technol.* **42**, (2008) 4583–4588.
- [5] C. Beer, R. Foldbjerg, Y. Hayashi, D. S. Sutherland and H. Autrup, “Toxicity of Silver Nanoparticles–Nanoparticle or Silver Ion?”, *Toxicol. Lett.* **208**, (2012) 286–292.
- [6] E. Navarro, F. Piccapietra, B. Wagner, F. Marconi, R. Kaegi, N. Odzak, L. Sigg and R. Behra, “Toxicity of Silver Nanoparticles to *Chlamydomonas Reinhardtii*” *Environ. Sci. Technol.* **42**, (2008) 8959–8964.

- [7] K. R. Raghupathi, R. T. Koodali and A. C. Manna, “Size-Dependent Bacterial Growth Inhibition and Mechanism of Antibacterial Activity of Zinc Oxide Nanoparticles” *Langmuir* **27**, 4020–4028 (2011).
- [8] G. Zhao and S. E. Stevens Jr, “Multiple Parameters for the Comprehensive Evaluation of the Susceptibility of *Escherichia Coli* to the Silver Ion” *Biometals* **11**, (1998) 27-32.
- [9] B. Galeano, E. Korff and W. L. Nicholson, “Inactivation of Vegetative Cells, but not Spores, of *Bacillus anthracis*, *B. cereus*, and *B. subtilis* on Stainless Steel Surfaces Coated with an Antimicrobial Silver- and Zinc-Containing Zeolite Formulation” *Appl. Environ. Microbiol.* **69**, (2003) 4329-4331.
- [10] S. Sadhasivam, P. Shanmugam, M. Veerapandian, R. Subbiah and K. Yun, “Biogenic Synthesis of Multidimensional Gold Nanoparticles Assisted by *Streptomyces hygroscopicus* and its Electrochemical and Antibacterial Properties”, *Biometals* **25**, (2012) 351-360.
- [11] Y. Cui, Y. Zhao, Y. Tian, W. Zhang, X. Lu and X. Jiang, “The Molecular Mechanism of Action of Bactericidal Gold Nanoparticles on *Escherichia coli*.”, *Biomaterials* **33**, (2012) 2327-2333.

- [12] Y. Zhang, H. Peng, W. Huang, Y. Zhou and D. Yan, “Facile Preparation and Characterization of Highly Antimicrobial Colloid Ag or Au Nanoparticles”, *J. Colloid Interface Sci.* **325**, (2008) 371-376.
- [13] J. F. Hernandez-Sierra, F. Ruiz, D. C. C. Pena, F. Martinez-Gutierrez, A. E. Martinez, A. de J. P. Guillen, H. Tapia-Perez, and G. M. Castanon, “The Antimicrobial Sensitivity of *Streptococcus mutans* to Nanoparticles of Silver, Zinc Oxide, and Gold”, *Nanomed.-Nanotechnol. Biol. Med.* **4**, (2008) 237-240.
- [14] J. J. Li, D. Hartono, C. -N. Ong, B. -H. Bay and L. -Y. L. Yung, “Autophagy and Oxidative Stress Associated with Gold Nanoparticles”, *Biomaterials* **31**, (2010) 5996-6003.
- [15] F. U. Khan et al., “Visible Light Inactivation of *E. coli*, Cytotoxicity and ROS Determination of Biochemically Capped Gold Nanoparticles”, *Microbial Pathogenesis* **107**, (2017) 419-424.
- [16] A. Kumar, S. Kumar, W. -K. Rhim, G. -H. Kim, J. -M. Nam, “Oxidative Nanopeeling Chemistry-Based Synthesis and Photodynamic and Photothermal Therapeutic Applications of Plasmonic Core-Petal Nanostructures”, *J. Am. Chem. Soc.* **136**, (2014) 16317-16325.

- [17] L. Mei, Y. Wang, W. Zhang, Z. Lu, Y. Luo, Y. Zhao and C. Li, “Multivalent Polymer-Au Nanocomposites with Cationic Surfaces Displaying Enhanced Antimicrobial Activity”, *Polymer Chemistry* **5**, (2014) 3038-3044.
- [18] Z. V. Feng *et al.*, “Impacts of Gold Nanoparticle Charge and Ligand Type on Surface Binding and Toxicity to Gram-Negative and Gram-Positive Bacteria”, *Chemical Science* **6**, (2015) 5186-5196.
- [19] L. Rizzello *et al.*, “Impact of Nanoscale Topography on Genomics and Proteomics of Adherent Bacteria”, *ACS Nano* **5**, (2011) 1865-1876.
- [20] E. P. Ivanoa *et al.*, “Natural Bactericidal Surfaces: Mechanical Rupture of *Pseudomonas Aeruginosa* Cells by Cicada Wings”, *Small* **16**, (2012) 2489-2494.
- [21] E. P. Ivanoa *et al.*, “Bactericidal Activity of Black Silicon”, *Nature Communications* **4**, (2013) 2838-2844.
- [22] K. Anselme, P. Davidson, A. M. Popa, M. Giazzon, M. Liley and L. Ploux, “The Interaction of Cells and Bacteria with Surfaces at the Nanometer Scale”, *Acta Biomaterialia* **6**, (2010) 3824-3846.
- [23] J. Erlebacher, M. J. Aziz, A. Karma, N. Dimitrov and K. Sieradzki, “Evolution of Nanoporosity in Dealloying”, *Nature* **410**, (2001) 450-453.

- [24] M. Hakamada, S. Taniguchi and M. Mabuchi, “Antimicrobial Activity of Nanoporous Gold Against *Escherichia coli* and *Staphylococcus epidermidis*.”, *J. Mater. Res.* **32**, (2017) 1787-1795.
- [25] S. Parida, D. Kramer, C. A. Volkert, H. Rosner, J. Erlebacher and J. Weissmuller, “Volume Change during the Formation of Nanoporous Gold by Dealloying”, *Phys. Rev. Lett.* **97**, (2006) 035504.
- [26] M. Hakamada, H. Nakano, T. Furukawa, M. Takahashi and M. Mabuchi, “Hydrogen Storage Properties of Nanoporous Palladium Fabricated by Dealloying”, *J. Phys. Chem. C* **114**, (2010) 868-873.
- [27] M. Hakamada, T. Furukawa, T. Yamamoto, M. Takahashi, & M. Mabuchi, “Abnormal Hydrogen Absorption/Desorption Properties of Nanoporous Pt with Large Lattice Strains”, *Mater. Trans.* **52**, (2011) 806-809.
- [28] M. Hakamada, M. Yuasa and M. Mabuchi, “Anomalous Mechanical Characteristics of Au/Cu Nanocomposite Processed by Cu Electroplating”, *Phil. Mag.* **95**, (2015) 1499-1510.

- [29] H. Heintz, R. A. Vaia, B. L. Farmer and R. R. Naik, “Accurate Simulation of Surfaces and Interfaces of Face-Centered Cubic Metals Using 12-6 and 9-6 Lennard-Jones Potentials”, *J. Phys. Chem. C*, **112** (2008) 17281-17290.
- [30] J. Dubochet, A. W. McDowell, B. Menge, E. N. Schmid and K. G. Lickfeld, “Electron Microscopy of Frozen-Hydrated Bacteria”, *J. Bacteriol.* **155**, (1983) 381-390.
- [31] S. O. Meroueh, K. Z. Bencze, D. Heseck, M. Lee, J. F. Fisher, T. L. Stemmler and S. Mobashery, “Three-Dimensional Structure of the Bacterial Cell Wall Peptidoglycan”, *PNAS* **103**, (2006) 4404-4409.
- [32] B. Dmitriev, F. Toukach and S. Ehlers, “Towards a Comprehensive View of the Bacterial Cell Wall”, *Trends in Microbiol.* **13**, (2015) 569-574.
- [33] M. Yusupov, A. Bogaerts, S. Huygh, R. Snoeckx, A. C. T. van Duin, & N. C. Erik, “Plasma-Induced Destruction of Bacterial Cell Wall Components: A Reactive Molecular Dynamics Simulation”, *J. Phys. Chem. C* **117**, (2013) 5993-5998.
- [34] J. M. Ghuyssen, “Use of Bacteriolytic Enzymes in Determination of Wall Structure and Their Role in Cell Metabolism”, *Bacteriological reviews* **32**, (1968) 425-464.
- [35] A. D. MacKerell Jr. et al., “All-Atom Empirical Potential for Molecular Modeling and Dynamics Studies of Proteins”, *J. Phys. Chem. B* **102**, (1998) 3586-3616.

- [36] B. J. Delley, “An All-Electron Numerical Method for Solving the Local Density Functional for Polyatomic Molecules”, *J. Chem. Phys.* **92**, (1990) 508-517.
- [37] B. J. Delley, “From Molecules to Solids with the Dmol³ Approach”, *J. Chem. Phys.* **113**, (2000) 7756-7764.
- [38] J. P. Perdew et al., “Atoms, Molecules, Solids, and Surfaces: Application of the Generalized Approximation for Exchange and Correlation”, *Phys. Rev. B* **46**, (1992) 6671-6687.
- [39] D. Vanderbilt, “Soft Self-Consistent Pseudopotentials in a Generalized Eigenvalue Formalism”, *Phys. Rev. B* **14**, (1990) 7892-7895.
- [40] H. J. Monkhorst and J. D. Pack, “Special Points for Brillouin-Zone Integrations”. *Phys. Rev. B* **13**, (1976) 5188-5192.
- [41] W. Rocchia, E. Alexov, and B. Honig, “Extending the Applicability of the Nonlinear Poisson-Boltzmann Equation: Multiple Dielectric Constants and Multivalent Ions”, *J. Phys. Chem. B* **105**, (2001) 6507-6514.
- [42] W. Rocchia, S. Sridharan, A. Nicholls, E. Alexov, A. Chiabrera and B. Honig, “Rapid Grid-Based Construction of the Molecular Surface and the Use of Induced Surface

Charge to Calculate Reaction Field Energies: Applications to the Molecular Systems and Geometric Objects. *J. Comput. Chem.* **23**, (2012) 128-137.

[43] D. V. D. Spoel, E. Lindahl, B. Hess, G. Groenhof, A. E. Mark and H. J. C. Berendsen, “GROMACS: Fast, Flexible, and Free”, *J. Comput. Chem.* **26**, (2005) 1701-1718.

[44] M. J. Abraham, T. Murtola, R. Schulz, S. Pall, J. C. Smith, B. Hess and E. Lindahl, “GROMACS: High Performance Molecular Simulations Through Multi-Level Parallelism from Laptops to Supercomputers”, *Software X* **1-2**, (2015) 19-25.

[45] L. Shun, W. Grant, P. Richard and R. D. John, “Nanomechanical Response of Bacterial Cells to Cationic Antimicrobial Peptides” *Soft Matter* **10**, (2014) 1806-1815.

[46] A. V. Bolshakova, O. I. Kiselyova and I. V. Yaminsky, “Microbial Surfaces Investigated Using Atomic Force Microscopy”, *Biotechnol. Prog.* **20**, (2004) 1615-1622.

[47] K. L. Johnson, K. Kendall and A. D. Roberts, “Surface Energy and the Contact of Elastic Solids”, *Proc. R. Soc. London Ser. A-Math. Phys. Eng. Sci.* **324**, (1971) 301-313.

[48] S. Nagai, S. Fujinami, K. Nakajima and T. Nishi, “Recent Development of Nanomechanical Property Measurement”, *J. Soc. Rheol. Jpn.* **36**, (2008) 99-106.

[49] G. Cabrini and A. S. Verkman, “Potential-Sensitive Response Mechanism of diS-C3-(5) in Biological Membranes”, *J. Membr. Biol.* **92**, (1986) 171-182.

- [50] N. D. Lang and W. Kohn, "Theory of Metal Surfaces", *Phys. Rev. B* **1**, (1970) 4555-4568.
- [51] H. T. Hannah, K. A. George, D. R. Lars, M. Hasebe, T. Carolina, S. Max, C. C. Wendy, G. Ajay, C. H. Kerwyn & B. W. Douglas, "Measuring the Stiffness of Bacterial Cells from Growth Rates in Hydrogels of Tunable Elasticity", *Mol. Microbiol.* **84**, (2012) 874-891.
- [52] B. M. Cooke, N. Mohandas and R. L. Coppel, "The Malaria-Infected Red Blood Cell: Structural and Functional Changes", *Adv. Parasitol.* **50**, (2001) 1-86.
- [53] G. B. Nash, E. O' Brien, E. C. G. -Smith & J. A. Dormandy, "Abnormalities in the Mechanical Properties of Red Blood Cells Caused by Plasmodium Falciparum", *Blood* **74**, (1989) 855-861.
- [54] M. Paulitschke and G. B. Nash, "Membrane Rigidity of Red Blood Cells Parastized by Different Strains of Plasmodium Falciparum", *J. Lab. Clin. Med.* **122**, (1993) 581-589.
- [55] E. Heikkila *et al.*, "Cationic Au Nanoparticles Binding with Plasma Membrane-Like Lipid Bilayers: Potential Mechanism for Spontaneous Permeation to Cells Revealed by Atomistic Simulations", *J. Phys. Chem. C* **118**, (2014) 11131-11141.

[56] R. Gupta and B. Rai, “Effect of Size and Surface Charge of Gold Nanoparticles on their Skin Permeability: A Molecular Dynamics Study”, *Sci. Rep.* **7**, (2017) 1-13.

CHAPTER4

ELECTRONIC ORIGIN OF ANTIMICROBIAL ACTIVITY OWING TO SURFACE EFFECT

4.1 Introduction

The surface effect owing to peculiar electronic states at the surface is one of the most important properties of metallic nanomaterials. However, there is much room for understanding the surface effect on large organic matters such as bacteria, whereas there are many studies on small molecules such as amino acids [1,2]. Actually, the remarkable antimicrobial activity (AA) of metallic nanomaterials such as Au nanoparticles is not directly caused by the surface effect because the AA results from the emission of harmful substances such as metallic ions and reactive oxygen species (ROS) [3-5]. There are other kinds of antimicrobial metallic nanomaterials that kill bacteria through incorporation into the cytoplasm and deterioration of cytoplasmic proteins without releasing ROS and metallic ions [6-8]. Understanding of the origins of AA without the release of harmful substances is required for the safe application of antimicrobial nanomaterials.

Nanoporous Au (npAu) shows high catalytic activities on organic molecules such as the oxidation of carbon monoxide [9] and methanol [10]. The catalytic activities of npAu originate from the peculiar electronic states on their surfaces. Recently, higher AA of npAu compared with that of flat Au (fAu) was reported [11]. Again, the AA of npAu does not include the emission of harmful substances such as metallic ions and reactive oxygen

species. In addition, the npAu did not exhibit AA in a high relative humidity of 90%, indicating that the direct contact of the bacteria on the npAu surface was necessary for the high AA. NpAu specimens cannot pass through the cell wall of bacteria because of their bulky dimensions, with typical macroscopic lengths larger than one millimeter. These facts suggest that the high AA of npAu can be attributed to the surface effect. Because of the inertness of gold, organic molecules are adsorbed on Au surfaces through physisorption owing to Coulombic or van der Waals interactions and not owing to chemical (covalent/ionic) binding. Therefore, the surface effect of npAu was related to the Coulombic or van der Waals interactions between the bacterial cell wall and the npAu surface. However, the physical origins of the surface effects in npAu are still not sufficiently understood.

In chapter 3, the results showed that the cell wall of bacteria was negatively hyperpolarized after contact with the npAu surface and the hyperpolarized cell wall caused the structural change of ion channels, which led to the AA of npAu [12]. Electrons spill out on a metallic surface and an electric double layer is formed, resulting in a positive metallic surface [13,14]. Therefore, the nature of peculiar electronic states at the surface, which is responsible for the AA, is related to the spilling out of electrons. Therefore, it is worth estimating the intensity of the spilling out of electrons for deep understanding of the origin of the AA. The molecular dipole is closely connected with the work function (WF) [15,16]. Also, the interface dipole moment is generated during the adsorption of organic molecules [17,18]. Therefore, the hyperpolarization of the cell wall of bacteria, which is induced by npAu, is suggested to have a correlation with the WF of npAu. In the present work, the effectiveness of WF as an indicator of AA was demonstrated by

investigating Au specimens with different WFs. There are some methods to vary the WF of metallic surfaces: adsorption of molecules [17,19], modification of self-assembled monolayers (SAMs) [16,20], alloying [21,22] and lattice distortion [23,24]. The adsorption of molecules and SAM modification were not appropriate in the present work because the effect of the adsorbates themselves on the AA cannot be neglected. Therefore, alloying was appropriate for varying the WF of npAu. We chose platinum (Pt) as an alloying element because ion elution of Pt can be neglected owing to its nobleness (or low ionization tendency).

In the present work, the AAs of nanoporous Au-Pt (npAu-Pt_{0.5} and npAu-Pt_{0.1}, see Methods for details), npAu and fAu specimens were investigated on *E. coli*. Also, their WFs were calculated from ultraviolet photoelectron spectrometry (UPS) measurements. Furthermore, a first-principles calculation and molecular dynamics (MD) simulations were performed to analyze the electronic states of the surface and the cell wall. To the best of our *knowledge*, the present paper is the first work showing that the WF can be *representative of the surface effect on the biological phenomenon of AA*.

4.2 Methods

4.2.1 Preparation of npAu and npAu-Pt

A 100-nm-thick pure gold film (>99.9 mass%) was sputtered on a 50×50×1.2 mm glass substrate. 150-nm-thick Au_{0.3}Ag_{0.7}, (Au_{0.5}Pt_{0.5})₂₅Ag₇₅, and (Au_{0.9}Pt_{0.1})₂₅Ag₇₅ films were then sputtered on the pure gold film. Nanoporous Au and Au-Pt specimens were fabricated by dealloying (free corrosion) of these films at 253 K for 24 h in 69 mass% HNO₃. Also, a nanoporous Au specimen with a larger pore of 50 nm was fabricated by

dealloying at 298 K. Nanoporous Au and Au-Pt made of $\text{Au}_{0.3}\text{Ag}_{0.7}$, $(\text{Au}_{0.5}\text{Pt}_{0.5})_{25}\text{Ag}_{75}$ and $(\text{Au}_{0.9}\text{Pt}_{0.1})_{25}\text{Ag}_{75}$ were denominated “npAu”, “npAu-Pt_{0.5}” and “npAu-Pt_{0.1}”, respectively. Immediately after dealloying, the specimens were thoroughly rinsed more than 10 times with pure water. A flat Au (fAu) specimen, which was fabricated by sputtering of pure gold, was used as a reference inert substrate. The microstructures of npAu-Pt and npAu specimens were observed by scanning electron microscopy (SEM; SU-6600 by Hitachi High-Technologies Corporation). The average ligament sizes were calculated by measuring the diameter of >50 ligament, while the average pore sizes were calculated by averaging >50 spacing between ligaments, except for npAu-Pt_{0.5} sample whose ligaments and pores were too small to observe clearly by SEM. X-ray diffraction (XRD; X’Pert Pro by PANalytical) measurements were performed on the npAu-Pt, npAu and fAu specimens. Their chemical compositions were investigated by energy-dispersive X-ray (EDX; XFlash 5010, Bruker AXS, Germany) spectroscopy.

4.2.2 Bacterial strain

Type strains of *E. coli* (K-12, NBRC 3301) were supplied by the National Institute of Technology and Evaluation (Tokyo, Japan). We incubated the bacteria in Luria-Bertani (LB) medium at 308 K for 44 h before treating them in antimicrobial tests. Casein-peptone glucose yeast extract LB (Wako Pure Chemical Industries Ltd., Osaka, Japan) was used for the incubation.

4.2.3 Tests of antimicrobial activity (AA)

The antimicrobial properties of npAu-Pt, npAu and fAu were investigated mainly according to the Japanese Industrial Standard (JIS) “Antibacterial products-Test for antibacterial activity and efficacy” [25]. First, one quantity of platinum loop of bacteria

incubated in the medium was removed from the colony and placed in 5 mL of 1/500 nutrient broth, followed by vortex mixing. Second, 400 μ L of the bacterial suspension was dropped onto the samples and then a 40 \times 40 mm PE film covered the bacterial suspension. In this way, bacterial suspensions were incubated on the specimen for 24 h in humidity-controlled incubators at 308 K and at a relative humidity (RH) of 50%. The RH is 90% in JIS; however, the AAs for fAu and npAu were almost zero at an RH of 90% [11]. Therefore, the AA tests were carried out at the intermediate RH of 50%. Third, the incubated bacteria were recovered using 10 mL of Soybean Casein Digest Broth with Lectithin & Polysorbate 80 (SCDLP) medium and diluted 10-fold in phosphate-buffered saline (PBS). The diluted PBS was mixed in LB medium to make a 10-fold dilution series of LB pour plates. These were then incubated at 308 K for 48 h. The number of colonies in the LB pour plates was then counted. Viable bacteria counts (VBCs) were statistically analyzed by the one-way analysis of variance followed by a post-hoc test. The AA was given by

$$AA = \log_{10}(N_0/N) \quad (4.1)$$

in which N_0 is the viable bacteria count for fAu (as a control sample) and N is the viable bacteria count for npAu-Pt or npAu. The mean value of AA was obtained from 5 repeated tests. All results are expressed as mean \pm standard deviation.

4.2.4 Inductively coupled plasma (ICP) atomic emission spectrophotometry measurements

The culturing solution was suspended on the npAu-Pt substrate for 24 h, and the sample was then analyzed using ICP atomic emission spectroscopy. The concentrations of silver, gold, and platinum ions in the culturing solutions were found to be <0.05 ppm

of the apparatus detection limit. At least approximately 1 ppm is necessary for realizing the antimicrobial properties of Ag ions [4, 26-28]. Therefore, the effect of Ag ion dissolution on AA could be ignored.

4.2.5 Ultraviolet photoelectron spectrometry (UPS) measurements

WFs of npAu-Pt, npAu and fAu were measured with a PHI 5000 VersaProbe II Scanning ESCA Microprobe system (ULVAC-PHI, Chigasaki, Japan). A windowless helium discharge light source that provided HeI emission at 21.22 eV was used. The diameter of a vacuum-ultraviolet (VUV) light beam was 5 mm and the incident angle was 45°. The samples were biased at -5 V dc to drive low-energy secondary electrons into the detector to prevent signal cut-off owing to the detector. The work function (WF) Φ , can be given by

$$E_{\text{fermi}} - E_{\text{cutoff}} = \Phi - h\nu \quad (4.2)$$

in which E_{fermi} is the binding energy of the electron at fermi level, E_{cutoff} is the energy of the low-energy secondary electron, and $h\nu$ is the photon energy (21.22 eV). Before the measurements, the surfaces were cleaned by removing organic molecules using gas cluster ion beam (GCIB) of Ar emission for 5 minutes.

4.2.6 First-principles calculations of Au surfaces

We performed first-principles calculations for geometry optimization calculation of Au surface models by using the Cambridge Serial Total Energy Package (CASTEP) [29], in which a plane-wave basis set was used to calculate the electronic properties based on density functional theory (DFT) [30,31]. The Perdew-Burke-Ernzerhof functional (PBE) version of the generalized gradient approximation [32] was used to represent exchange

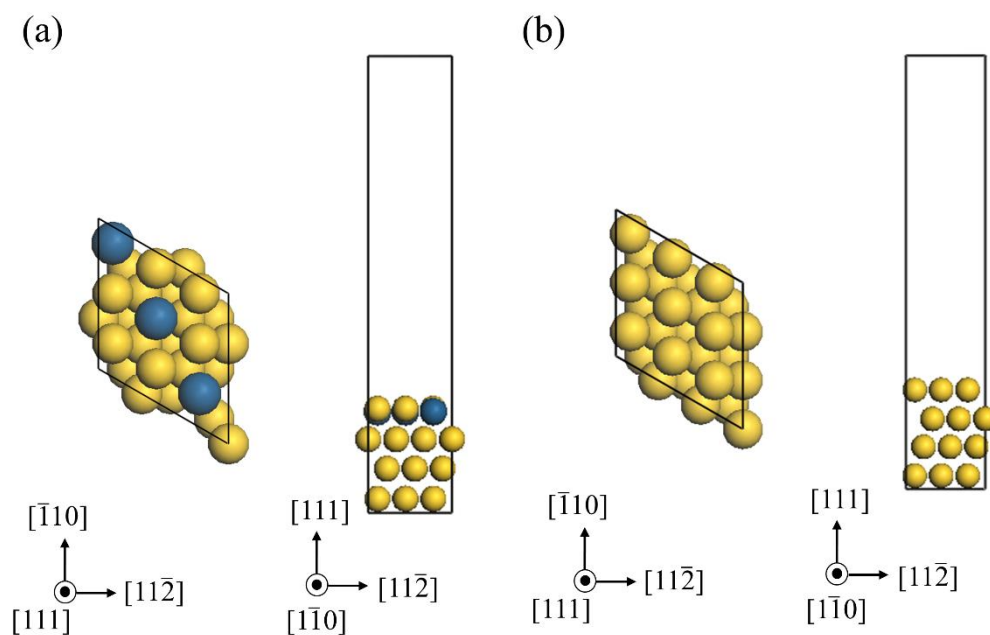


Figure 4.1 Simulation models used for first-principles calculation. (a), npAu-Pt model. (b), npAu model. The models have a slab geometry with 4 atomic layers of 4×4 and a vacuum layer of 30 Å. The 5% compressive strain is loaded in the simulation models. The yellow and blue atoms are Au and Pt atoms, respectively.

and correlation interactions within the DFT. Ultrasoft pseudopotentials [33] were used for all elements in the calculations. The cutoff energy was set to 320 eV and the Brillouin zone was sampled using $5 \times 5 \times 1$ Monkhorst-Pack k-point meshes in all calculations [34]. Periodic boundary conditions were applied in the x, y, and z directions for all of the calculations.

A slab geometry with 4 atomic layers of 4×4 and a vacuum layer of 30 Å was used to model npAu-Pt, npAu and fAu surfaces (Fig. 4.1). In the models, Ag atoms were not considered because effects of Ag atoms on the AA were ignorable. The atoms at the top three layers were relaxed to their equilibrium positions and the atoms at the bottom layer were frozen at their bulk positions in the models. Nanoporous metals have large lattice strains of up to 10% at the surfaces [35,36]. A previous study [12] showed that a cell wall was hyperpolarized when the cell wall was adsorbed on the (111) surface of npAu with 5% compressive lattice strain. Thus, the Au (111) surface with 5% compressive lattice strain was used as the npAu model in the present study. To create a npAu-Pt model, three Au atoms of the first layer in the npAu model were substituted by Pt atoms. The Pt concentration in the Au-Pt model almost corresponded to the experimental one, which was detected by XPS for npAu-Pt_{0.5}. The WF was calculated with these surface models, in which the WF was defined as the energy difference between the electrostatic potential at the middle of the vacuum region and the Fermi energy [14].

4.2.7 Molecular dynamics simulation and first-principles calculations of hyperpolarization of peptidoglycan

The hyperpolarization of peptidoglycan interacting with npAu-Pt, npAu or fAu was calculated by first-principles calculations and molecular dynamics (MD) simulations with

the same methods used in a previous study [12]. A scaffold model of peptidoglycan was constructed. The peptidoglycan was immersed in a spherical water solvation, where the center of water solvent was positioned at the mass center of peptidoglycan and the diameter of the spherical solvent water was 50.0 nm. Counter ions of 43 Na⁺ and 43 Cl⁻ were added to neutralize the system. The system was energy-minimized using the steepest decent algorithm (200,000 steps) and the conjugate gradient algorithm (100,000 steps). MD simulations were performed with a time step of 2.0 fs. The system was gradually heated from 5 to 300K for 4ps to activate thermal motion in the system. The system was equilibrated for 1 ns to obtain a stable structure of peptidoglycan with a constant number of particles, volume and temperature (NVT). Finally, the 10 ns NVT simulations were performed.

An interaction between MurNAc, which is a part of peptidoglycan, and the Au surface was calculated by first-principles calculations. A $4\sqrt{3} \times 3\sqrt{3}$ unit cell, which consisted of four Au layers, with a lattice strain of -5% was used as a npAu surface model (Fig. 4.2). A vacuum gap of 15 Å was added to create the surface. For the npAu-Pt model, 12 Au atoms of the surface layers were substituted by Pt atoms, in which the replaced positions were the same as those in Fig. 4.1 (Fig. 4.2). The geometry optimization calculations were performed on the Au surface models by first-principles calculations using the Dmol3 code [37,38]. In the DMol3 method, the physical wave functions were expanded in terms of the accurate numerical basis sets. The exchange-correlation energies were treated according to the generalized gradient approximation (GGA) with the Perdew-Wang 1991 (PW91) approximation [39] to deal with the core (DNP). The

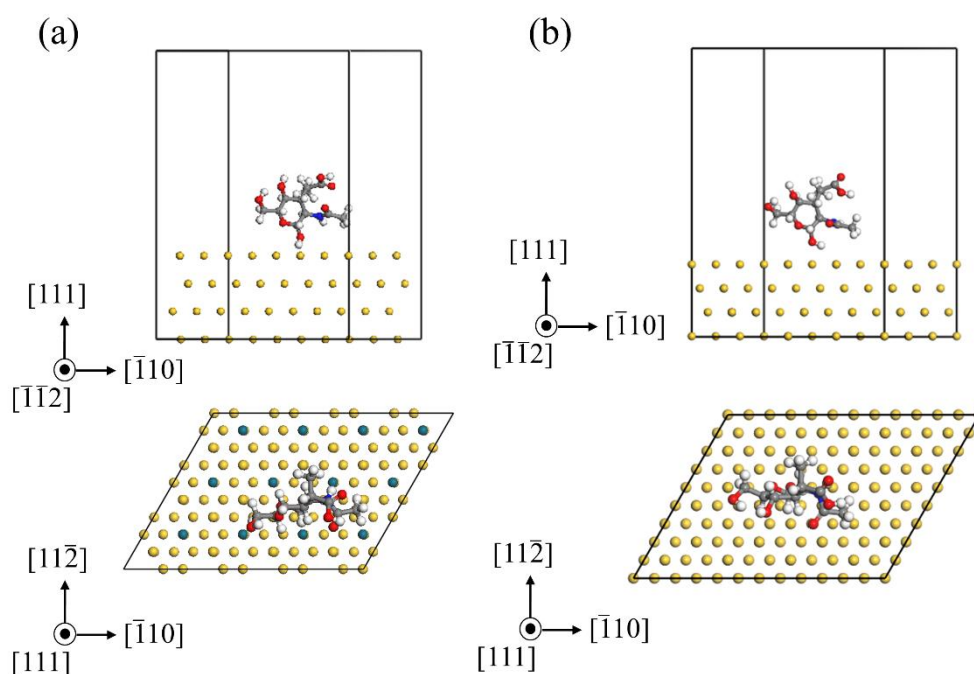


Figure 4.2 Simulation models used for adsorption of peptidoglycan on npAu and npAu-Pt models. (a), npAu-Pt model. (b), npAu model. The models have a slab geometry with 4 atomic layers of $4\sqrt{3} \times 3\sqrt{3}$ and a vacuum layer of 15 Å. A 5% compressive strain is loaded in the simulation models. The white, gray, red, dark blue, yellow and blue atoms are H, C, O, N, Au and Pt atoms, respectively.

ultrasoft pseudopotentials [33] represented in reciprocal space were used for all elements in the calculations. Optical Bloch equation (OBE) calculations were used to set the van der Waals interactions into calculations. A Fermi smearing of 0.005 hartree (1 hartree = 27.2114 eV) was adopted. A Brillouin zone of $2 \times 2 \times 1$ using a Monkhorst-Pack k-point mesh [34] was used. The bottom layer of the cell was frozen during geometry optimization calculations. MurNAc was positioned to be the atop site [12].

After the geometry optimizations of a MurNAc molecule located on the atop site of the Au surface model, a MurNAc molecule was put back at the same position in the original peptidoglycan model, and 1 ns MD simulations were performed again, in which the atomic positions of the MurNAc molecule were fixed during the calculations. Then, electrostatic potentials of the obtained peptidoglycan were calculated by solving the Poisson Boltzmann equation using the finite difference method implemented in the Delphi program [40,41]. The values of the atomic radii and partial atomic charges were taken from the CHARMM parameter set. The peptidoglycan was divided into a three-dimensional cubical grid and the electrostatic potential at each grid point was computed.

4.3 Results and Discussion

The nanoporous Au-Pt and Au are shown in Fig. 4.3. The average ligament and pore size were 5 and less than 2 nm for npAu-Pt_{0.5}, 15 and approximately 10 nm for npAu-Pt_{0.1}, and 34 and approximately 20 nm for npAu. The ligament and pore sizes of npAu-Pt were lower than those of npAu [42]. The smaller pore structure of the npAu-Pt alloy was

Table 4.1 Work function measured from the UPS spectrum.

Specimens	Work function (eV)
npAu-Pt _{0.5}	5.15
npAu-Pt _{0.1}	5.33
npAu(20nm)	5.81
npAu(50nm)	5.52
fAu	5.07

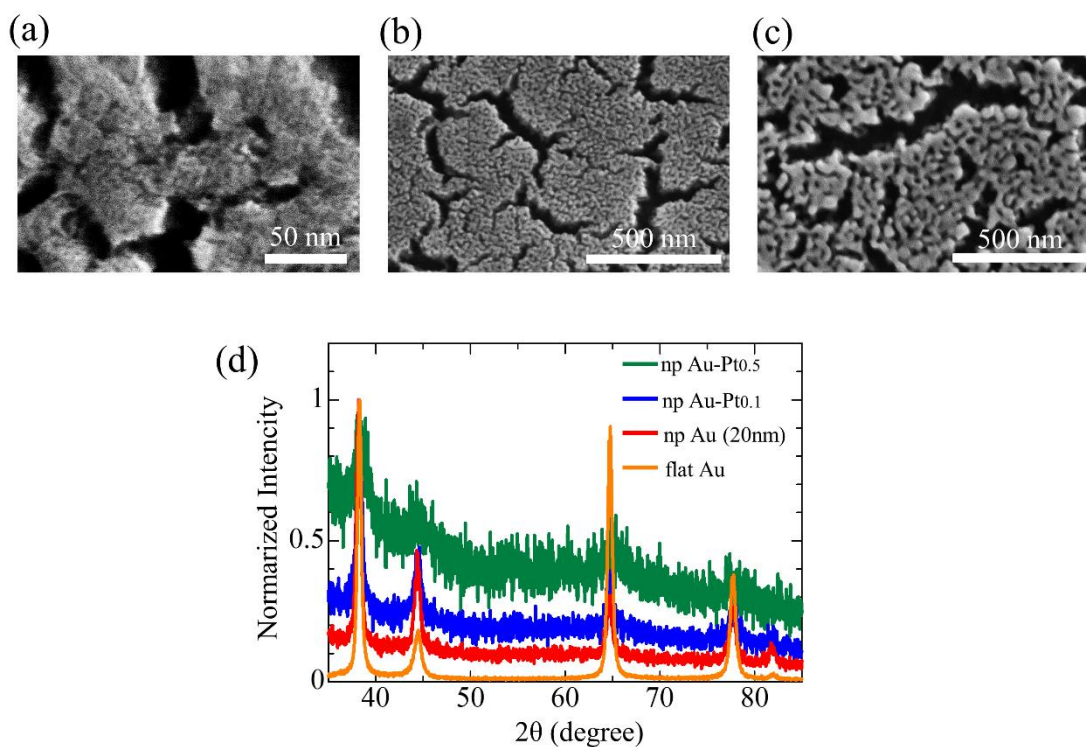


Figure 4.3 Nanoporous Au-Pt and Au fabricated by dealloying. (a)-(c), SEM images of npAu-Pt_{0.5}, npAu-Pt_{0.1} and npAu (20nm). (d), XRD measurements of npAu-Pt_{0.5}, npAu-Pt_{0.1}, npAu (20nm) and flat Au (fAu), where green, blue, red and orange lines show XRD of npAu-Pt_{0.5}, npAu-Pt_{0.1}, npAu (20nm) and flat Au (fAu), respectively.

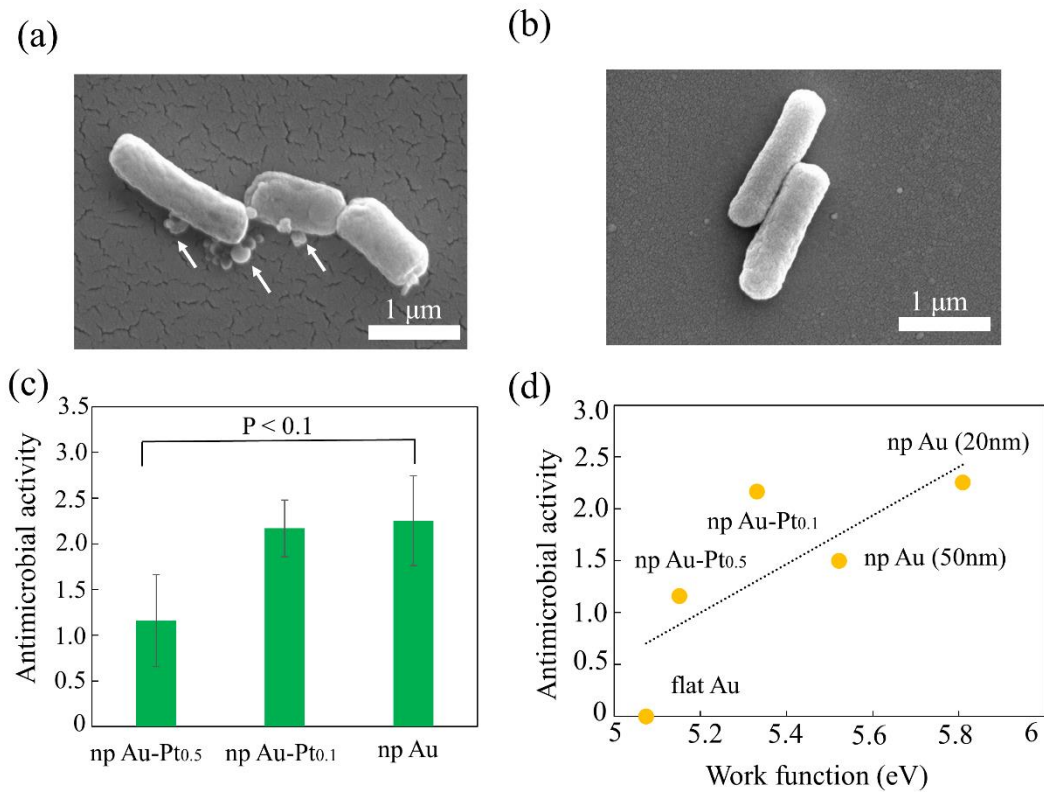


Figure 4.4 Results of antimicrobial activity tests. (a), SEM image of *E. coli* cultured on npAu-Pt_{0.5}. *E. coli* cultured on npAu-Pt_{0.5} was dead and its cell membrane was broken (cytoplasm drained out of bacterial body, as indicated by arrows). (b), SEM image of *E. coli* cultured on flat Au (fAu). *E. coli* cultured on fAu was not dead. (c), Antimicrobial activities (AA) of npAu-Pt and npAu. (d), Relationship between AA and work function (WF). In the figure, npAu (20nm) is for npAu with a pore size of 20 nm and npAu (50nm) is for npAu with a pore size of 50 nm. The AA of npAu (50nm) is the one obtained in the previous study [11].

attributed to the lower surface diffusion of Pt [35]. Alloying of npAu with Pt reduced the lattice constant (Fig. 4.3 (d)). The reduction in the lattice constant by the Pt addition almost corresponded to Vegard's law.

Residual Ag in npAu-Pt and npAu may affect the AA because the Ag ion is a strong killer of bacteria [3]. The Ag concentration was 16.75 at.% for npAu-Pt_{0.5}, 7.23 at.% for npAu-Pt_{0.1} and 0.85 at.% for npAu (Table 4.1). However, the Ag concentration in the culture medium after the AA tests was less than the detection limit of the inductively coupled plasma (ICP) atomic emission spectrophotometry measurements. Therefore, the effect of residual Ag on the AA was low enough to be ignored.

Figure 4.4 shows results of the antimicrobial tests. A large number of *E. coli* cultured on the npAu-Pt_{0.5} were dead, whereas only a few *E. coli* cultured on the fAu were dead in the AA tests. It appeared that the cell membrane was broken for *E. coli* cultured on the npAu-Pt_{0.5} (Fig. 4.4 (a), (b)). This corresponded to that for *E. coli* cultured on npAu [11], suggesting that the AA mechanism for npAu-Pt was the same as that for npAu. The AAs were 1.2 ± 0.5 , 2.2 ± 0.3 and 2.3 ± 0.5 for npAu-Pt_{0.5}, npAu-Pt_{0.1} and npAu, respectively (Fig. 4.4 (c)). Differences between npAu-Pt_{0.5} and npAu were considered statistically significant at a P-value < 0.1. Alloying with Pt reduced the AA of npAu. The reduced AA by alloying with Pt was not due to residual Ag because the residual Ag contents for the npAu-Pt were larger than that for the npAu. The smaller pore and ligand size enhanced the AA of npAu [11]. Hence, the finer pore structure of the npAu-Pt was not responsible for the reduced AA after alloying with Pt.

The WF was measured from the UPS spectrum (Fig. 4.5). The measured work function is listed in Table 4.1. The WF of fAu agreed with the value measured from the

Fowler plot [43]. The WFs of npAu-Pt and npAu were larger than that of fAu, indicating that the surface effect enhanced the spilling out of electrons at the surfaces. Noted that there was a positive correlation between the AA and the WF, in which the coefficient of correlation was 0.73 (Fig. 4.4 (d)). This demonstrated that the WF was representative of the intensity of the surface effect that leads to AA. The two series of npAu-Pt showed lower AA than the npAu with a pore size of 20 nm, despite the smaller pore size of npAu-Pt. It is therefore suggested that alloying with Pt changed the electronic states, resulting in reduced AA.

We performed first-principles calculations to investigate the origins of the variation in the electronic states after alloying with Pt. In the calculation, the WF was defined as the energy difference between the electrostatic potential at the middle of the vacuum region and the Fermi energy [14]. The order of calculated WF was $WF(\text{npAu}) > WF(\text{npAu-Pt}) > WF(\text{fAu})$ (Fig. 4.6). This trend agreed with the experimental one.

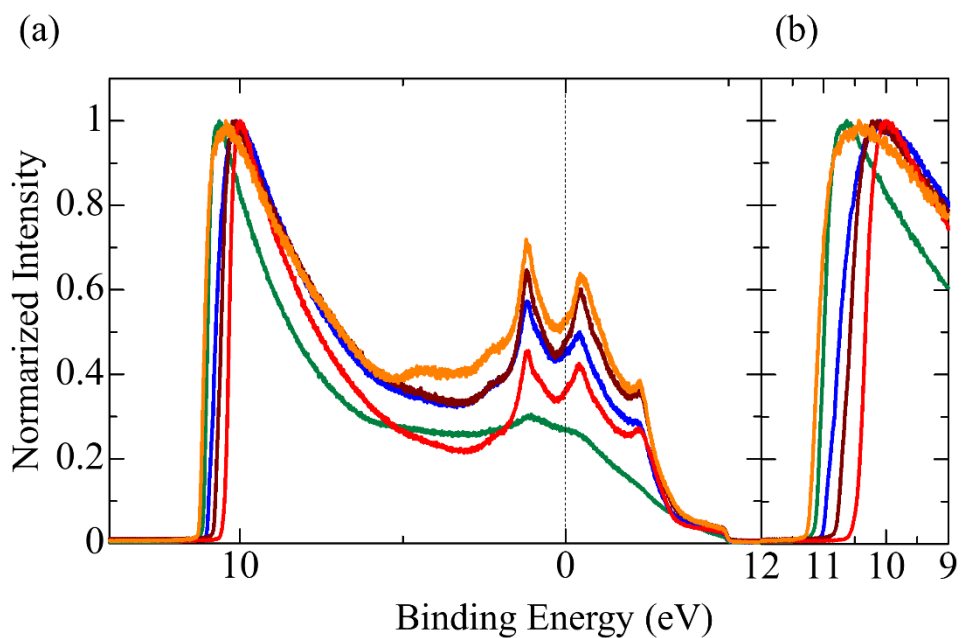


Figure 4.5 Spectrums obtained by UPS measurements. (a), Whole spectrum. (b), Initial part of the spectrum in which green, blue, brown, red and orange lines are the spectra of npAu-Pt_{0.5}, npAu-Pt_{0.1}, npAu (50 nm), npAu (20 nm) and flat Au, respectively. The work function is calculated from the energy at the flexion point of the spectrum.

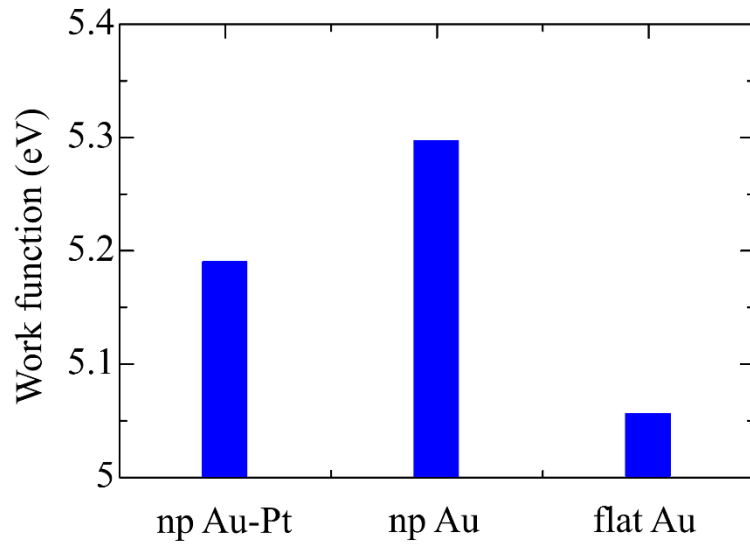


Figure 4.6 Work function obtained by first-principles calculation. The work function (WF) is defined as the energy difference between the electrostatic potential at the middle of the vacuum region and the Fermi energy. The order of calculated WF is $WF(npAu) > WF(npAu-Pt) > WF(fAu)$.

Nanoporous metals have large lattice strains of up to 10% at the surfaces, because the nanosized ligaments have high positive and negative curvatures [35,36]. Therefore, a 5% compressive strain was loaded in the simulation models of npAu and npAu-Pt; the larger WFs for npAu-Pt and npAu can be explained from the compressive strain [23,24].

The WF mainly results from the spilling out of electrons and electric double layer formation at the metallic surface [13,14]. Hence, the variation in WF by alloying with Pt can be investigated by the electron charge difference between npAu-Pt and npAu ($=\rho_{\text{npAu-Pt}} - \rho_{\text{npAu}}$, in which ρ_{npAu} and $\rho_{\text{npAu-Pt}}$ are the electron density of npAu and npAu-Pt, respectively). The first-principle calculations were performed to investigate the electron charge difference. The result is shown in Fig. 4.7 (a). The electron charge difference was negative in the vacuum region except for the Au atomic radius. This means that alloying with Pt reduces the spilling out of electrons. The charge densities of the surfaces are shown in Figs. 4.7 (b) and 4.7 (c). More charge was accumulated between the first and the second layer of npAu-Pt than of npAu because the charge transfer occurred from Pt to Au atoms for npAu-Pt. On the other hand, the chemical (covalent) bonding between Au and Pt atoms may also affect the variation in WF [44]. However, such chemical bonding was not generated between Au and Pt atoms in npAu-Pt (Fig. 4.8). Therefore, it is suggested that the reduced WF by alloying with Pt was mainly related to the charge transfer from Pt to Au atoms. Another factor affecting the WF is the geometric effect [22]. There are a large number of atomic steps at the surfaces of npAu [45]. The density of atomic steps may be higher for npAu-Pt than for npAu because of the smaller pore

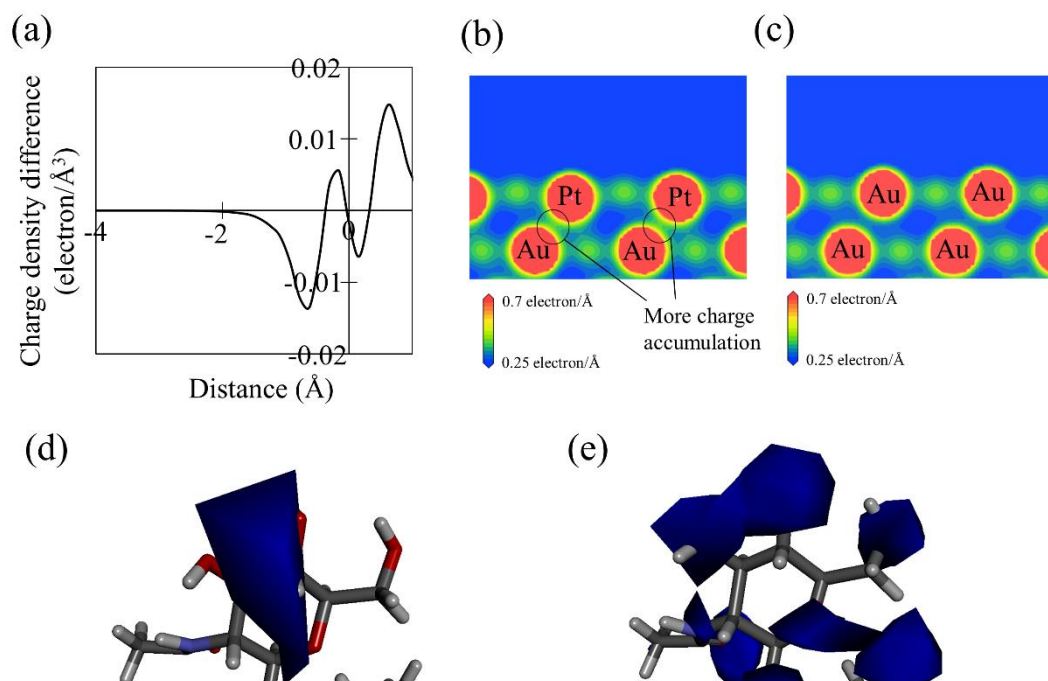


Figure 4.7 Results of first-principles calculation and molecular dynamics simulation. (a), Electron charge difference between npAu-Pt and npAu ($=\rho_{\text{npAu-Pt}} - \rho_{\text{npAu}}$, in which ρ_{npAu} and $\rho_{\text{npAu-Pt}}$ are the electron density for npAu and for npAu-Pt, respectively) of the (100) plane. The (100) plane containing no Pt atoms was investigated for npAu-Pt. The horizontal axis shows the distance from the center of the first layer Au atom, and the positive (negative) value indicates the bulk (vacuum) region. (b) & (c), Charge density of the (121) plane for npAu-Pt and for npAu. The (121) plane containing three Pt atoms was investigated for npAu-Pt. (d) & (e), Electrostatic potential of peptidoglycans located on npAu-Pt and on npAu, where gray, white and red atoms are carbon, hydrogen and oxygen

atoms, respectively, and the blue region show the isosurface of electrostatic potential. The isosurface value is negative value of $-6kT$.

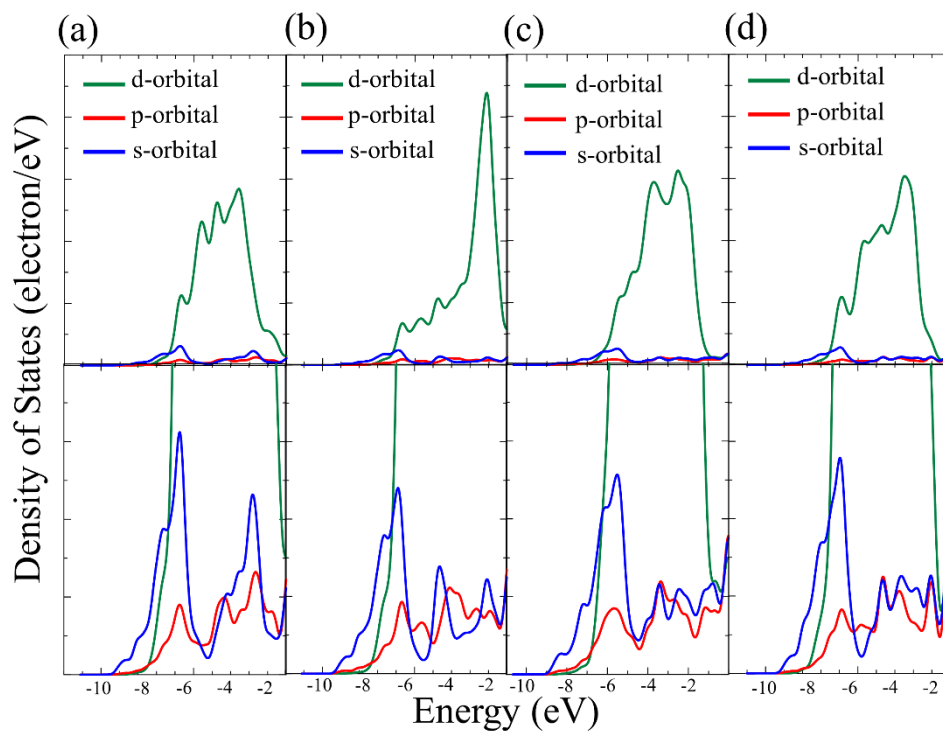


Figure 4.8 Density of electronic states (DOS). (a), DOS of Au atom in npAu-Pt. (b), DOS of Pt atom in npAu-Pt. (c), DOS of Au atom in npAu. (d), DOS of Au atom in flat Au. The green, blue and red lines show s-, p- and d-orbitals, respectively. The upper panels focus on DOS of d-orbitals and the lower panels on DOS of s- and p-orbitals. Chemical (covalent) bonding is not generated between Au and Pt atoms in npAu-Pt.

structure of npAu-Pt. The higher density of atomic steps can reduce the WF owing to the Smoluchowski mechanism [13]. Therefore, the lower WF of npAu-Pt may be partly related to the higher density of atomic steps.

The electrostatic potential of peptidoglycans interacting with npAu-Pt and with npAu is shown in Figs. 4.7 (d) and 4.7 e. The peptidoglycans interacting with npAu-Pt as well as with npAu were negatively hyperpolarized, but the intensity of hyperpolarization of the peptidoglycan with npAu-Pt was weaker than that with npAu. This is because alloying with Pt reduced the spilling out of electrons. Therefore, the reduced spilling out of electrons owing to alloying with Pt weakened the hyperpolarization of bacterial cell walls. This resulted in a reduction in AA by alloying npAu with Pt.

A possible approach for further elucidation of the whole mechanism and phenomena is the analyses of gene expression in *E. coli* such as real-time PCR and microarray analysis [11]. The approach may make it possible to clearly differentiate the antimicrobial mechanism of nanoporous noble metals from that of noble metal nanoparticles.

4.4 Conclusions

The antimicrobial activity and the work function of nanoporous Au-Pt, nanoporous Au and flat Au were investigated. As a result, there was a positive correlation between them. Thus, the work function was representative of the surface effect leading to the antimicrobial activity. A first-principles calculation and molecular dynamics simulation showed that the positive correlation is owing to peculiar electronic states at the Au surface, namely, the spilling out phenomenon of electrons.

References

- [1] S. M. Barlow, K. J. Kitching, S. Haq and N. V. Richardson, "A Study of Glycine Adsorption on a Cu {110} Surface Using Reflection Absorption Infrared Spectroscopy", *Surf. Sci.* **401**, (1998) 322-335.
- [2] B. Loganathan, V. L. Chandraboss, S. Senthilvelan and B. Karthikeyan, "Surface Enhanced Vibrational Spectroscopy and First-Principles Study of L-Cysteine Adsorption on Noble Trimetallic Au/Pt@Rh Clusters", *Phys. Chem. Chem. Phys.* **17**, (2015) 21268-21277.
- [3] G. Zhao and S. E. Stevens Jr., "Multiple Parameters for the Comprehensive Evaluation of the Susceptibility of *Escherichia coli* to the Silver ion", *BioMetals* **11**, (1998) 27-32.
- [4] B. Galeano, E. Korff and W. L. Nicholson, "Inactivation of Vegetative Cells, but not Spores, of *Bacillus anthracis*, *B. cereus*, and *B. subtilis* on Stainless Steel Surfaces Coated with an Antimicrobial Silver- and Zinc-Containing Zeolite Formulation", *Appl. Environ. Microbiol.* **69**, (2003) 4329-4331.
- [5] F. U. Khan *et al.*, "Visible Light Inactivation of *E. coli*, Cytotoxicity and ROS Determination of Biochemically Capped Gold Nanoparticles", *Microbial Pathogenesis* **107**, (2017) 419-427.
- [6] Cui, Y. *et al.*, "The Molecular Mechanism of Action of Bactericidal Gold Nanoparticles on *Escherichia coli*." *Biomater.* **33**, (2012) 2327-2333.
- [7] Y. Zhang, H. Peng, W. Huang, Y. Zhou and D. Yan, "Facile Preparation and Characterization of Highly Antimicrobial Colloid Ag or Au Nanoparticles", *J. Colloid Interface Sci.* **325**, (2008) 371-376.

- [8] J. F. Hernandez-Sierra *et al.*, “The Antimicrobial Sensitivity of *Streptococcus mutans* to Nanoparticles of Silver, Zinc Oxide, and Gold”, *Nanomed.-Nanotechnol. Biol. Med.* **4**, (2008) 237-240.
- [9] V. Zielasek *et al.*, “Gold Catalysts: Nanoporous Gold Foams”, *Angew. Chem. Int. Ed.* **45**, (2006) 8241-8244.
- [10] A. Wittstock, V. Zielasek, J. Biener, C. M. Friend and M. Bäumer, “Nanoporous Gold Catalysts for Selective Gas-Phase Oxidative Coupling of Methanol at Low Temperature”, *Science* **327**, (2010) 319-322.
- [11] M. Hakamada, S. Taniguchi and M. Mabuchi, “Antimicrobial Activity of Nanoporous Gold against *Escherichia coli* and *Staphylococcus epidermidis*”, *J. Mater. Res.* **32**, (2017) 1787-1795.
- [12] N. Miyazawa, M. Hakamad and M. Mabuchi, “Antimicrobial Mechanisms due to Hyperpolarization Induced by Nanoporous Au”, *Sci. Rep.* **8**, (2018) 3870.
- [13] R. Smoluchowski, “Anisotropy of the Electronic Work Function of Metals”, *Phys. Rev.* **1**, (1941) 661-674.
- [14] N. D. Lang and W. Kohn, “Theory of Metal Surfaces: Work Function”, *Phys. Rev. B* **3**, (1971) 1215-1223.
- [15] F. N. Lloyd *et al.*, “Reversible Work Function Changes Induced by Photoisomerization of Asymmetric Azobenzene Dithiol Self-Assembled Monolayers on Gold”, *Appl. Phys. Lett.* **93**, (2008) 083109.
- [16] N. Gozlan, U. Tisch and H. Haick, “Tailoring the Work Function of Gold Surface by Controlling Coverage and Disorder of Polar Molecular Monolayers”, *J. Phys. Chem. C* **112**, (2008) 12988-12992.

- [17] L. -L. Wang and H. -P. Cheng, “Density Functional Study of the Adsorption of a C60 Monolayer on Ag(111) and Au(111) Surfaces”, *Phys. Rev. B* **69**, (2004) 165417.
- [18] D. Otalvaro, T. Veening and G. Brocks, “Self-Assembled Monolayer Induced Au(111) Ag(111) Reconstructions: Work Functions and Interface Dipole Formation”, *J. Phys. Chem. C* **116**, (2012) 7826-7837.
- [19] F. Mehmood, A. Kara, T. S. Rahman and C. R. Henry, “Comparative Study of CO Adsorption on Flat, Stepped, and Kinked Au Surfaces Using Density Functional Theory”, *Phys. Rev. B* **79**, (2009) 075422.
- [20] M. Malicki *et al.*, “Preparation and Characterization of 4'-donor Substituted Stilbene-4-Thiolate Monolayers and Their Influence on the Work Function of Gold”, *Langmuir* **25**, (2009) 7967-7975.
- [21] T. C. Leung, C. L. Kao, W. S. Su, Y. J. Feng and C. T. Chan, “Relationship between Surface Dipole, Work Function and Charge Transfer: Some Exceptions to An Established Rule”, *Phys. Rev. B* **68**, (2003) 195408.
- [22] L. H. F. Rafael, K. Adam & L. F. D. S. Juarez, “Adsorption of Rh, Pd, Ir, and Pt on the Au(111) and Cu(111) Surfaces: a Density Functional Theory Investigation”, *J. Phys. Chem. C* **118**, (2014) 19051-19061.
- [23] W. Li, M. Cai, Z. Zong and S. Yu, “Variation of Surface Morphology and Electronic Behavior under Dynamic Tensile Conditions”, *Scr. Mater.* **88**, (2006) 181902.
- [24] X. F. Wang *et al.*, “The Canonical Work Function-Strain Relationship of the Platinum Metal: A First-Principles Approach to Metal-Gate Transistor Optimization”, *Appl. Phys. Lett.* **102**, (2013) 223504.
- [25] “Japanese Standards Association, Japanese Industrial Standard (JIS) Z 2801

Antibacterial Products-Test for Antibacterial Activity and Efficacy”.

[26] C.-N. Lok *et al.*, “C.-M. Proteomic Analysis of the Mode of Antibacterial Action of Silver Nanoparticles”, *J. Proteome Res.* **5**, (2006) 916-924.

[27] C. P. Randall, L. B. Oyama, J. M. Bostock, I. Chopra and A. J. O’Neill, “The Silver Cation (Ag⁺): Antistaphylococcal Activity, Mode of Action and Resistance Studies”, *J. Antimicrob. Chemother.* **68**, (2013) 131-138.

[28] N. Miura and Y. Shinohara, “Cytotoxic Effect and Apoptosis Induction by Silver Nanoparticles in HeLa cells”, *Biochem. Biophys. Res. Commun.* **390**, (2009) 733-737.

[29] M. C. Payne, M. P. Teter, D. C. Allan, T. A. Arias and J. D. Joannopoulos, “Iterative Minimization Techniques for Ab Initio Total-Energy Calculations: Molecular Dynamics and Conjugate Gradients”, *Rev. Mod. Phys.* **64**, (1992) 1045-1097.

[30] P. Hohenberg and W. Kohn, “Inhomogeneous Electron Gas”, *Phys. Rev.* **136**, (1964) B864-B871.

[31] W. Kohn and L. Sham, “Self-Consistent Equations Including Exchange and Correlation Effects”, *Phys. Rev.* **140**, (1965) A1133-A1138.

[32] J. P. Perdew, K. Burke and M. Ernzerhof, “Generalized Gradient Approximation Made Simple”, *Phys. Rev. Lett.* **77**, (1996) 3865-3868.

[33] D. Vanderbilt, “Soft Self-Consistent Pseudopotentials in a Generalized Eigenvalue Formulation”, *Phys. Rev. B* **14**, (1990) 7892.

[34] H. J. Monkhorst and D. P. James, “Special Points for Brillouin-Zone Integrations”, *Phys. Rev. B* **13**, (1976) 5188.

[35] S. Parida, *et al.*, “Volume Change during the Formation of Nanoporous Gold by Dealloying”, *Phys. Rev. Lett.* **97**, (2006) 035504.

- [36] M. Hakamada, H. Nakano, T. Furukawa, M. Takahashi, and M. Mabuchi, “Hydrogen Storage Properties of Nanoporous Palladium Fabricated by Dealloying”, *J. Phys. Chem. C* **114**, (2010) 868-873.
- [37] B. J. Delley, “An All-Electron Numerical Method for Solving the Local Density Functional for Polyatomic Molecules”, *J. Chem. Phys.* **92**, (1990) 508-517.
- [38] B. J. Delley, “From Molecules to Solids with the Dmol3 approach”, *J. Chem. Phys.* **113**, (2000) 7756-7764.
- [39] J. P. Perdew *et al.*,” Atoms, Molecules, Solids and Surfaces: Applications of the Generalized Gradient Approximation for Exchange and Correlation”, *Phys. Rev. B* **46**, (1992) 6671.
- [40] W. Rocchia, E. Alexov & B. Honig, “Extending the Applicability of the Nonlinear Poisson-Boltzmann Equation: Multiple Dielectric Constants and Multivalent Ions”, *J. Phys. Chem. B* **105**, (2001) 6507-6514.
- [41] W. Rocchia, S. Sridharan, A. Nicholls, E. Alexov, A. Chiabrera and B. Honig, “Rapid Grid-Based Construction of the Molecular Surface and the Use of Induced Surface Charge to Calculate Reaction Field Energies: Applications to the Molecular Systems and Geometric Objects”, *J. Comput. Chem.* **23**, (2002) 128-137.
- [42] J. Snyder, P. Asanithi, A. B. Dalton and J. Erlebacher, “Stabilized Nanoporous Metals by Dealloying Ternary Alloy Precursors”, *Adv. Mater.* **20**, (2008) 4883-4886.
- [43] R. H. Fowler, “The Analysis of Photoelectric Sensitivity Curves for Clean Metals at Various Temperatures”, *Phys. Rev.* **38**, (1931) 45-56.

CHAPTER5

WEAK INTERACTION CAUSES DYSFUNCTION OF A POTASSIUM ION CHANNEL

5.1 Introduction

Generally, interactions between biomacromolecules and inorganic/organic matters are classified into two kinds: strong interactions which are caused via strong Coulombic force (ionic binding) or covalent bonding, and weak interactions which is related to *intermolecular bonding* or weak Coulombic force. Most of nanomaterials shows antimicrobial activities via the strong interactions through reactive oxygen species (ROS) [1,2] and metallic ion [3]. Thus, the strong interactions are powerful for antimicrobial. On the other hand, weak interactions are also important for activities of biomacromolecules. For example, many enzyme reactions involve van der Waals and/or hydrophobic interactions [4]. However, there are poor understandings about roles of weak interactions in antimicrobial activity.

It is necessary to maintain ionic gradient inside and outside a cell for normal electrochemical gradient [5], and transportation and selectivity of various ions through ion channels are vital functions. Hence, ion channels are important *transmembrane* proteins to keep life, in particular, K^+ channel plays a vital role in *keeping the membrane*

potential. The overall structure of bacterial *KcsA* K^+ channel was observed using X-ray crystallography [6-8], which showed *that compatibility of high selectivity and high permeability is related to a sophisticated structure of the channel, in particular, the selectivity filter* [9-11]. Therefore, external weak interactions may cause serious dysfunction of K^+ channels because the structure of selectivity filter is very delicate.

As discussed in the previous chapter, the antimicrobial mechanism for NPG [12] is related to weak interaction between the NPG surface and the cell membrane of bacteria. The hyperpolarization of cell wall induced by NPG leads to slight structural changes in the membrane proteins, resulting in killing bacteria [13]. However, unclear at all is *how* the slight structural changes cause dysfunction of membrane proteins.

In the present work, effects of structural change of bacterial K^+ channel, which is induced by the hyperpolarized cell wall, on ionic permeability are studied by molecular dynamics simulations and first-principle calculations. The K^+ channels show a selectivity sequence of $K^+ > Cs^+ > Na^+$, for example, the permeability of K^+ is 10,000 times higher than that of Na^+ , while an ion diameter sequence is $Cs^+ > K^+ > Na^+$. Thus, the K^+ channel has high K^+ selectivity. In the present work, the permeabilities of K^+ , Na^+ and Cs^+ in the selectivity filter were investigated in the cases with or without interaction with the hyperpolarized cell wall.

5.2 Methods

5.2.1 Potassium channel interacting with hyperpolarized cell wall

The peptidoglycan model of scaffold model was obtained using molecular dynamics and first-principles simulations. The calculation method was the same used in the previous study [13]. The part of hyperpolarized peptidoglycan molecule was taken from the front edge of the peptidoglycan, where the taken part was GlcNAc molecule located furthest from the interaction point. The electrostatic potentials of hyperpolarized and non-hyperpolarized peptidoglycan molecules were shown in Figure 5.1 (a) and (b).

Initial coordinates for potassium channel were taken from the crystal structures 1K4C from protein data bank. The channel was embedded in a bilayer of 2,182 POPE lipid and solvated in 15,078 water molecules and 15 Cl⁻ ions to neutralize the system using CHARMM-GUI web site. Periodic boundary conditions were applied. Energy minimizations and MD simulations were performed using the CHARMM force field [14] using gromacs 5.1.1 code [15,16]. The system was energy-minimized using the steepest decent algorithm (500,000steps). MD simulations were performed at 300K with the time step of 1.0 fs. The system was equilibrated for 10 ns to obtain a stable structure of peptidoglycan with the constant number of particles, volume and temperature (NVT) ensemble. Finally, the 100 ns NVT simulations were performed. To investigate the effect

of hyperpolarization of the cell wall, a part of the hyperpolarized peptidoglycan molecule was positioned near the outermost amino acids of ion channel (about 5Å from Gly56), which is located outermost of ion channel (Figure 5.1 (c)). The energy minimization,

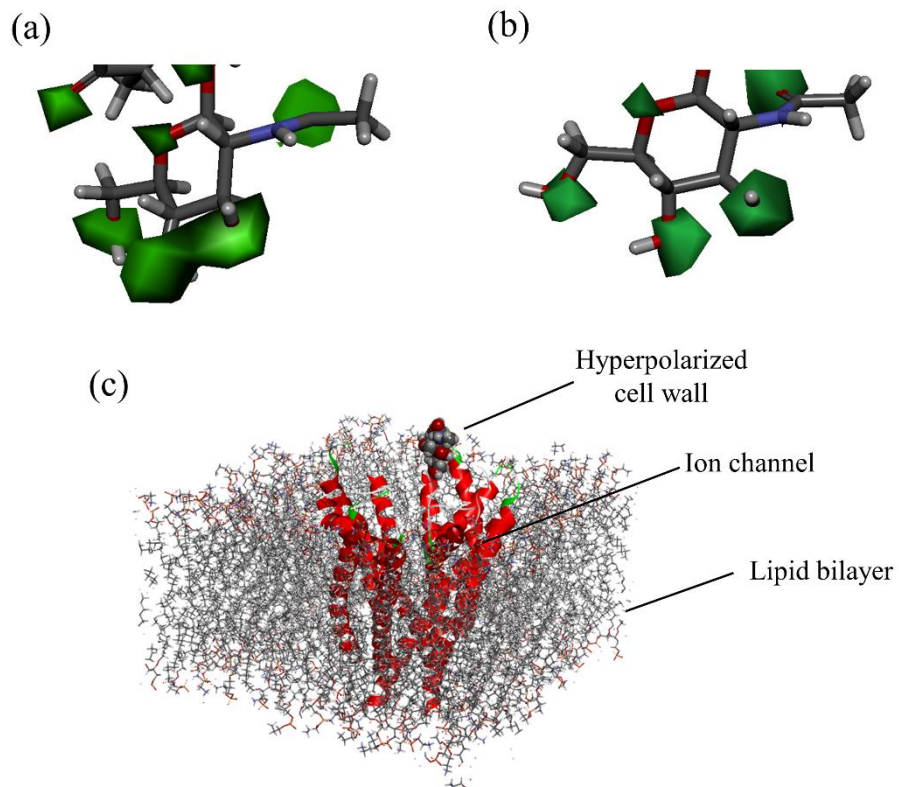


Figure 5.1 Simulation models used for molecular dynamics simulations. (a) & (b), Hyperpolarized and non-hyperpolarized cell wall. (c), Potassium channel interacting with hyperpolarized cell wall. The channel is embedded in POPE lipid bilayer.

equilibration and 100ns NVT simulations described above was conducted on ion channel models interacting with hyperpolarized cell wall.

5.2.2 Bias-exchange metadynamics simulations

Bias-exchange metadynamics simulations were performed to investigate the ionic velocity of sodium and potassium ions using Plumed 2.3.0 code [17] and gromacs 5.1.1 code [15,16]. The number of replicas were four, which is the number of ions considered in permeation and a neutral replica. The replicas other than neutral replicas were biased using a time-dependent metadynamics potential that acted on one dimensional collective variable (CV). This CV was defined as the coordinates of potassium and sodium ions positioned inside the selectivity filter (Figure 5.2), where the initial positions of ions were S1, S3 and S4 sites. Gaussians hills with height equal to 0.5nm and width equal to 0.3 nm were added to the biasing potential every 500 ps. Exchanges between replicas were attempted every 2 ps. The calculation was conducted for 1ns. The ionic velocity was calculated as the displacement per calculation time where the displacement was the difference of between final and initial coordinates.

5.2.3 First-principles calculations on the selectivity filter

The energy calculations were performed on the selectivity filter models by first-principles calculations using the Dmol3 code [18,19]. The selectivity filter model is

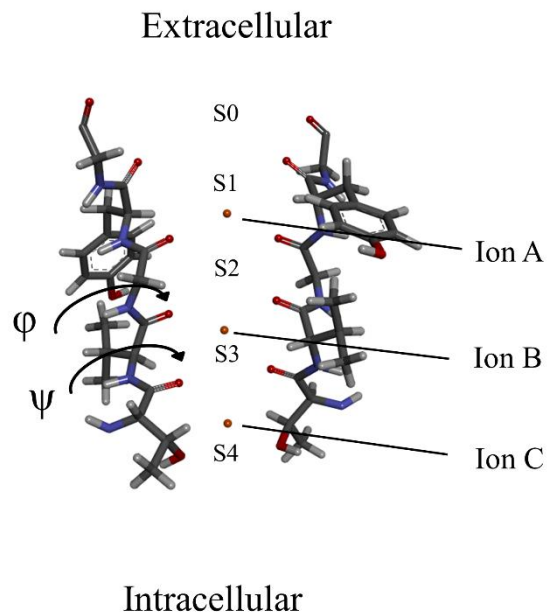


Figure 5.2 Schematic illustration of selectivity filter. The definitions of Ions A, B and C, S0 to S4 sites and dihedral angles (ψ and ϕ) are shown. White, black, red, blue and orange balls indicate hydrogen, oxygen, nitrogen atoms and potassium ions, respectively.

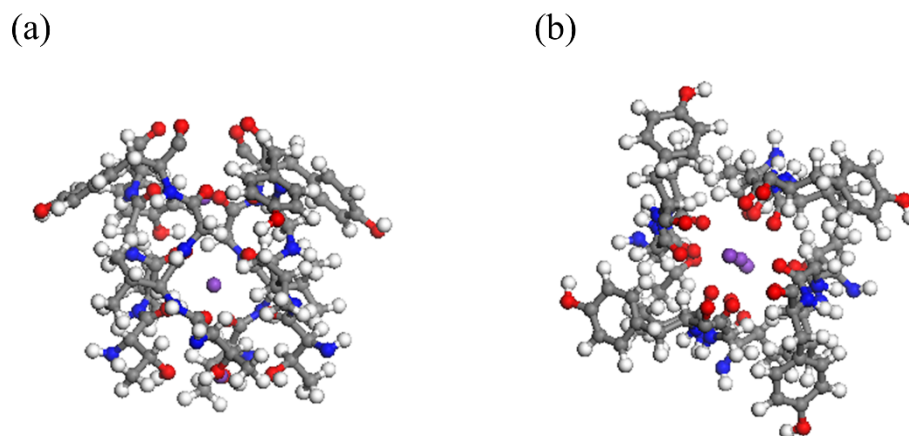


Figure 5.3 Simulation models used for first-principles calculations. (a) Side view., (b) Top view. Selectivity filter is composed of Thr74, Val76, Gly77, Tyr78 and Gly79. White, black, red, blue and purple balls indicate hydrogen, oxygen, nitrogen atoms and potassium ions, respectively.

shown in Figure 5.3, where Thr74, Val76, Gly77, Tyr78 and Gly79 were contained. In the DMol3 method, the physical wave functions were expanded in terms of the accurate numerical basis sets. The exchange-correlation energies were treated according to the generalized gradient approximation (GGA) with the Perdew-Wang 1991 (PW91) approximation [20] to deal with the core (DNP). The ultrasoft pseudopotentials [21] represented in reciprocal space were used for all elements in the calculations. Optical Bloch equation (OBE) calculations were used to set the van der Waals interactions into calculations.

5.3 Results and Discussions

In the selectivity filter, four strands of sequence TVGYG are located with carboxyl groups containing oxygen atoms which interact with passing cation ions [22]. It was believed that two ions move in a concerted fashion between two configurations such as ion-water-ion-water [23]. However, it was shown that ion conduction involves transitions between two main states, with two and three K^+ ions occupying the selectivity filter [24,25], that is “direct knock-on” mechanism. In the present work, the permeability was investigated based on the direct knock-on mechanism, where no water molecule exists between three ions passing in the selectivity filter. Noted that the permeabilities of all three K^+ ions were about 50% higher in the selectivity filter interacting with the hyperpolarized cell wall than in the one without the hyperpolarized cell wall, while the

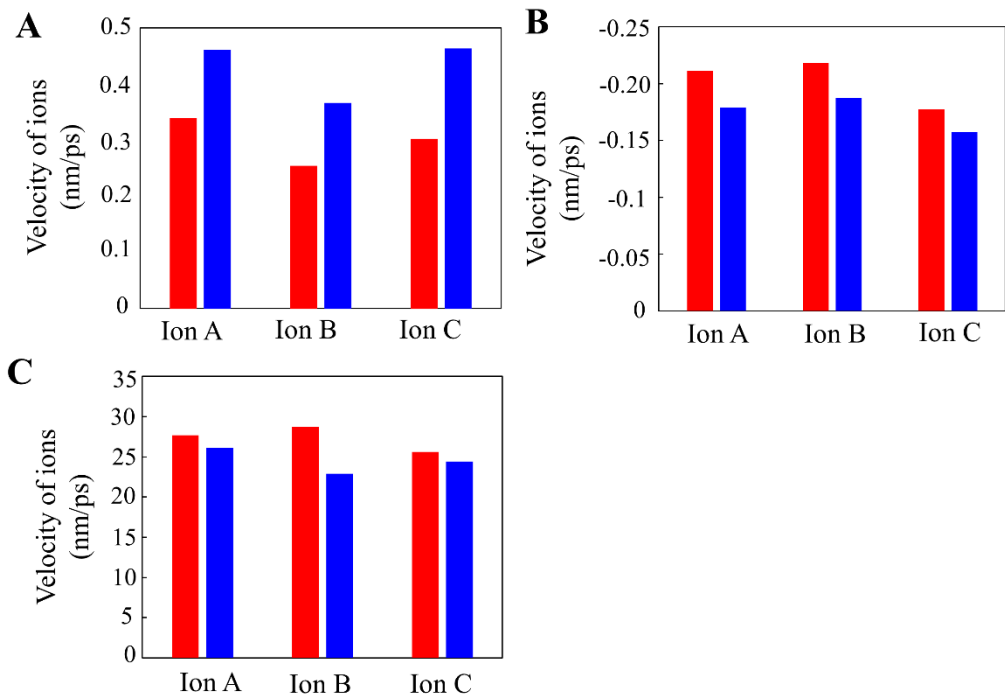


Figure 5.4 Velocity of three cation ions in 10 ns metadynamics simulation. (a) K^+ ions., (b) Na^+ ions., (c) Cs^+ ions. Red and blue bars indicate velocities of cation ions in selectivity filters interacting without and with hyperpolarized cell wall, respectively. The locations of ions A, B, and C are shown in figure 5.2.

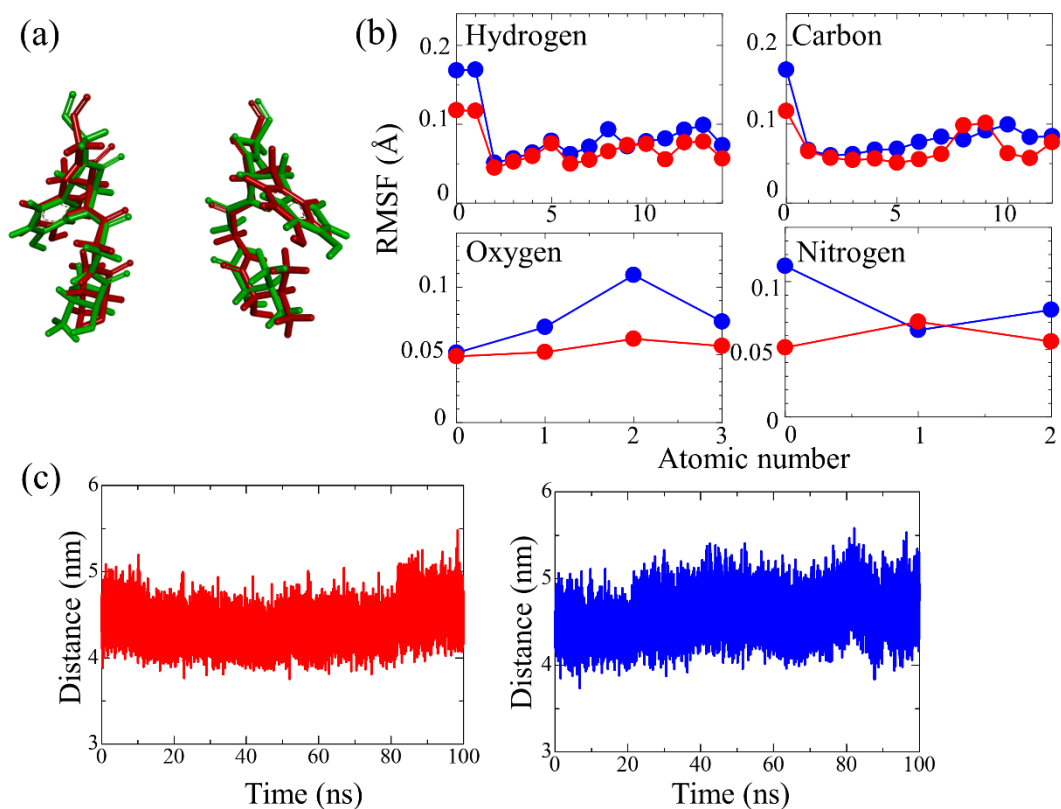


Figure 5.5 Structural change of selectivity filter. (a) Superposition of structure of selectively filters interacting with (green) and without (red) hyperpolarized cell wall after 100 ns calculation. (b) Variations in root mean square fluctuation (RMSF) of H, C, O and N atoms of carboxyl group located at selectivity filter during 100 ns calculation. Blue and red curves indicate RMSFs for selectivity filters interacting without and with hyperpolarized cell wall. (c) Variations in diameter of selectivity filters interacting with (red) and without (blue) hyperpolarized cell wall during 100 ns calculation. The diameter of selectivity filter is defined as the distance between oxygen atoms of facing carboxyl groups.

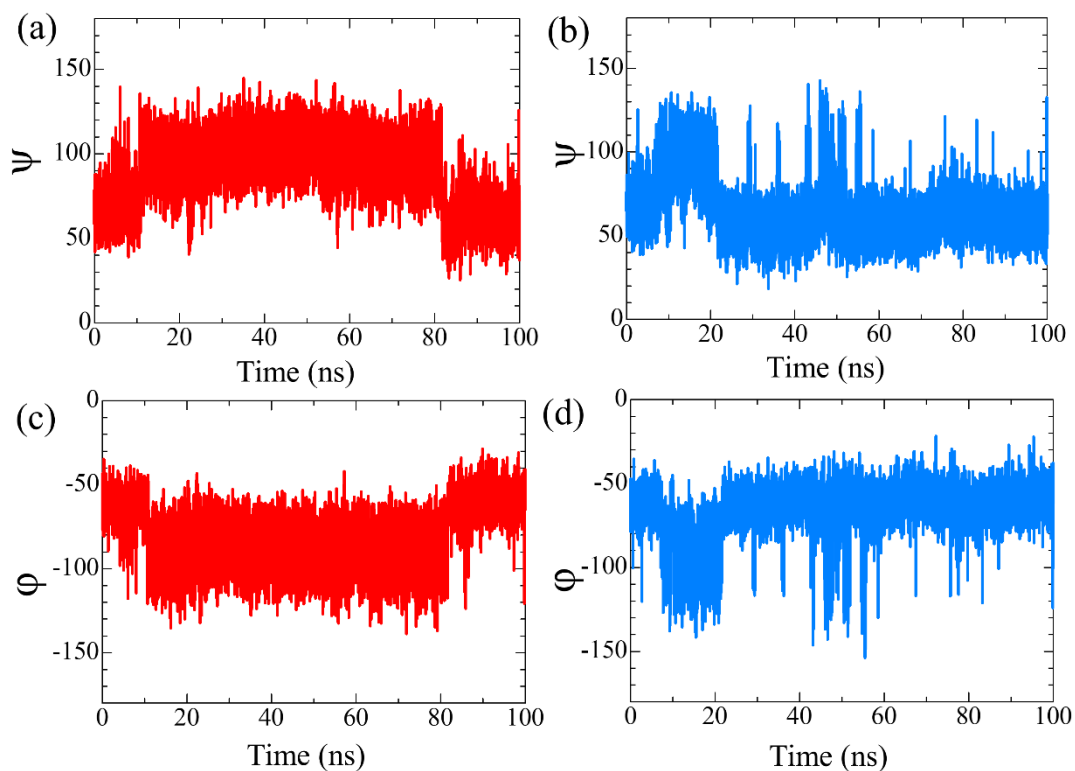


Figure 5.6 Variations of dihedral angles (ψ , ϕ) of the selectivity filter. (a) & (b), ψ of electivity filter interacting without (red) and with (blue) hyperpolarized cell wall. (c) & (d), ϕ of electivity filter interacting without (red) and with (blue) hyperpolarized cell wall. The dihedral angles of ψ and ϕ are shown in figure 5.2.

permeabilities of all three Na^+ ions were reduced by interaction with the hyperpolarized cell wall (Fig. 5.4). As for Cs^+ ion, the permeability of one ion was enhanced by the interaction, but those of others were reduced.

The structure of selectivity filter was a little changed by the hyperpolarized cell wall, although no significant structural change such as disruption and collapse were generated (Fig. 5.5 (a)). The dihedral angles of selectivity filter were affected by interaction with the hyperpolarized cell wall and its large deviations tended to be suppressed (Fig. 5.6). Also, thermal fluctuation in atoms of carboxyl group located at selectivity filter was suppressed by interaction with the hyperpolarized cell wall (Fig. 5.5 (b)). It is accepted that the high ion selectivity of K^+ channel is related to size-matched ion binding sites created by its structure [26], and it is the diameter of selectivity filter that has the most significant impact on the permeability. The average diameter of selectivity filter in 100 ns calculation was 4.39 ± 0.20 and 4.57 ± 0.22 Å for selectivity filters interacting with and without the hyperpolarized cell wall (Fig. 5.5 (c)). Thus, the distance between oxygen atoms of the carboxyl groups was shortened by the interaction.

More charge was accumulated around oxygens atoms of carboxyl groups and K^+ ion by interaction with the hyperpolarized cell wall because the distance between oxygen atoms was shortened (Fig. 5.7). On the other hand, the covalent bonding was not enhanced by the interaction (Fig. 5.8). Thus, the shortened diameter of selectivity filter led to the stronger carboxyl group- K^+ ion interaction due to the accumulated charge. The accumulated charge was generated in the cases of Na^+ and Cs^+ ions as well (the data are not shown). This suggests that the reduced permeabilities of Na^+ and Cs^+ by interaction

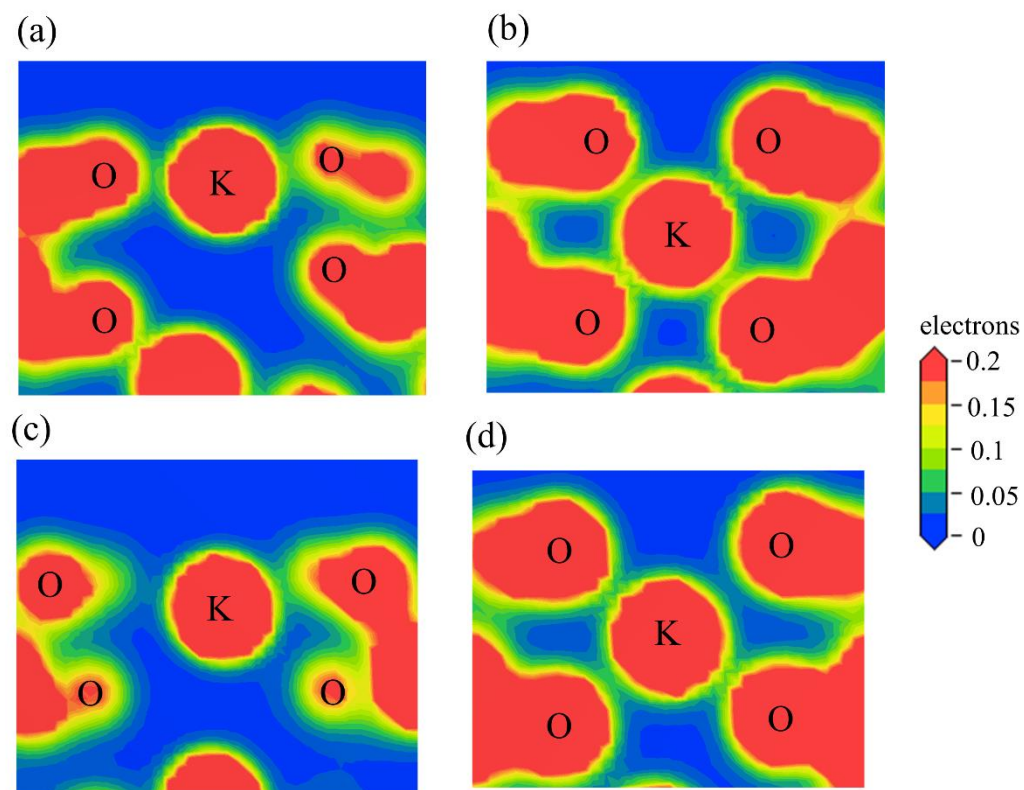


Figure 5.7 Charge maps of selectivity filter. (a) & (b), High and low states of selectivity filter interacting with hyperpolarized cell wall. (c) & (d), High and low states of selectivity filter interacting without hyperpolarized cell wall. O and K indicate oxygen atom and K^+ ion, respectively.

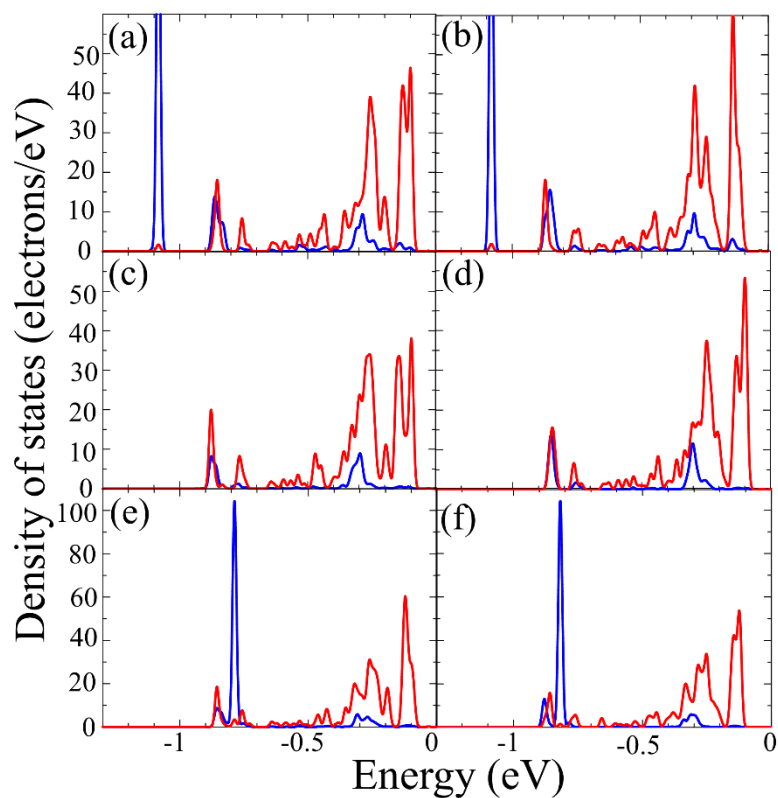


Figure 5.8 Density of states (DOS) of an ion interacting with oxygen atoms of selectivity filter. (a) & (b), K^+ in selectivity filter interacting without and with hyperpolarized cell wall. (c) & (d), Na^+ in selectivity filter interacting without and with hyperpolarized cell wall. (e) & (f), Cs^+ in selectivity filter interacting without and with hyperpolarized cell wall. Blue and red curves indicate s orbitals of ions and p orbitals of oxygen atoms, respectively. Peaks for generation of covalent bonding by interaction with hyperpolarized cell wall are not found in the all cases of K^+ , Na^+ and Cs^+ .

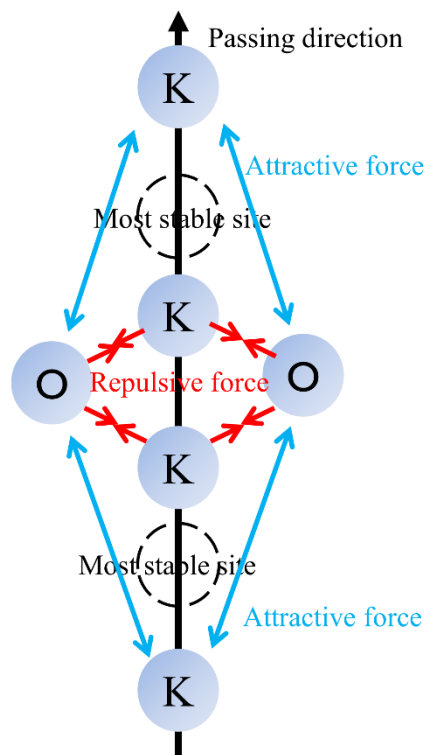


Figure 5.9 Schematic illustration for carboxyl group- K^+ ion interaction. O and K indicate oxygen atom and K^+ ion, respectively. As shown in Fig.5.7, the most stable state of selectivity filter is not in the condition that the K^+ ion is closest to the oxygen atoms, which means that the distance where the carboxyl group-ion interaction is the most stable is farther than the one where the K^+ ion is closest to the oxygen atoms. Hence, the K^+ ion must approach oxygen atoms to a shorter distance than the one where the carboxyl group-ion interaction is the most stable to pass by carboxyl group. Repulsive force is generated when the carboxyl group-ion distance is shorter than the one where the carboxyl group-ion interaction is the most stable. Hence, attractive and repulsive forces work in an ion approaching and leaving the carboxyl group.

with the hyperpolarized cell wall cannot be explained from the viewpoint of carboxyl group-ion interaction. Let consider a simple case where only the carboxyl group-ion interaction is operative. The carboxyl group-ion interaction induces the attractive force at its long distance, while the repulsive force is generated when the carboxyl group-ion distance is shorter than the one where the carboxyl group-ion interaction is the most stable. The attractive (repulsive) interaction enhances (reduces) the permeability in an ion approaching the oxygen atoms, while the attractive (repulsive) force reduces (enhances) the permeability in an ion leaving the oxygen atoms. Thus, the same attractive and repulsive forces due to the carboxyl group-ion interaction work in an ion approaching and leaving the carboxyl group (Fig. 5.9). It is therefore suggested that the variation in permeability by interaction with the hyperpolarized cell wall cannot be explained from the variation in the carboxyl group-ion interaction.

Another important interaction in passing of ions in selectivity filter is the repulsive one between passing ions. Investigations of ion-ion distances showed that one of two K^+ - K^+ distances was shortened by interaction with the hyperpolarized cell wall, while both Na^+ - Na^+ distances were extended by the interaction (Table 5.1). This well correspond to the variations in permeability: the permeability of K^+ was enhanced by interaction with the hyperpolarized cell wall, while the permeability of Na^+ was reduced by the interaction. It is therefore suggested that the “direct knock on” mechanism of repulsive ion-ion interaction plays an essential role in passing of ions in the selectivity filter.

The size match between the selectivity filter and a passing ion has been explained from the viewpoint of energy balance in dehydration of an ion [22]. However, the binding

Table 5.1 The ion-ion distances in ion channel with and without hyperpolarized cell wall after 10ns metadynamics simulations. The upper and under value shows ion-ion distances between ion A and ion B and between ion B and ion C, respectively. The definition of ion A, B and C is shown in figure 5.2.

	With hyperpolarized cell wall (Å)		Without hyperpolarized cell wall (Å)	
K ⁺	A-B	3.90	A-B	4.46
	B-C	5.01	B-C	4.64
Na ⁺	A-B	3.90	A-B	3.79
	B-C	5.30	B-C	4.79
Cs ⁺	A-B	4.20	A-B	4.44
	B-C	5.47	B-C	4.94

Table 5.2 The binding energy of K, Na and Cs ions. The left and right column shows the binding energy in ion channel with and without hyperpolarized cell wall, respectively.

	With hyperpolarized cell wall (Ha)	Without hyperpolarized cell wall (Ha)
K ⁺	-0.186	-0.179
Na ⁺	-0.192	-0.162
Cs ⁺	-0.191	-0.180

energy between the passing ions and the selectivity filter was increased by interaction with the hyperpolarized cell wall, independently of the kind of ions (Table 5.2). Thus, the variation in permeability cannot be explained from the viewpoint of energy balance, suggesting that the repulsive K^+ - K^+ interaction is not so large that it cannot mainly affect the binding energy. Interestingly, the modest interaction decisively affects the permeability of ions in selectivity filter.

It is known that nanomaterials such as fullerene [27,28] and Au nanoparticles [29] physically blocks the selectivity pores of the channel. The tetraethylammonium molecule is also a well-known channel blocker [30-32]. However, the present work suggested that interaction with the hyperpolarized cell wall does not suppress the K^+ permeability, but it enhances the permeability. The enhanced permeability will cause the excessive K^+ concentration outside a bacterium, which leads to dysfunction such as low membrane potential and abnormal electrochemical gradients. The dysfunction will occur when the dehydration occurs easily and the K^+ concentration inside/outside a bacterium depends on the K^+ permeability in selectivity filter. It is known that conformational adjustments of the side helices for gate opening in the channel are directly correlated to the ion configuration in the filter³³ and the interconversion between open-activated and close-inactivated states of ion channel is closely related to ion occupancy in selectivity filter [3,34-36]. Therefore, the enhanced K^+ permeability will cause unusual interconversion between open and close gates of ion channel. Thus, the enhanced K^+ permeability can cause dysfunction of K^+ channel whatever is the rate-controlling process. This corresponds to the experiment fact that NPG caused the dysfunction of cell membrane [12].

It is accepted that thermal fluctuation affects functions of selectivity filter [37]. In the present work, because the difference in standard deviation of filter diameter was small between selectivity filters interacting with and without the hyperpolarized cell wall, effect of thermal fluctuation was not considered. However, the thermal fluctuation in atoms of selectivity filter tended to be suppressed by interaction with the hyperpolarized cell wall. The suppressed thermal fluctuation may affect the permeability, although its details are unknown.

5.4 Conclusions

In this chapter, the MD simulation was performed to investigate the effect of hyperpolarized cell wall on the functions of potassium ion channels. The results showed that the velocity of potassium ion increased while other ions did not change so much. This is caused by potassium ion-ion distances becomes shortened by interacting with hyperpolarized cell wall while this did not occur in other ions. This is one of the first study to elucidate the weak interactions cause function disorders in proteins.

References

- [1] A.K. Chatterjee, R. Chakraborty, and T. Basu, “Mechanism of Antibacterial Activity of Copper Nanoparticles”, *Nanotechnology* **25**, (2014) 135101-135107.
- [2] G. Zhao and S.E. Stevens Jr., “Multiple Parameters for the Comprehensive Evaluation of the Susceptibility of Escherichia coli to the Silver Ion”, *BioMetals* **11**, (1998) 27-32.
- [3] L. G. Cuello, V. Jogini, D. M. Cortes and E. Perozo, “Structural Mechanism of C-type Inactivation in K⁺ Channels”, *Nature* **466**, (2010) 209.
- [4] S. Garavaglia et al., “The Structure of Rigidoporus Lignosus Laccase Containing a Full Complement of Copper Ions, Reveals an Asymmetrical Arrangement for the T3 Copper Pair”, *J. Mol. Biol.* **342**, (2004) 1519-1531.
- [5] B. Hille, “Ionic Channels of Excitable Membranes. 3rd Edition. *Massachusetts: Sinauer Inc*”, **814** (2001).
- [6] D. A. Doyle *et al.*, “The Structure of the Potassium Channel: Molecular Basis of K⁺ Conduction and Selectivity”, *Science* **280**, (1998) 69-77.
- [7] Y. Zhou, J. H. Morais-Cabral, A. Kaufman and R. MacKinnon, “Chemistry of Ion Coordination and Hydration Revealed by a K⁺ Channel-Fab Complex at 2.0Å Resolution”, *Nature* **414**, (2001) 43-48.
- [8] F. I. Valiyaveetil, M. Leonetti, T. W. Muir and R. MacKinnon, “Ion Selectivity in a Semisynthetic K⁺ Channel Locked in the Conductive Conformation. *Science* **314**, (2006) 1004-1007.
- [9] C. Domene *et al.*, “The Role of Conformation in Ion Permeation in a K⁺ Channel”, *Journal of the American Chemical Society* **130**, (2008) 3389-3398.

- [10] H. T. Kratchvil et al., “Probing the Effects of Gating on the Ion Occupancy of the K⁺ Channel Selectivity Filter Using Two-Dimensional Infrared Spectroscopy”, *Journal of the American Chemical Society* **139**, (2017) 8837-8845.
- [11] P. Stevenson et al., “Visualizing KcsA Conformational Changes upon Ion Binding by Infrared Spectroscopy and Atomistic Modeling”, *The Journal of Physical Chemistry B* **119**, (2015) 5824-5831.
- [12] M. Hakamada, S. Taniguchi and M. Mabuchi, “Antibacterial Activity of Nanoporous Gold against Escherichia Coli and Staphylococcus epidermidis”, *J. Mater. Res.* **32**, (2017) 1787-1795.
- [13] N. Miyazawa, M. Hakamada and M. Mabuchi, “Antibacterial Mechanisms Due to Hyperpolarization Induced by Nanoporous Au”, *Scientific Reports* **8**, (2018) 3870.
- [14] A. D. MacKerell Jr. et al., “All-Atom Empirical Potential for Molecular Modeling and Dynamics Studies of Proteins”, *J. Phys. Chem. B* **102**, (1998) 3586-3616.
- [15] D. V. D. Spoel, E. Lindahl, B. Hess, G. Groenhof, A. E. Mark and H. J. C. Berendsen, “GROMACS: Fast, Flexible, and Free”, *J. Comput. Chem.* **26**, (2005) 1701-1718.
- [16] M. J. Abraham, T. Murtola, R. Schulz, S. Pall, J. C. Smith, B. Hess and E. Lindahl, “GROMACS: High Performance Molecular Simulations through Multi-Level Parallelism from Laptops to Supercomputers”, *Software X* **1-2**, (2015) 19-25.
- [17] M. Bonomi et al., “PLUMED: A Portable Plugin for Free-Energy Calculations with Molecular Dynamics”, *Computer Physics Communications* **180**, (2009) 1961.
- [18] B. J. Delley, “An All-Electron Numerical Method for Solving the Local Density Functional for Polyatomic Molecules”, *J. Chem. Phys.* **92**, (1990) 508-517.
- [19] B. J. Delley, “From Molecules to Solids with the Dmol3 Approach”, *J. Chem. Phys.*

113, (2000) 7756-7764.

[20] J. P. Perdew et al., “Atoms, Molecules, Solids, and Surfaces: Application of the Generalized Approximation for Exchange and Correlation”, *Phys. Rev. B* **46**, (1992) 6671-6687.

[21] D. Vanderbilt, “Soft Self-Consistent Pseudopotentials in a Generalized Eigenvalue Formalism”, *Phys. Rev. B* **14**, (1990) 7892-7895.

[22] J. H. Marais-Cabral, Y. Zhou and R. MacKinnon, “Energetic Optimization of Ion Conduction Rate by the K⁺ Selectivity Filter”, *Nature* **414**, (2001) 37-42.

[23] D. A. Doyle et al., “The Structure of the Potassium Channel: Molecular Basis of K⁺ Conduction and Selectivity”, *Science* **280**, (1998) 69-77.

[24] S. Berneche and B. Roux, “Energetics of Ion Conduction through the K⁺ Channel”, *Nature*, **414**, (2001) 73-77.

[25] D. A. Kopfer et al., “Ion Permeation in K⁺ Channels Occurs by Direct Coulomb Knock-On”, *Science* **346**, (2014) 352-355.

[26] S. W. Lockless, M. Zhou and R. Mackinnon, “Structural and Thermodynamic Properties of Selective Ion Binding in a K⁺ Channel”, *PLoS Biology* **5**, (2007) 1079-1088.

[27] M. Calvaresi, S. Furini, C. Domeme, A. Bottoni and F. Zerbetto, “Blocking the Passe: C₆₀ Geometrically Clogs K⁺ Channels”, *ACS Nano* **9**, (2015) 4827-4834.

[28] T. A. Hilder, P. Ridone, Y. Nakayama, B. Martinac and S. -H. Chung, “Binding of Fullerenes and Nanotubes to MscL”, *Scientific Reports* **4**, (2015) 1-10.

[29] A. Leifert et al., “Differential hERG Ion Channel Activity of Ultrasmall Gold Nanoparticles”, *PNAS* **110**, (2013) 8004-8009.

- [30] R. French and J. J. Shoukimas, "Blockage of Squid Axon Potassium Conductance by Internal Tetra-n-Alkylammonium Ions of Various Sizes", *Biophys. J.* **34**, (1981) 271-291.
- [31] G. Yallen, M. E. Jurman, T. Abramson and R. Mackinnon, "Mutations Affecting Internal TEA Blockage Identify the Probable Pore-Forming Region of a K⁺ Channel", *Science* **25**, (1991) 939-942.
- [32] L. Heiginbotham and R. Mackinnon, "The Aromatic Binding Site for Tetraethylammonium Ion on Potassium Channels", *Neuron* **8**, (1992) 483-491.
- [33] O. B. Clarke et al., "Domain Reorientation and Rotation of an Intracellular Assembly Regulate Conduction in Kir Potassium Channels", *Cell* **141**, (2010) 1018-1029.
- [34] J. F. Cordero-Morales, L. G. Cuello, Y. Zhao, V. Jogini, D. M. Cortes, B. Roux and E. Perozo, "Molecular Determination of Gating at the Potassium Channel Selectivity Filter" *Nature structural & molecular biology* **13**, (2006) 311-318.
- [35] T. Lu et al., "Probing Ion Permeation and Gating in a K⁺ Channel with Backbone Mutation in the Selectivity Filter", *Nature Neuroscience* **4**, (2001) 239.
- [36] B. Galeano, E. Korff, and W.L. Nicholson, "Inactivation of Vegetative Cells, but not Spores, of *Bacillus anthracis*, *B. cereus*, and *B. subtilis* on Stainless Steel Surfaces Coated with an Antimicrobial Silver- and Zinc-Containing Zeolite Formulation", *Appl. Environ. Microbiol.* **69**, (2003) 4329-4331.
- [37] M. Thomas, D. Jaystilaka and B. Corry, "An Entropic Mechanism of Generating Selective Ion Binding in Macromolecules", *PLOS Computational Biology* **9**, (2013) e1002914.

CHAPTER6

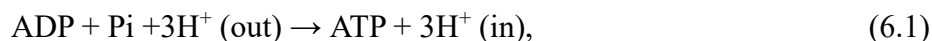
THE EFFECT OF NANOPOROUS AU ON THE FUNCTIONS OF ATP SYNTHASE

6.1 Introduction

Adenosine triphosphate (ATP) is the universal energy resources for all living creatures. As for bacteria, ATP synthase which produces ATP is located at the cell membrane. The structures and functions of ATP synthase is significantly complicated. A high-resolution structure analysis of ATP synthase was recently performed [1]. The F_1F_0 -ATP synthase consist of two domains of F_1 and F_0 [2-5]. The F_1 domain, which is located at the outside of cell membrane, has the catalytic sites to produce ATP. The F_0 domain is embedded in cell membrane and has the proton transfer system, as explained later. The F_1 domain has 5 subunits of $\alpha_3\beta_3\gamma\delta\epsilon$ and the F_0 domain has 2 subunits of a and c. The subunit c consists of cylindrically located transmembrane helixes and the subunit a is located beside the subunit c.

F_1F_0 -ATP synthase is known to produce ATP through its rotational motion [6-8]. The rotational motion of ATP synthase has been well studied [9,10]. In this process, F_0 domain passively transports H^+ ion from outside to inside of cell membrane. The H^+ ionic

electrochemical gradient is essential to produce ATP from ADT through following reaction:



where ADP is adenosine diphosphate and P_i is phosphoric acid, respectively. In the ATP synthesis process of (6.1), Asp61 amino acid located at the middle of subunit c plays an important role [11]. The protons are transferred at the middle of the lipid membrane via water half-channels [12]. The protonation and de-protonation of Asp61 occurs and this causes structural changes of helixes in subunit c, resulting in swiveling of subunit c [13]. Therefore, the protonation and de-protonation of Asp61 is a vital function in ATP production.

As discussed in the previous chapter, nanoporous Au (NPG) showed the high antimicrobial properties due to dysfunction of cell membrane of bacteria [14]. In chapter 5, the effect of hyperpolarized cell wall on the functions of ion channel was shown [15]. ATP synthase is also a vital membrane protein because ATP is energy resource of a life as described above. If the hyperpolarized cell wall affects the functions of ATP synthase, bacteria should easily die. As discussed in chapter 5, the selectivity filter of ion channel has such a sophisticated structure that the weak interactions of NPG can disrupt the functions of ion channel. On the other hand, ATP synthase is rather a large and rigid protein compared with ion channels. The results described in this chapter will show that NPG can disrupt the functions of ATP synthase.

In the present chapter, molecular dynamics (MD) and first-principles (FP) calculations are performed to investigate the effect of hyperpolarized cell wall on the functions of ATP synthase. The MD simulations show that the Asp61 in ATP synthase is more negatively hyperpolarized in interacting with the hyperpolarized cell wall. The negative hyperpolarization attracts proton in ASP 61, which leads to the strengthened O-H bond. The FP calculation discloses the origins of strengthened O-H bond from electronic point of view.

6.2 Methods

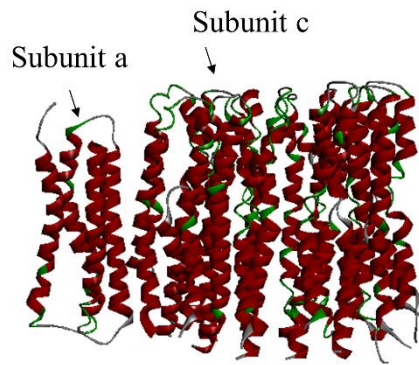
The peptidoglycan model of scaffold model was obtained using molecular dynamics and first-principles simulations. The calculation methods were the same used in the previous chapters¹⁵. A part of hyperpolarized peptidoglycan molecule was taken from the front edge of the peptidoglycan, where the taken part was GlcNAc molecule located furthest from the interaction point. The electrostatic potentials of hyperpolarized and non-hyperpolarized peptidoglycan molecules are shown in Figure 3.6 (d) and (a).

Initial coordinates for potassium channel were taken from the crystal structures 1C17 from the protein data bank. The protonated and non-potonated ATP synthase models were prepared where the all Asp61 amino acids were protonated in protonated model and no Asp61 amino acids were protonated in non-protonated model. The channel was embedded

in a bilayer of 400 POPE lipid and solvated in 30,000 water molecules and 22 K^+ ions to neutralize the system using CHARMM-GUI web site. Periodic boundary conditions were applied. Energy minimizations and MD simulations were performed using the CHARMM force field [16] using gromacs 5.1.1 code [17,18]. The system was energy-minimized using the steepest decent algorithm (500,000steps). MD simulations were performed at 300K with the time step of 1.0 fs. The system was equilibrated for 10 ns to obtain a stable structure of peptidoglycan with the constant number of particles, volume and temperature (NVT) ensemble. Finally, the 100 ns NVT simulations were performed. To investigate the effect of hyperpolarization of the cell wall, a part of the hyperpolarized peptidoglycan molecule was positioned near the outermost amino acids of ATP synthase, which was located outermost of ion channel (Figure 6.1). The energy minimization, equilibration and 100ns NVT simulations described above was conducted on ATP synthase models interacting with hyperpolarized cell wall.

The energy calculations were performed on the Asp61 amino acids by FP calculations using the Dmol3 code [19,20]. The Asp61 model is shown in Figure 6.2. In the DMol3 method, the physical wave functions were expanded in terms of the accurate numerical basis sets. The exchange-correlation energies were treated according to the generalized

(a)



(b)



Figure 6.1 The simulation model of ATP synthase consisting of subunit a and c. The hyperpolarized peptidoglycan is located above ATP synthase.

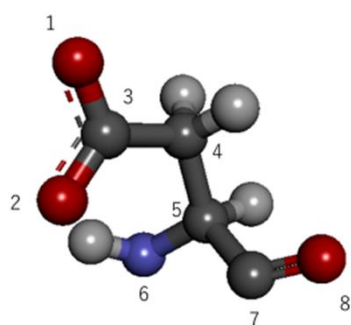


Figure 6.2 The structure of Asp61. The white, gray, red and blue balls represent hydrogen, carbon, oxygen and nitrogen atoms, respectively.

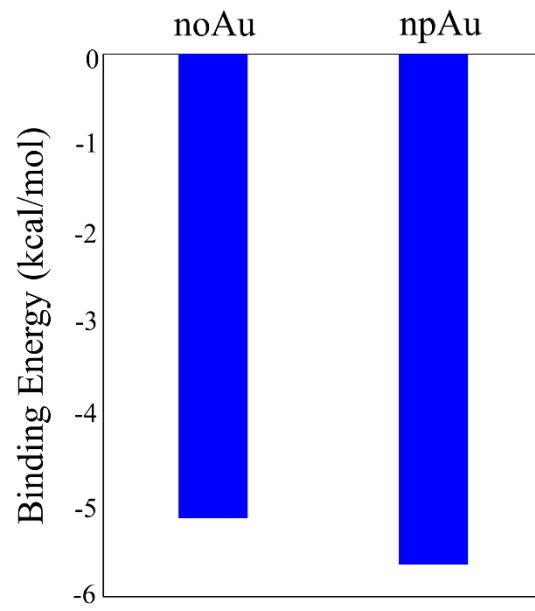


Figure 6.3 The binding energy of proton in Asp61. Noted that the binding energy of Asp61 is lower in ATP synthase interacting with hyperpolarized cell wall.

gradient approximation (GGA) with the Perdew-Wang 1991 (PW91) approximation [21] to deal with the core (DNP). Optical Bloch equation (OBE) calculations were used to set the van der Waals interactions into calculations.

6.3 Results and Discussion

Figure 6.3 shows the binding energy of hydrogen atom with Asp61 amino acid. The binding energy E_b is calculated by:

$$E_b = E_{ATP_protonation} - E_{ATP_non-protonation} - E_H, \quad (6.2)$$

where $E_{ATP_protonation}$ and $E_{ATP_non-protonation}$ are the average internal energies of protonated and non-protonated ATP synthase models during last 10ns in 100ns production simulation, and E_H is the internal energy of hydrogen atoms, respectively. Noted that the binding energy of hydrogen atom with Asp61 is lower in ATP synthase interacting with hyperpolarized cell wall than without hyperpolarized cell wall.

Figure 6.4 shows dihedral angles of Asp 61 in ATP synthase interacting with and without hyperpolarized cell wall. The dihedral angles of Asp61 interacting with hyperpolarized cell wall is overall lower than those without hyperpolarized cell wall. Thus, the hyperpolarized cell wall affected the conformation of Asp 61.

Figure 6.5 shows electrostatic potentials of Asp61 interacting with and without hyperpolarized cell wall. The electrostatic potential of Asp61 interacting with hyperpolarized cell wall is more negative than that without hyperpolarized cell wall.

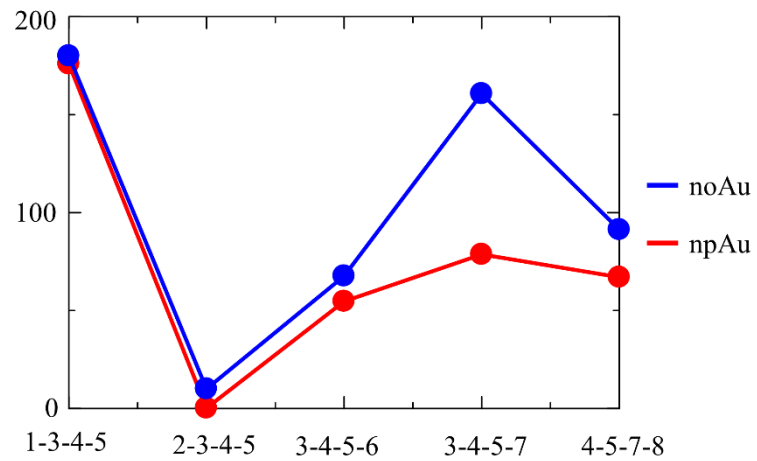


Figure 6.4 The dihedral angles of Asp61 in ATP synthase interacting with and without hyperpolarized cell wall. The number is defined in figure 6.2. The dihedral angles are changed by interactions with hyperpolarized cell wall.

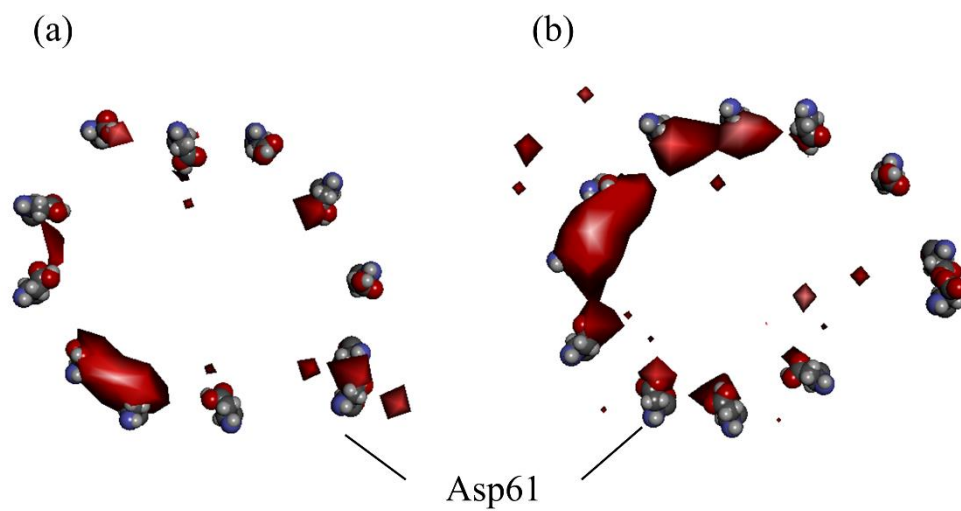


Figure 6.5 The electrostatic potential of Asp61 in ATP synthase interacting with and without hyperpolarized cell wall. The red region shows electrostatic potential. The isovalue is $-40kT$. The negative polarization is enhanced in ATP synthase interacting with hyperpolarized cell wall.

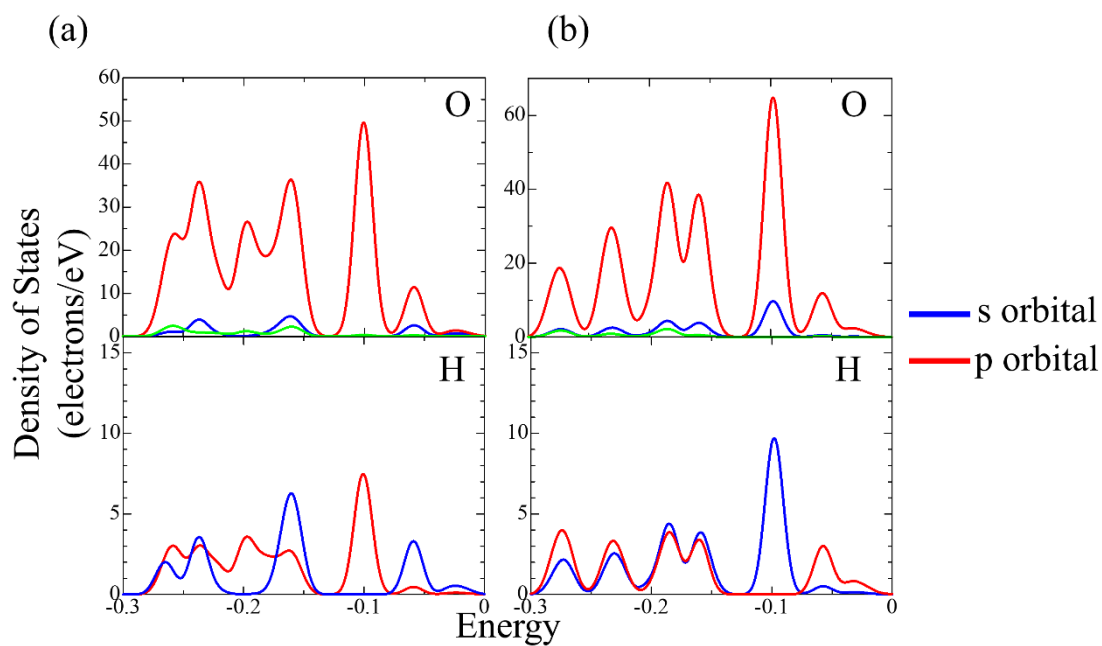


Figure 6.6 The density states of oxygen and hydrogen atoms in protonated Asp61 interacting with and without hyperpolarized cell wall, respectively. The blue and red lines show s- and p- orbital, respectively. The peaks for hybridization are found in Asp61 interacting with hyperpolarized cell wall.

The negative polarization enhanced by interactions with hyperpolarized cell wall more strongly attracts H^+ by the Coulombic force. Therefore, the decreased E_b is suggested to be due to the more-negatively polarized Asp61 caused by the interactions with hyperpolarized cell wall.

The enhanced stability in O-H bond of Asp61 interacting with hyperpolarized cell wall can be explained from electronic viewpoint. The density of states (DOS) of Asp 61 interacting without hyperpolarized cell wall is shown in figure 6.6 (a), where the oxygen and hydrogen atoms are those of carbonyl group of Asp61. Some peaks are found in oxygen and hydrogen atoms, respectively. However, the peaks of DOS are sharp in Asp61 when interacting with hyperpolarized cell wall, compared with that without hyperpolarized cell wall. This suggests that hybridization is stronger in Asp61 when interacting with hyperpolarized cell wall. The hybridization corresponds to the enhanced O-H binding.

The reaction velocity, v , can be predicted by the Arrhenius equation: $v = A \exp(-E/kT)$, where A is a constant, E is the activation energy, k is the Boltzmann constant and T is the absolute temperature. The binding energy E_b is not the activation energy, but it is comparable to the activation energy. Hence, the ratio of reaction velocity of Asp61 interacting with and without hyperpolarized cell wall is 0.61. The protonation/deprotonation process produces the rotation of subunit c [13,22]. Because the rotation velocity of ATP synthase is 167 s^{-1} , the rotation velocity is suggested to be reduced to 102 s^{-1} by the interactions with hyperpolarized cell wall. Therefore, only a little difference in binding energy results in a large difference in production of ATP.

As mentioned in chapter 1, the microarray analyses showed that NPG disturbed the functions of the cell membrane of bacteria. The present study suggested that the proton transportation will be disturbed in ATP synthase in interacting with NPG. ATP is a vital molecule to keep life of bacteria because ATP is the energy resources of a life. Therefore, the disfunction of ATP synthase is one of the antimicrobial mechanisms for NPG.

6.4 Conclusions

The MD simulations and FP calculation were performed to investigate the effect of hyperpolarized cell wall on the functions of ATP synthase. The results showed that the binding energy of O-H bonds in carbonyl groups were increased in interacting with hyperpolarized cell wall compared that without hyperpolarized cell wall. The structural change of Asp61 was observed and negative polarization of Asp61 was enhanced in interacting with hyperpolarized cell wall. The DOS analyses showed that O-H bond is strengthened in interacting with hyperpolarized cell wall. Therefore, it is suggested that the structural change of Asp61 increases its negative polarization and the enhanced polarization attracts proton in Asp61, which results in disturbance of proton transport in ATP synthase. Thus, this chapter proposed one of the antimicrobial mechanisms for NPG.

References

- [1] A. P. Srivastava et al., “High-Resolution Cryo-EM Analysis of the Yeast ATP Synthase in a Lipid Membrane”, *Science* **360**, (2018) 619 1-8.
- [2] P. D. Boyer, *Annu. Rev. Biochem.*, “The ATP Synthase—A Splendid Molecular Machine” *Annu. Rev. Microbiol.* **66**, (1997) 717–749.
- [3] G. Deckers-Hebestreit and K. Altendorf, “The F₀F₁-type ATP synthesis of bacteria: structure and function of the F₀ complex”, *Annu. Rev. Microbiol.* **50**, (1996) 791–824.
- [4] R. H. Fillingame, “Coupling H⁺ Transport and ATP Synthesis in F₁F₀-ATP Synthases: Glimpses of Interacting Parts in a Dynamic Molecular Machine” *J. Exp. Biol.* **200**, (1997) 217–224.
- [5] R. H. Fillingame, “The Bacteria”, Academic, New York, 12 (1990) 345–391.
- [6] T. M. Duncan, V. V. Bulygin, Y. Zhou, M. L. Hutcheon and R. L. Cross, *Proc. Natl., “Rotation of Subunits during Catalysis by Escherichia coli F₁-ATPase”*, *Acad. Sci. USA* **92**, (1995) 10964–10968.
- [7] D. Sabert, S. Engelbrecht and W. Junge, “Intersubunit Rotation in Active F-ATPase”, *Nature* **381**, (1996) 623–625.
- [8] H. Noji, R. Yasuda, M. Yoshida & K. Kinosita Jr. “Direct Observation of the Rotation of F₁-ATPase”, *Nature* **386**, (1997) 249–302.
- [9] J. L. Martin et al., “Elastic Coupling Power Stroke Mechanism of the F₁-ATPase Molecular Motor”, *PNAS* **115**, (2018) 5750–5755.
- [10] J. Czub and H. Grubmüller, “Torsional Elasticity and Energetics of F₁-ATPase”, *PNAS* **108** (2011) 7408–7413.
- [11] W. Jiang and F. H. Robert, “Interacting helical faces of subunits a and c in the F₁F₀

ATP synthase of *Escherichia coli* defined by disulfide cross-linking”, *Proc. Natl. Acad. Sci. USA* **95**, (1998) 6607–6612.

[12] H. Gohlke, D. Schlieper and G. Groth, “Resolving the Negative Potential Side (n-side) Water-accessible Proton Pathway of F-type ATP Synthase by Molecular Dynamics Simulations”, *The Journal of Biological Chemistry* **287**, (2012) 36536–36543.

[13] R. H. Fillingame, P. Ryan Steed, “Half Channels Mediating H⁺ Transport and the Mechanism of Gating in the F_o Sector of *Escherichia coli* F₁F_o ATP Synthase”, *Biochimica et Biophysica Acta* **1837**, (2014) 1063–1068.

[14] M. Hakamada, S. Taniguchi and M. Mabuchi, “Antibacterial Activity of Nanoporous Gold Against *Escherichia coli* and *Staphylococcus epidermidis*”, *J. Mater. Res.* **32**, (2017) 1787-1795.

[15] N. Miyazawa, M. Hakamada and M. Mabuchi, “Antibacterial Mechanisms due to Hyperpolarization Induced by Nanoporous Au”, *Scientific Reports* **8**, (2018) 3870 1-8.

[16] A. D. MacKerell Jr. et al., “All-Atom Empirical Potential for Molecular Modeling and Dynamics Studies of Proteins”, *J. Phys. Chem. B* **102**, (1998) 3586-3616.

[17] D. V. D. Spoel, E. Lindahl, B. Hess, G. Groenhof, A. E. Mark and H. J. C. Berendsen, “GROMACS: Fast, Flexible, and Free”, *J. Comput. Chem.* **26**, (2005) 1701-1718.

[18] M. J. Abraham et al., “GROMACS: High Performance Molecular Simulations through Multi-Level Parallelism from Laptops to Supercomputers”, *Software X* **1-2**, (2015) 19-25.

[19] B. J. Delley, “An All-Electron Numerical Method for Solving the Local Density Functional for Polyatomic Molecules”, *J. Chem. Phys.* **92**, (1990) 508-517.

[20] B. J. Delley, “From Molecules to Solids with the Dmol3 Approach”, *J. Chem. Phys.*

113, (2000) 7756-7764.

[21] J. P. Perdew et al., “Atoms, Molecules, Solids, and Surfaces: Application of the Generalized Approximation for Exchange and Correlation”, Phys. Rev. B **46**, (1992) 6671-6687.

[22] S. Mukherjee and A. Warshel, “Realistic simulations of the coupling between the protomotive force and the mechanical rotation of the F_0 -ATPase”, PNAS 109, (2012) 14876-14881.

CHAPTER7

GENERAL CONCLUSIONS

The nanoporous metals show remarkable activities such as its catalytic behavior. The catalytic properties of nanoporous Au (NPG) on organic matters has been reported before. This high catalytic activity should be caused by the large lattice strains on its surfaces. However, the interactions between nanoporous Au and organic matters are usually caused by weak interactions such as Coulombic or van der Waals interactions. These weak interactions usually do not cause heavy effects on organic matters. Therefore, to investigate the origins of interactions between NPG and organic matters should be elucidated. Under this purpose, this thesis treats the enhanced catalytic activity of laccase by NPG and antimicrobial activity (AA) of NPG.

In chapter 2, the origins of enhanced catalytic activity of laccase immobilized on self-assembled monolayer (SAM) modified Au was studied using molecular dynamics simulations. The results showed that the conformation of laccase was changed by binding with SAM. This leads to strong hydrophobic interactions between ligand and enzyme. The interactions between SAM and laccase is via covalent bonds. Therefore, this chapter investigated the effect of strong interactions on protein. The strong interaction easily causes conformation changes of a protein as shown in this chapter.

In chapter 3, the antimicrobial properties of NPG was investigated. The hyperpolarization and mechanical characteristics of cell wall of bacteria was studied

using fluorescent microscopy observation, scanning probe microscopy, atomistic and electronic simulations. Bacteria such as *E.coli* is protected by cell wall so nanostructured substrates which has millimeter scale should firstly affect cell wall. The fluorescent microscopy observation and combination of molecular dynamics (MD) and first-principles (FP) calculations showed that cell wall of bacteria was negatively hyperpolarized by interacting with nanoporous Au. The MD simulations also showed that ion channel was denaturated by hyperpolarized cell wall.

In chapter4, the electronic origins of hyperpolarization of cell wall caused by NPG was studied. The results of AA of nanoporous metals and ultraviolet photoelectron spectrometry (UPS) measurements showed that the AA corresponded with the work function (WF). The work functions were known to be increased by lattice strains on the metallic surfaces. This is related with the spilling out of electrons on the surface of metals. The FP simulation showed that the high WF was caused by enhanced spilling out of electrons of nanoporous metals.

In chapter5, the effect of hyperpolarized cell wall on the functions of ion channel was studied using MD simulations. The hyperpolarization of cell wall itself cannot kill bacteria and the affection on cell membrane should be studied. The interactions between hyperpolarized cell wall and membrane protein is weak interactions. Therefore, the overall structure of ion channel was not so changed. On the other hand, the ionic velocity passing through ion channel was enhanced for potassium ion and not so changed for sodium and cesium ions. This is caused by the change of ion-ion distances. The structures of selectivity filter in ion channel was so sophisticated and the delicate structural change caused by weak interactions can disrupt the function of proteins.

In chapter6, the effect of hyperpolarized cell wall on ATP synthase was investigated. ATP synthase is a vital membrane protein because ATP is energy resource of a life. The results of MD simulation showed that the binding energy of protons and Asp61 was decreased by interacting with hyperpolarized cell wall. This will result in proton transport will be difficult and ATP production was much less than that without hyperpolarized cell wall. This is caused by the structural change of ATP synthase and polarization of Asp61.

ACKNOWLEDGEMENTS

I would like to express my sincere gratitude Professor Mamoru Mabuchi of Graduate School of Energy Science, Kyoto University, who is my superior on this doctoral thesis, for his stimulating discussions, and beneficial and knowledgeable guidance throughout this study.

I am deeply grateful to Professor Hirohiko Takuda and Professor Toshiya Doi of Graduate School of Energy Science, Kyoto University, for their helpful suggestions and comments.

I am sincerely thankful to Associate Professor Masataka Hakamada of Graduate School of Energy Science, Kyoto University, for his experimental help and fruitful discussions.

I am grateful to Associate Professor Hiromu Kusuda, Assistant Professor Youqing Chen and Assistant Professor Eishi Kusaka of Graduate School of Energy Science, Kyoto University, for their kindly advises.

I acknowledge former Professor Hajime Iwasaki of University of Hyogo, Dr. Akio Nishiyama of former research director in Mitsubishi Materials Corporation, former Professor Tatsuhiko Aizawa of Shibaura Institute of Technology, Dr. Kohmei Halada of National Institute for Materials Science, Professor Hiromi Nakano of Toyohashi University of Technology and Dr. Yasumasa Chino of National Institute of Advanced Industrial Science and Technology, for their beneficial suggestions.

Part of my study was financially supported by a Grant-in-Aid for research Fellow of the Japan Society for the Promotion of Science (Grant No. 16J11132), which I acknowledge.

I sincerely appreciate kindly and continuous encouragement and helpful discussion of all members of Division of Resources and Energy System, and Division of Mineral Processing, Department of Energy Science and Technology, Graduate School of Energy Science, Kyoto University. Finally, I thank my family and friends for their invaluable assistance.

LIST OF PUBLICATIONS

The publications related to this thesis are listed in the following

Chapter 2

[1] N. Miyazawa, M. Tanaka, M. Hakamada, M. Mabuchi, “Molecular Dynamics Study of Laccase Immobilized on Self-Assembled Monolayer-Modified Au”, *Journal of Materials Science* **52** (2017), 12848-12853.

Chapter 3

[2] N. Miyazawa, M. Hakamada, M. Mabuchi, “Antimicrobial mechanisms due to hyperpolarization induced by nanoporous Au”, *Scientific Reports* **8** (2018), 3870 1-8.

Chapter 4

[3] N. Miyazawa, S. Sakakibara, M. Hakamada, M. Mabuchi, “Electronic origin of antimicrobial activity owing to surface effect”, *Scientific Reports*, in press.

Chapter 5

[4] N. Miyazawa, M. Hakamada, M. Mabuchi, “Weak interaction causes dysfunction of a potassium ion channel”, to be published.

Chapter 6

[5] N. Miyazawa, M. Hakamada, M. Mabuchi, “Weak interaction causes dysfunction of a potassium ion channel”, to be published.

Other publications

- [1] N. Miyazawa, M. Hakamada and M. Mabuchi, “Energy Jump During Bond Breaking”, *Physical Review B* **96** (2017), 014115 1-7.
- [2] N. Miyazawa, S. Suzuki, M. Mabuchi and Y. Chino, “Atomistic Simulations of the Effect of Y and Al Segregation on the Boundary Characteristics of a Double Twin in Mg”, *Journal of Applied Physics* **122** (2017), 165103 1-13.
- [3] N. Miyazawa, T. Yamaoka, M. Hakamada and M. Mabuchi, “Atomistic Study of Inelastic Deformation in Aluminum Grain Boundary Fractures”, *Philosophical Magazine Letters* **97** (2017), 476-485.
- [4] N. Miyazawa, J. Ishimoto, M. Hakamada and M. Mabuchi, “Mechanical Characterization of Nanoporous Au with Self-Assembled Monolayers”, *Applied Physics Letters* **109** (2016), 261905 1-4.